Direct and Indirect Measurement of Photonuclear Reactions Relevant to Medical and Reactor Physics

Thesis submitted to
University of Calicut in partial fulfilment
for the Degree of

DOCTOR OF PHILOSOPHY
IN
PHYSICS

By
SHAIMA AKBAR

under the guidance of

Dr. M. M. Musthafa
Senior Professor

DEPARTMENT OF PHYSICS
UNIVERSITY OF CALICUT
February 2025

DECLARATION

I hereby declare that the work presented in the thesis entitled **"DIRECT AND INDIRECT MEASUREMENT OF PHOTONUCLEAR REACTIONS RELEVANT TO MEDICAL AND REACTOR PHYSICS"** is based on the original work done by me under the guidance of Prof.(Dr.) M. M. Musthafa, Senior Professor, Department of Physics, University of Calicut, and has not been included in any other thesis submitted previously for the award of any degree. The contents of the thesis are undergone plagiarism check using 'iThenticate' software at C.H.M.K. Library, University of Calicut, and the similarity index found within the permissible limit. I also declare that the thesis is free from AI generated contents.

Shaima Akbar

Prof. (Dr.) M. M. Musthafa
Research Supervisor
Department of Physics
Calicut University
Kerala-673638

Calicut University
22 February 2025

Dedicated to my family,

and especially to my little girl,

who fills my life with love and joy.

Acknowledgements

I would like to take this opportunity to express my heartfelt gratitude to all those who supported me in fulfilling my dream.

I express my sincere and whole hearted thanks to my esteemed research supervisor Dr. M. M. Musthafa, Senior Professor, Department of Physics, University of Calicut, Kerala, for giving me an opportunity to work under his guidance. His understanding, guidance, encouragement, patience, and personal involvement have been invaluable in helping me overcome the uncertainties that arose during this period. I am deeply indebted to his unwavering perseverance, which enabled me to present this work in the proper perspective.

I express my sincere gratitude to Prof. Mohammed Shahin Thayyil, Head of the Department of Physics and Prof. C. D Ravikumar, Prof. A. M. Vinodkumar, Prof. P. P. Pradyumnan and Prof. Antony Joseph, former Heads of the Department of Physics, University of Calicut for providing me all the support and essential facilities to carry out the research. I also thank all the faculty members including Dr. Libu K. Alexander, Dr. Drisya K., Dr. Zuhail K. P and Dr. Santhosh K. P for their valuable support. I also extent my sincere thanks to library and office staff of the Department of Physics for the help they rendered during the entire course of my research study.

I also express my heartfelt gratitude to Prof. S. V. Suryanarayana, Scientist, NPD, BARC, for his constant motivation and encouragement, which pushed me to strive for significance and uniqueness in my work. I am deepily grateful to K. C. Jagadeesan, my principal collaborator of the DAE-BRNS project, for his invaluable support throughout this journey. I would like to express my special thanks to the DAE-BRNS, for the financial support through Project Fellowship. I would like to express my thanks to Dr. S. Santra,

Dr. P.C. Rout, Dr. Asim Pal, and Dr. Ramandeep Gandhi, Scientist, NDP, BARC, and Dr. Jyoti Pandey for the fruitful discussions.

I am really thankful to my research colleague C. V Midhun, for his encouragement and the fruitful discussions. I really enjoyed the academic and non-academic discussion with K. Hajara, Gokul Das H, Fathima Shirin Shana, Bhagyasree, Salma Ibrahim, Mohammed Shan P T, Sanila, Arjun, Ummukulsu E, Anju K, Vishnu, Rijin N T, Baheeja, Aruna, Riyas, Vafiya Thaslim and Jinu. I lovingly remember the occasion spent with all my friends and juniors, Akhil Ramesh, Nived, Anjali V.K, Aneena Mohan, Vishnu Sathyan, Nihal, Dinto Sebastian and Saroop. Thank you for being my pillars of strength and for always being there with a listening ear and open heart. A special thanks to my friend, Parvathy T, whose unwavering support, both mentally and emotionally, has been a constant source of strength for me. Your understanding, encouragement, and presence have meant more than words can express, and I am forever grateful for everything you've done for me. To Swapna Balakrishnan, you are truly special to me. Your constant care, kindness, and quiet strength have brought immense comfort during some of the most difficult moments. Thank you for always being there, for believing in me, and for being such a beautiful part of this journey.

I can't find the right words to express how truly grateful I am to my beloved mother, Shailaja, who filled my heart with a love for learning from the very beginning. Your guidance, encouragement, and endless love have shaped who I am today. Thank you for everything, Mom. From the depths of my heart, my deepest gratitude goes to Sanjaydath, my soulmate. We embarked on this journey together, and through every twist and turn, your unwavering support, love, and patience have been my greatest strength. You waited through my long hours, stood by me in silence during the toughest moments, and celebrated every small victory with unmatched joy. Your belief in me never wavered, even when I doubted myself. Thank you for being my rock, my refuge, and my constant. This accomplishment is not mine alone, it is ours. I would like to dedicate this work to my precious baby, Nainika, who was born during my PhD journey. Your presence has been a constant source of love, joy, and inspiration. Despite the challenges, you have filled my life with a new sense of purpose and strength. This achievement is as much yours as it is mine. Thank you for your unwavering support in the form of your laughter, your innocence, and your endless love. You have made this journey unforgettable, and I will forever cherish this time with you. I extend my thanks to my elder sister, Shelja, for imparting life wisdom and to my younger sister, Sheeba, for the joyful childhood memories. From the bottom of my heart, I am forever grateful to have such strong, loving, and irreplaceable sisters by my side. Throughout my research journey, I was blessed with the unwavering support of someone who's more than a sister-in-law, Shilliya, my true sister in every sense. Special thanks to my in-laws, Baiju, Subhashini, Sivasankaran and Avinash for their support. I am truly grateful to my father, Akbar K. V, for his constant support and quiet strength throughout my journey.

My heartfelt thanks go to my brotherly companions, Adhil, Avinash, Shefeer, Rithul, Sanal, Arif and Ashik, for being there for me through thick and thin. Thank you all for your support, love, and presence in my life, which have been my strength and joy through every situation, and I'm deeply grateful for each of you always having my back.

As a final word, I would like to thank each and every individual who have been a source of support and encouragement and helped me to achieve my goal and complete my Thesis work successfully.

Shaima Akbar

Contents

List of Tables

List of Figures

Preface

Henri Becquerel's 1896 discovery of radioactivity laid the foundation for the field of nuclear physics. His accidental finding led to further research by Marie Curie, Rutherford, and others, leading to the discovery of nucleus. Nuclear reactions, involving a projectile and a target, help scientists to study nuclear interactions, structure, spin, and nature of forces between nucleons. These reactions release ejectiles like neutrons, charged particles, and radiation, while the residual nucleus often remains excited. Studying nuclear reactions provides key insights into nuclear behavior. In 1936, Niels Bohr introduced the compound nucleus model to explain nuclear reactions. It suggests that when a projectile and target nuclei combine, they form an intermediate state (the compound nucleus), which decays to a final state. This process occurs over a longer time scale ($\approx 10^{-16}$). Bohr's hypothesis, later experimentally confirmed by S.N. Goshal in 1950, showing that the decay of the compound nucleus doesn't depend on how it was formed. However, the theory doesn't explain certain reactions at specific energies, where direct reactions occur faster and involve interactions at the surface level, unlike the compound nuclear process, which involves many internal collisions.

Photonuclear reactions are a type of nuclear reactions that involve photons as projectiles interacting with atomic nuclei, causing the emission of particles such as photons, protons, neutrons, or other charged particles. These reactions can be elastic or inelastic, depending on the energy of the photon. Photonuclear reactions are studied using photon sources like bremsstrahlung, with experimental data obtained through activation analysis, which is essential for accurate measurements and applications. Other facilities such as bremsstrahlung tagged photons, quasi-monoenergetic photons, laser Compton scattered photons are widely used as photon sources. Photonuclear data are used in various fields, including nuclear medicine, radiation therapy, nuclear waste disposal, and nuclear astrophysics. They also helps transmute long-lived radioactive waste into stable or short-lived isotopes. However, the absence of high-quality data in photonuclear reactions represents a substantial obstacle in advancing these domains. While photonuclear reactions have been investigated across numerous elements and isotopes, much of the existing data often lacks proper validation. The lack of accurate photonuclear data severely limits the development of theoretical models. To overcome this, it is important to generate reliable experimental data with proper theoretical validation.

In the nuclear medicine, photon-induced nuclear reactions are crucial as it can effectively be used for producing medical isotopes used in diagnostics and therapy. Studying the interaction of photons with biological samples are also important, as this can provide the indepth effect of these radiations with the healthy cells. Curretly a large number of isotopes, which are produced either using reactor or cyclotron facility are used for medical diagnostic and therapeutic procedures. Short-lived isotopes like ^{18}F and ^{99}Tc are used for diagnostics, while long-lived isotopes like ^{177}Lu and ^{225}Ac are used for therapy. The cost in terms of production, management, storage, and transportation can significantly be reduced if these isotopes are produced locally as per the demand.

^{99m}Tc, with 6-hours half-life, is widely used in medical imaging due to its emission of 140 keV gamma radiation. It minimizes patient radiation exposure, as it does not emit harmful beta or alpha radiation. ^{99m}Tc is produced from its parent isotope, ^{99}Mo, which has a half-life of 66-hours. ^{99}Mo is typically produced through the fission of Highly Enriched Uranium (HEU) in nuclear reactors. This process yields ^{99}Mo, which is used in Mo-Tc generators to produce ^{99m}Tc. However, the fission process also generates large number of unwanted radioactive by-products, which further require transmutation into stable or short lived products. While ^{99m}Tc is produced in hospitals using generators, issues such as rapid decay and losses during transportation, storage, and processing limit its availability for medical use. The metastable ^{99m}Tc will further decays to its ground state after emitting 140 keV, which will be eventually discarded as radioactive waste due to its longer half-life. This thesis explores the re-utilization of ^{99}Tc through photon-induced processes as a potential solution to eliminate the accumulation of ^{99}Tc as nuclear waste, at the same time reducing the demand of production of fresh isotpe significantly.

^{18}F is a key isotope used in positron emission tomography (PET) scanning because it emits 97% positrons with a maximum energy of 635 keV and has a short half-life of 109 minutes. This allows for obtaining high-resolution PET images and quick reduction of radiation exposure for the patients. ^{18}F decays to stable ^{18}O, preventing unwanted radiation. ^{18}F is currently produced by irradiating enriched water ($H_2^{18}O$) with protons in a cyclotron at 18 MeV. This process produces a fluoride ion solution, but using the enriched ^{18}O target, which has only 0.2% natural abundance, makes it expensive. The ^{18}F is then trapped in a quaternary ammonium column and eluted with an aqueous base. However, there is a risk of contaminating the radioisotope with toxic hydrogen fluoride, which could harm the patients. Additionally, the proton beam and energetic neutrons produced during the process can create unwanted radioisotopes. Hence, we have investigated the possibility of producing ^{18}F through a photon-induced reaction and performed theoretical validation.

Photonuclear reactions plays a significant role in fission-fusion reactor technology. High-energy gamma radiation is produced inside reactors due to inelastic collisions between neutrons and atomic nuclei. Low-energy neutrons lead to capture reactions, while high-energy neutrons cause nuclear breakup, resulting in the de-excitation of the nucleus and the generation of energetic photons. These photons can interact with the reactor's structural materials, causing damage. Structural materials like stainless steel, made primarily of chromium, iron, and nickel, can undergo neutron-induced reactions, producing long-lived unwanted isotopes. The energetic photons generated during reactor operation can further induce reactions in these isotopes, leading to additional damage to the materials. ^{58}Co(γ,xp) is a key reaction in the production of hydrogen isotopes. Major pathways for the production of ^{58}Co include ^{58}Ni(n,p), ^{59}Co(n,2n), and ^{60}Ni(n,t). ^{58}Co then undergoes photon-induced reactions from gamma rays produced in the reactor. However, due to the instability of ^{58}Co, directly measuring this reaction is challenging. In this study, the cross-section for ^{58}Co(γ,xp) reaction was determined using the surrogate ratio method, and the optimization of the nuclear reaction code was performed.

With these objectives, the integral cross sections for ^{99}Tc(γ, γ')^{99m}Tc and ^{19}F(γ,n)^{18}F reactions, for different bremsstrahlung endpoint energies, were measured employing the activation technique. The experimental data for the monitor reactions were obtained from the EXFOR nuclear data library. Also the indirect cross section of ^{58}Co(γ,xp) reaction was determined using the surrogate ratio method, employing ^{56}Fe(^{6}Li,α) reaction as the surrogate reaction. Theoretical model calculations were performed using the statistical nuclear reaction code TALYS 1.96, and the theoretical parameters were optimized based on the presently obtained data. In summary, we found that the re-utilization of ^{99}Tc through the photon-induced reaction channel ^{99}Tc(γ, γ')^{99m}Tc is an effective way to reduce the accumulation of ^{99}Tc as nuclear waste. For ^{18}F, we identified photon-induced reactions utilizing bremsstrahlung photons from an electron accelerator as a alternative method for its production. We have determined the cross section corresponding to ^{58}Co(γ,xp), which is useful during the design of reactor structural materials. The surrogate ratio method is applied for the first time to determine photonuclear reactions. Our study also finds that, for unstable medium-mass nuclei, the surrogate ratio method allows the investigation of proton decay probabilities by populating the required compound nucleus, which can then be used to determine the corresponding cross sections.

The overall content of the thesis are summarized as follows.

- Chapter 1 : Provides a foundational introduction to the thesis problem by discussing the literature review and the study's relevance.

- Chapter 2: Provides a detailed theoretical description of photonuclear reactions and surrogate reactions.

- Chapter 3 : Provides a detailed description of the experimental setup, materials, and methods used in the measurements.

- Chapter 4 : Provides a detailed measurement and analysis of the ^{99}Tc(γ,γ')^{99m}Tc reaction, along with a comprehensive theoretical analysis.

- Chapter 5 : Provide a detailed measurement and analysis of the ^{19}F(γ,n)^{18}F reaction, accompanied by an in-depth theoretical analysis.
- Chapter 6 : Provide a detailed measurement and analysis of the ^{58}Co(γ,xp) reaction, along with a comprehensive theoretical analysis.
- Chapter 7 : Summarizes the thesis findings and discusses the future prospects of this work.

List of Acronyms

QMA	Quasi-monochromatic annihilation
GR	Giant Resonance
GDR	Giant Dipole Resonance
QD	Quasi-Deuteron
LCS	Laser Compton Scattered
FEL	Free-Electron Laser
NRF	Nuclear Resonance Fluoroscence
PET	Positron Emission Tomography
SRM	Surrogate Ratio Method
CN	Compound Nucleus
WE	Weisskopf-Ewing
NLD	Nuclear level density
FGM	Fermi Gas Model
CTM	Constant Temperature Model
BFM	Back-shifted Fermi Gas Model
GSM	Generalized Superfluid Model
HF-BCS	Hartree-Fock-Bardeen-Cooper-Schrieffer
HFB	Hartree-Fock-Bogoliubov
PSF	Photon Strength Function
LINAC	Linear Accelerator

List of Publications

1. **Shaima Akbar**, M.M. Musthafa, C.V. Midhun *et al., Determination of photonuclear cross section of* $^{58}Co(\gamma,xp)$ *reaction in the energy region 27-32 MeV via the surrogate ratio method.* European Physical Journal A 61, 13 (2025). https://doi.org/10.1140/epja/s10050-025-01485-w

2. **Shaima Akbar**, M.M. Musthafa, C.V. Midhun *et al., Integral cross section measurement of the* $^{19}F(\gamma,n)^{18}F$ *reaction for 12-20 MeV bremsstrahlung photons.* Applied Radiation and Isotopes. 218 (2025)111673, https://doi.org/10.1016/j.apradiso.2025.111673.

3. **Shaima Akbar**, M.M. Musthafa, C.V. Midhun *et al., Re-utilization of long lived* ^{99}Tc *radio isotope via Photon induced nuclear reactions.* Applied Radiation and Isotopes 204 (2024)111138, https://doi.org/10.1016/j.apradiso.2023.111138

Co-authored Publications

1. Resmi K.Bharathan, C. V. Midhun, M. M. Musthafa, M. Sreena, Silpa Ajaykumar, M. P. Farhana Thesni, Swapna Balakrishnan, Vafiya Thaslim T.T, **Shaima Akbar**, K. Nived, Akhil Ramesh, P. K. Anagha, V., Arunima Dev T., S. Keerthi E., K. S. Akshay, P. V. Arun and Ghugre, S. *Measurement of the sequential* 3α *process in the photodissociation of* ^{12}C. Phys. Rev. C 111 (6) 2025

2. Hajara K., M.M. Musthafa, N. Madhavan, S. Nath, Jagadish Gehlot, Gonika, C.V. Midhun, **Shaima Akbar** , Fathima Shirin Shana , A. Parihari , Rohan Biswas,

Amninder Kaur. *Entrance channel dependence of quasi fission in reactions leading to* ^{206}Po *compound nucleus.* Nucl. Phys. A 1042 (2024) 122789

3. K. Hajara, M. M. Musthafa , C. V. Midhun, **Shaima Akbar**, P. T. M. Shan, N. Madhavan, S. Nath , J. Gehlot, Gonika, Rohan Biswas, F. S. Shana, Amninder Kaur, Prashant N. Patil. *Evaporation residue cross section measurements for the* ^{30}Si+^{176}Yb *reaction.* Phys. Rev. C 105, 044619 (2022)

4. C. V. Midhun, M. M. Musthafa, S. V. Suryanarayana, T. Santhosh, A. Baishya, P. N. Patil, A. Pal, P. C. Rout, S. Santra, R. Kujur, Antony Joseph, **Shaima Akbar**, Hajara. K., P. T. M. Shan, Satheesh B., Y. Sawant, B. V. John, E. T. Mirgule, K. C. Jagadeesan, and . Ganesan. *Impact of* ^{7}Be *breakup on the* ^{7}Li(p,n) *neutron spectrum.* Phys. Rev. C 104, 054606 (2021)

5. Midhun C. V., Musthafa M. M., **Shaima Akbar**, Swapna Lilly Cyriac, Sajeev Sachin, Antony Joseph, Jagadeesan K. C., Suryanarayana S. V. and Ganesan S. *Spectroscopy of High-Intensity Bremsstrahlung Using Compton Recoiled Electrons.* Nucl. Sci. Eng.194(3):207–212,2020

Conference Proceedings

1. Shaima Akbar, M.M Musthafa, C.V Midhun, S.V Suryanarayana. Investigation of spin-parity conditions for the photonuclear reaction using surrogate ratio method. Proceedings of the DAE Symp. on Nucl. Phys. 68 (2024)

2. Shaima Akbar, M.M. Musthafa, C.V. Midhun, Antony Joseph, Swapna Lilly Cyriac, K.C. Jagadeesan *Integral cross section of* $^{19}F(\gamma,n)^{18}F$ *reaction at 14 MeV bremsstrahlung photon.* Proceedings of the DAE Symp. on Nucl. Phys. 67 (2023)

3. Shaima Akbar, M.M Musthafa, C.V Midhun, S.V Suryanarayana, Jyoti Pandey. *Determination of* $^{58}Co(\gamma,xp)$*cross section via the surrogate ratio method.* 8th International Conference on Women in Physics, 10-14 July 2023.

4. Shaima Akbar, M.M. Musthafa, C.V. Midhun, Antony Joseph, Swapna Lilly Cyriac, K.C. Jagadeesan. *Re-utilization and Transmutation of long lived* ^{99}Tc *radio isotope via Photon induced nuclear reactions.* 23rd National Symposium on Radiation Physics (NSRP-23), January 19 – 21, 2023

5. Shaima Akbar, M.M. Musthafa, C.V. Midhun, Resmi K. Bharathan, Sreena M., K.C. Jagadeesan. *Measurement and analysis of* $^{19}F(\gamma,n)^{18}F$ *reaction.* Proceedings of the DAE Symp. on Nucl. Phys. 66 (2022)

6. Shaima Akbar, M.M. Musthafa, C.V. Midhun, Antony Joseph, Swapna Lilly Cyriac, K.C. Jagadeesan. *The Photo-Activation based production of* $^{99}Tc^{m}$. DST-PURSE supported Satellite Symposia on Physical Sciences, Life Sciences, Chemical Sciences, and Mathematical-Statistical-Computational Sciences held at Bharathiar University on September 13-15 2022

7. Shaima Akbar, Jyoti Pandey, M.M. Musthafa, Midhun C.V., Bhawna Pandey, S.V. Suryanarayana, B.K. Nayak, H.M Agrawal, S. Santra, Antony Joseph, and K.C Jagadeesan. *Determination of excitation function of* $^{61}Ni(\gamma,xp)$ *reaction using surrogate ratio method.* Proceedings of the DAE Symp. on Nucl. Phys. 64 (2019)

8. Akhil Ramesh, M.M. Musthafa, Midhun C.V., Shaima Akbar, S.S. Ghugre. *Validating Spin-Parity conditions for neutron capture cross sections using surrogate Techniques.* Proceedings of the DAE Symp. on Nucl. Phys. 68 (2024)

9. Nived K, Midhun C.V, M.M. Musthafa, Resmi K. Bharathan, Vafiya Thaslim T.T , Swapna Balakrishnan, Akhil Ramesh, Arunima Dev T.V, Anagha P.K, Shaima Akbar, Drisya Karinkuzhi and Irfana Thasni A.K. *Direct Measurement of* $^{7}Li(\gamma,\alpha)t$ *cross sections.* Proceedings of the DAE Symp. on Nucl. Phys. 68 (2024)

10. Resmi K Bharathan, Midhun CV, Musthafa MM, Sreena M, Silpa Ajaykumar, Farhana Thesni MP, Swapna B, Vafiya TT , Shaima A, Nived K, Akhil R, Keerthi ES, Akshay KS, Arun PV. *Direct Measurement of* $^{12}C(\gamma,\alpha)\ ^{8}Be\rightarrow 3\alpha$ *Cross Sections.* Proceedings of the DAE Symp. on Nucl. Phys. 67 (2023)

11. Sreena M, Midhun CV, Musthafa M.M, Resmi K Bharathan, Farhana Thesni M P, Swapna B, Vafiya T T, Shaima A, Nived K, Akhil R, Keerthi E S, Silpa Ajaykumar, Akshay K S, Arun P V. *Inclusive* α *Spectrum from* $^{12}C(\gamma,\alpha)$ *Reaction.* Proceedings of the DAE Symp. on Nucl. Phys. 67 (2023)

12. C. V. Midhun, M. M. Musthafa, S. V. Suryanarayana, H. Gokul Das, A. Shaima, K. Hajara, Joseph Antony, T. Santhosh, A. Baishya, A. Pal, P. C. Rout, S. Santra, P. T. M. Shan, B. V. John, K. C. Jagadeesan, S. Ganesan. *On the estimation of* $^{6}Li(n,\gamma)$ *cross sections*, Proceedings of the DAE Symp. on Nucl. Phys. 66 (2022)

13. C.V Midhun, M.M Musthafa, Shaima Akbar, S.V Suryanarayana, K.C Jagadeesan, N.T Rijin, *Monitor Controlled Single Projection Approach for Cross Section Unfolding*, Proceedings of the DAE Symp. on Nucl. Phys. 66 (2019).

14. Siji M, Syama G Nair, Midhun C V, Shaima Akbar, Musthafa M M, Ganesan S, *Re-Estimation of Cross section data for the IAEA EXFOR ID:40803 for* $^{232}Th\,(n,\gamma)^{233}Th$ *using covariance analysis technique.* Proceedings of the DAE Symp. on Nucl. Phys. 65 (2018).

15. Syama G Nair, Siji M, Midhun C V, Shaima Akbar, M. M Musthafa, S Ganesan. *Re-Estimation of Cros section data for the IAEA EXFOR ID:40803 for* $^{238}U(n,\gamma)^{239}U$ *using covariance analysis technique*, Proceedings of the DAE Symp. on Nucl. Phys. 65 (2018).

Chapter 1

Introduction

The discovery of radioactivity by Henri Becquerel in 1896 marked a remarkable opening for the field of nuclear physics[1], though the concept of nucleus was not explored at that time. This observation happened accidentally, when he left a material containing uranium in front of a photographic plate. Building on Becquerel's work, extensive research by Marie Curie, Rutherford, and others led to significant discoveries. The detailed exploration of the nucleus, its nucleons, and their behavior continues through the use of nuclear reaction experiments. Conducting a nuclear reaction allows scientists to understand nuclear interactions, structure, angular momentum, spin, parity, and the forces between nucleons. A nuclear reaction relies on a specific combination of a projectile and a target, with the projectile directed toward the stationary target. However, in certain experiments, continuously moving targets are also employed. In both setups, the interaction between the projectile and the target results in the emission of ejectiles, which typically include neutrons, light-charged particles, and radiation. The remaining entity after the reaction, the residual nucleus, is usually in an excited state. Careful observation of these ejectiles and the residual nucleus provides crucial insights into the nucleus, and the involved mechanism within the nucleus.

To explain the mechanism of nuclear reactions, Niels Bohr introduced the concept of the compound nucleus in 1936[2]. This model considers the formation of an intermediate state through the fusion of the projectile and the target nucleus, and this intermediate state is the compound nucleus. The energy of the projectile particle is distributed among the compound nucleus, which gradually decays to its final state. The compound nuclear process takes place over a longer time scale as the incident particle moves through the target nucleus. Bohr suggested that, in this two-step process, the decay of the compound nucleus does not depend on the initial formation. The theory is known as Bohr's hypothesis or the independence hypothesis. In 1950, S.N. Goshal verified the independence hypothesis experimentally[3]. He formed the same compound nucleus ^{64}Zn, via two different pathways ^{63}Cu+p and ^{60}Ni+α. The compound nucleus was populated at the same excitation energy by suitably adjusting the incident energy of both the proton and the alpha particle in the two different pathways. The outgoing channels, such as ^{62}Zn+2n, ^{63}Zn+n, and ^{62}Cu+np, were analyzed to determine the excitation functions corresponding to the reaction channels. It was confirmed that the compound nucleus formed through different pathways does not retain information about its formation. However, the compound nuclear theory fails to explain the underlying physics above certain incident energies in specific systems. It was later identified that above the compound nuclear energy regime, direct reactions occur, which typically happen on a faster time scale. In a direct nuclear reaction, the incident nucleon interacts only with specific degrees of freedom, whereas in a compound nuclear reaction, numerous collisions occur within the target.

1.1 Photonuclear reactions - An overview

Photonuclear reactions are the specific classification of nuclear reactions in which projectile particles are photons and the ejectile particles may be a photon, a nucleon, a nucleus, or any combination of these. In this type of reaction, photons interact with the atomic nuclei and are absorbed by them, thereby photons ($\gamma\prime$), protons (p), neutrons (n), or heavily charged particles will be ejected from the nuclei. A schematic representation of photonuclear reaction is shown in Fig. 1.1. An elastic (γ, γ) or inelastic $(\gamma, \gamma\prime)$ photon scattering is prominent below particle separation energy, and if it is above the particle separation energy, particle emission occur. Common channels for photon induced reactions include (γ,n), (γ,2n), (γ,p), and photo-fission. The most critical aspect of these reactions is the

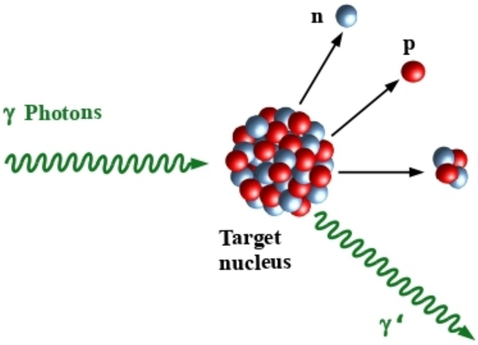

Figure 1.1: Schematic representation of photonuclear reaction

photon source used in experiments. Experimental photonuclear data are typically obtained through activation analysis using a bremsstrahlung photon source[4]. In activation analysis, a sample is irradiated by photons, and the resulting activity induced within the sample, is measured with a suitable detector. Recent advances in the field now enable online measurements of photonuclear reactions.

The photon sources used, in the early photon induced reactions have generally been produced in nuclear excitations or electromagnetic processes. The first known experiment utilizing a photon beam was performed in 1934 by Chadwick and Goldhaber[5]. They have used 2.615 MeV decay gamma from ^{208}Pb as a source, and estimated the neutron mass through the photo-disintegration of deuterium into proton and neutron. Various groups have conducted a series of experiments utilizing the photons emitted from nuclear reactions over the years. Among these, the experiment performed by Bothe and Gentner[6] using 17 MeV gamma ray produced in the ^{7}Li(p,γ) reaction was the first to utilize proton induced gamma beam to study Giant Dipole Resonance (GDR) studies on various isotopes. Following this, certain photonuclear reactions were performed by using energetic gamma rays produced via the proton induced nuclear reactions such as ^{19}F(p,$\alpha\gamma$) and ^{3}He(p,γ). However, due to the emission of the associated α particle, an energy spread of about 130 keV was also observed in the emitted gamma lines.

Similar to proton capture, various groups also used certain neutron capture reactions to study photonuclear reactions in the early years[7–9]. L. Green and D. J. Donahue[8] studied the photoneutron cross sections of ^{181}Ta, ^{7}Li, ^{6}Li, ^{13}C, and ^{10}B using the photons produced via thermal neutron capture. However, a low-energy spread of the γ-lines is observed in neutron capture gamma-rays. Additionally, it is only possible to work within a restricted energy range (less than 10 MeV) for the photon source, which further limits the study of photonuclear reactions involving only gamma rays and neutrons in the exit channel. Later, Knowles[10] introduced the idea of a monochromatic polarized photon beam to study nuclear resonances. The underlying principle is the Compton scattering of neutron capture γ-rays produced by placing targets such as Ni in the high thermal neutron flux region inside the reactor. However, the method inherits certain serious background issues.

Alternatively, Baldwin and Klaiber first used the continuous spectrum of γ-ray in 1947 to study the properties of GDR[11]. They have used the betatron to accelerate electrons and produced bremsstrahlung photons in the energy range of 10-100 MeV. With the advent of bremsstrahlung X-rays, numerous photonuclear experiments were explored by various groups. A stable and intense photon source produced via Van De Graaff accelerator with the electron of variable energy lead by F.R Metzger provided a better quality in the photonuclear data[12]. The development of high-current electron linear accelerators[13] and superconducting electron linear accelerators (S-DALINAC)[14] contributed to the advancement of photon induced nuclear reactions using bremsstrahlung photon beam. The S-DALINAC at the Darmstadt High-Intensity Photon Setup (DHIPS),[15] at TU Darmstadt, accelerates electrons with a maximum energy of 10 MeV and current 60μA. In this facility, the bremsstrahlung photons with a flux around 10^3 photons/(eV cm^2 s) have been generated by using a 14 mm thick rotating Cu target. At the Helmholtz-Zentrum Dresden-Rossendorf in Germany, the γ-ELBE facility uses a superconducting electron linac and niobium as a converter target to produce bremsstrahlung photons up to 13 MeV[16]. At the Flerov Laboratory of the JINR in Dubna, Russia, a tungsten with a thickness of 30 mm is used as the radiator target[17]. In this facility, they achieved a total integrated photon flux of around 10^{14} photons/s utilizing a microtron (MT-25). The Lawrence Livermore Laboratory in USA achieved similar output using a tungsten target. Other research laboratories such as the High Voltage Research Laboratory (HVRL) at MIT, NSC KIPT in Kharkiv, Ukraine, Idaho Accelerator Center (IAC) at Idaho State University, USA, and the Turkish Accelerator and Radiation Facility (TARLA) in Ankara, Turkey, were developed the bremsstrahlung photon source using electron linac for reaction purpose. Later, the bremsstrahlung monochromator technique was introduced to obtain a photon beam with a notably small energy interval. The energy of the bremsstrahlung photons can be determined by tagging with the associated decelerated electrons[18, 19]. However, the coincidence rate between the electron and the product radiation limits the technique to explore its application in a large area of photonuclear reactions.

To facilitate more detailed spectroscopic studies using photon beams, quasi-monoenergetic photons produced via positron annihilation in-flight technique were developed. The advantage of a quasi-monochromatic photon beam over a bremsstrahlung beam is that the latter is energy-tunable and minimizes low energy backgrounds. The production of positron annihilation in-flight photons was first published in 1953 by Colgate and Gilbert[20], and they measured the cross section for 50, 100, and 200 MeV incident positron beam. They confirmed the annihilation of photons by detecting the disappearing positrons in coincidence with the radiation emitted. This method was used at various research facilities viz. Livermore[21], Saclay[22], and Giessen[23] to study the photonuclear reactions using annihilation photon. Later, fully polarized, high intense, quasi-monoenergetic photon beams were generated by the Laser Compton Backscattering technique by various groups[24, 25]. The idea of Compton backscattered photon production was then explored by various groups and developed high intense high flux photon beam. The Ladon project, implemented at Frascati national laboratory[26–30] was the first among them to use high flux γ-ray Compton source for the nuclear physics research activities. The success of Ladon project encouraged various other groups in United states[31], France[32], Russia[33–36] and Japan[37, 38] to begin the Compton Scattered γ-ray facilities. The High-Intensity Gamma-ray Source (HIγS)[31] facility developed at

Duke University became the first dedicated facility for Compton γ-ray source. The facility ensures a highly intense, highly polarized, and nearly monochromatic source with a wide energy band of up to 100 MeV, with the use of high intense Free-Electron Laser (FEL) as the photon driver. Another Laser Compton Scattered (LCS) photon facility at the Extreme Light Infrastructure - Nuclear Physics (ELI-NP) in Romania offers a tunable photon beam up to 20 MeV, with further development underway [39, 40].

Along with the development of photon sources, advancement in the detector set up also contributed in the photonuclear research. The multiplicities, yields, angular distribution and the spectra of neutrons emitted in the photonuclear reactions are analysed utilizing the neutron detectors. Conversion of neutrons using the reactions ^{10}B(n,α)^{7}Li, ^{6}Li(n,α)^{3}H, or ^{3}He(n,p)^{3}H in to charged partcles after thermalization is one of the procedure adopted in determining the photoneutron cross section. Neutron detectors such as liquid scintillators or proportional counters filled with ^{3}He or ^{10}BF$_3$ embedded in polyethelene or paraffin leads to the measurement of photoneutrons essential for the GDR studies, particularly in medium and heavy nuclei. To explore the level structure of a nucleus, Nuclear Resonance Fluoroscence (NRF) effect, excitations strengths, gamma spectroscopy is the crucial one. At γELBE[16] and at DHIPS facility[15], NRF measurements are performed using the high resolution, high purity HPGe detector along with BGO scintillator for active Compton-background suppression. HIγS[31] facility is using γ^3 setup sonsisting of 4 HPGe and 4 LaBr$_3$(Ce) detectors for $\gamma - \gamma$ coincidence measurements. Other gamma detectors such NaI and BGO are also used in many facilities. Along with neutron and gamma detectors, charged particle detectors are used in photonuclear experiments above charged particle thresholds. Silicon strip detectors are generally being used for the studies of charged particle emission. Large-area annular Silicon Detector Array (SIDAR)[41] at HIγS[31] facility and 4π array of Si strip detectors called ELI Silicon Strip Array (ELISSA), at ELI-NP[42] are the two dedicated charged particle detector setups available.

1.2 Photonuclear reactions in medical field

A major application of photon induced nuclear reaction falls in the nuclear medicine field. The nuclear isotopes useful for therapeutic and diagnostic purposes are generally called medical isotopes. Generally, the short-lived isotopes, emitting either gammas or positrons, are for diagnostic purposes and the long-lived ones are used for therapeutic purposes. Specifically, SPECT analysis is performed by γ emitters, Positron Emission Tomography (PET) scanning is done with β^+ emitters, and for cancer therapy, β^-, α emitters are used. Isotopes such as ^{18}F, ^{99}Tc,^{67}Cu,^{47}Sc, ^{22}Na ^{60}Co, ^{177}Lu, ^{225}Ac, ^{227}Ac, ^{161}Tb, ^{155}Tb etc are currently using in the medical field[43–45]. Some isotope pairs of the same element have added advantages. One of the isotopes is useful for diagnostic purposes, and the other for therapeutic purposes. These medical isotopes are usually produced via cyclotrons or reactors, which are then safely packed and transported to the required facilities[46]. However, the age of the research reactors and the switching of Highly Enriched Uranium (HEU) to Low Enriched Uranium (LEU) hindered the supply of these isotopes recently[44]. An alternative to reactor production is that, some of them can be produced at the therapeutic centers utilizing the medical linac facility available to them. Various research is being carried out by researchers to figure out the possibility of producing the medically required isotopes via photonuclear reactions[47, 48]. The feasibility of producing the radioisotopes ^{141}Ce and ^{159}Gd through the reactions ^{142}Ce(γ,n)^{141}Ce and ^{160}Gd(γ,n)^{159}Gd at 10 MeV using a medical linac facility was reported by R. Ghosh *et al.*[49]. G.H. Hovhannisyan *et al.*[43] studied the production of the radioisotope ^{67}Cu via a photonuclear reaction and achieved a specific activity of 4.75 μCi/(μA h g) at a 40 MeV bremsstrahlung endpoint energy. Thus, the precise knowledge of photon induced reaction data is important in the medical field.

Moreover, the knowledge of the interaction of photons with the biological samples is of great importance since we are using photon beams for treatment purposes. The dose absorbed by the patient during the radiotherapy treatment should be calculated, as the high-energy bremsstrahlung may induce further nuclear reactions within the patient's body.

1.3 Various photon sources for photonuclear experiments

The history behind the development of photon sources was discussed in the previous section. Here, we will discuss different photon sources available in the world and the theory behind their production in detail.

1.3.1 Bremsstrahlung photons

Bremsstrahlung radiation is basically the breaking radiation, generated when a beam of high-energy electrons passes near a nucleus[11, 50]. The kinetic energy resulting from the deceleration of the electron will convert into radiation with energy equivalent to the energy of the decelerating electron. Hence, we will get a spectrum of photons with maximum energy, known as endpoint energy, extending up to maximum electron energy. Usually, electrons are accelerated via betatron or synchrotron and allowed to incident on a photon-producing target. The bremsstrahlung photon thus obtained is then collimated and allowed to strike the required target under study. The bremsstrahlung photons produced via the passage of energetic electrons are provided in Fig. 1.2. The shape of the bremsstrahlung photon spectrum produced from a thin target can be evaluated by the Schiff formula[51]. However, in recent times, different Monte Carlo simulation codes have been used for the evaluation of the bremsstrahlung spectrum[16, 52, 53]. The yield corresponding to the reaction will be obtained though the bremsstrahlung photon induced reactions, which is given by,

$$Y(E_0) = N_R \int_{E_{th}}^{E_0} \frac{\sigma(E_\gamma)}{E_\gamma} S(E_0, E_\gamma) dE_\gamma \tag{1.1}$$

where N_R is the normalization factor, $\sigma(E_\gamma)$ is the cross section of the required reaction and $S(E_0,E_\gamma)$ is the bremsstrahlung energy spectrum. A typical bremsstrahlung energy spectrum, as described in [54], is shown in Fig. 1.3. Here, E_γ is the energy of photon, E_{th}

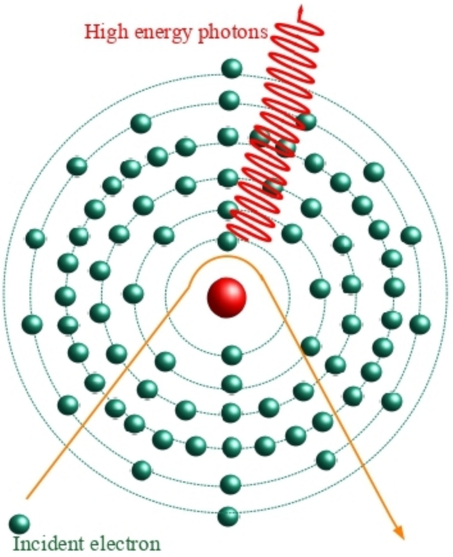

Figure 1.2: Schematic representation for the production of bremsstrahlung photons

is the threshold energy for the reaction to occur and E_0 is the end-point energy. The photon energies can be varied by changing the energy of incident electron. The so-obtained photonuclear yield then underwent the procedure of spectrum deconvolution to determine the actual cross section. The popular techniques used for photon spectrum unfolding are the Photon difference method[55], the Penfold Leiss method[56], and the Regularization method[57]. As the name suggests, the photon difference method considers the difference between two nearby endpoint photon energy spectra to be mono-energetic. In the Penfold Leiss method, the integral term in the yield expression (Eq. 1.1) is replaced by a set of linear expressions. Different regularization methods, including the Statistical regularization method, the Tikhonov method, the second difference method, and the Cooks least structure method are employed to deconvolute the bremsstrahlung spectrum. Usually, in these methods, the mean square difference between the cross section and its estimator is reduced under the assumption that the cross section is smooth.

Even though the bremsstrahlung technique is a widely accepted and employed method in photonuclear reactions, certain shortcomings exist in this method. The counting statistics and the accelerator parameter play a significant role in determining accurate yield for

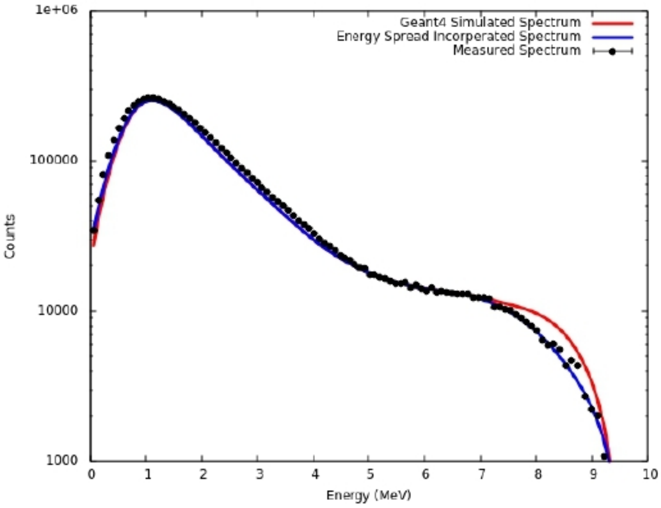

Figure 1.3: Bremsstrahlung energy spectrum showing the characteristic continuous photon energy distribution resulting from electron deceleration [54].

small energy bins, particularly above the GR region. Owing to the continuous nature of the bremsstrahlung spectra, one cannot directly measure the differential cross section of the reaction. Further, deconvolution of the obtained bremsstrahlung spectra introduces large uncertainties in the measured cross section.

1.3.2 Positron annihilation in-flight photons

Quasi-monochromatic annihilation (QMA) photon beams are generated via the positron annihilation in-flight technique, in which the mono-energetic positrons annihilate with the electron at rest. The positrons for this method are generated via the pair production of bremsstrahlung photons. High Z materials such as tungsten, gold, tantalum, and platinum are usually used for the production of bremsstrahlung photons. These materials can withstand the heat produced during the bremsstrahlung photon generation. The so-produced positron beam is then allowed to incident on thin low Z material, creating a peak of annihilation photon and corresponding bremsstrahlung spectra. The advantage of low Z material is that the bremsstrahlung spectrum and the annihilation photon peak can be separated. Typically, in the positron annihilation in-flight method, two photons are emitted isotropically with energy equal to mc^2 individually. But if we allow the high-velocity positron to annihilate in the flight path itself with the electron, the photons may

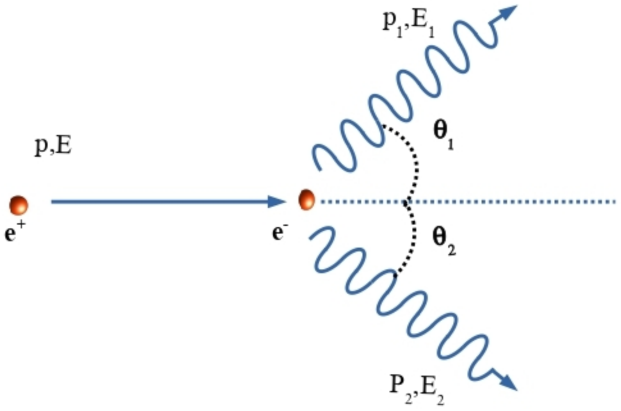

Figure 1.4: Schematic representation for the production of photons via positron annihilation method

emit directionally in the laboratory frame. A schematic representation of the positron annihilation with the electron is shown in Fig. 1.4. Here, E and p are the kinetic energy and momentum of the positron annihilating with the electron at rest, while E_1, p_1, E_2, and p_2 are the kinetic energy and momentum of the emitted photons at angles θ_1 and θ_2, respectively.

The photonuclear reactions using the positron annihilation in-flight photons are usually carried out in three steps.

1. First measure the photon induced yields corresponding to both annihilation photon and bremsstrahlung of positron.
2. Then, measure the yield corresponding to the photon produced in the electron bremsstrahlung.
3. Finally, subtracting the bremssstrahlung spectra correspond to electron from the combined spectrum of photons produced via positron bremsstrahlung and positron annihilation.

In the last step, it is assumed that, both the bremsstrahlung spectrum generated by positron and electron are identical. The cross section of a photonuclear reaction resulting from the interaction of annihilation photon with the nucleon can be represented as,

$$\sigma(E_\gamma) = Y^{e^+}(E) - Y^{e^-}(E) \tag{1.2}$$

where $Y^{e^+}(E)$ is the reaction yield obtained from the interaction of photons formed via positron bremsstrahlung and $Y^{e^-}(E)$ is the reaction yield obtained from the interaction of photons formed via electron bremsstrahlung. The annihilation cross section and the yield corresponding to the photon induced reaction tend to increases linearly with the energy of the incident positron.

The major disadvantage of this method as compared to bremsstrahlung photon is that the intensity of the spectrum will be low due to the small cross section for pair production and pair annihilation. Further, the yield corresponds to unwanted photon produced through the interaction of positron bremsstrahlung also increases with energy of the positron. This will cause difficulty in subtraction process to obtain the actual cross section. Eventhough the QMA photon source can produce better energy resolution, the literature shows an over smoothened cross sections as compared to bremsstrahlung photons. Moreover, the photonuclear reactions performrd using QMA photons from different laboratories itself shows variations in the absolute cross section values.

1.3.3 Bresmsstrahlung tagged photons

Bremsstrahlung tagged photon facilities were developed to generate mono-energetic photon beams for application in GDR studies[58]. The advancement of sophisticated linear accelerators to accelerate electrons contributed to the progress of this technique. The mono-energetic electrons accelerated from the high current linear accelerators incident on a converting target result in the production of bremsstrahlung photons. During the bremsstrahlung photon production, if the converting target is sufficiently thin, the energetic electron will interact only once within the target. Hence, we can determine the photon energy by tagging the energy of the scattered electron. The scattered electrons are guided into the array of detectors by passing through deflecting magnets at the focal plane. A schematic representation for the production of photons via bresmsstrahlung

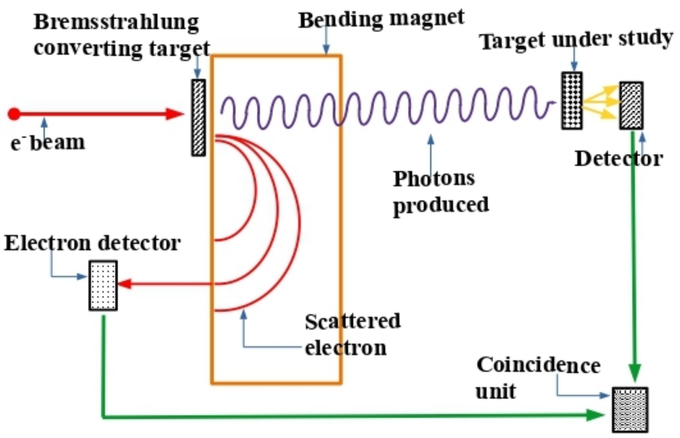

Figure 1.5: Schematic representation for the production of photons via bresmsstrahlung tagged facility

tagged facility is illustrated in Fig. 1.5. If E_e is the energy of the accelerated electron, E_s is the energy of the scattered electron, then the energy of the photon E_γ can be determined via the equation,

$$E_\gamma = E_e - E_s \tag{1.3}$$

Thus, tagging the scattered electrons with the photon enables the measurement of photon induced reactions with specified energies.

However, the usage of a considerably thin target for photon production results in the reduction of photon beam intensity. Consequently, the coincidence measurement becomes difficult. Further, the method demands the use of small solid angle neutron detectors with low efficiency, due to fast coincidence between scattered electrons and the photon.

1.3.4 Laser Compton back-scattered photons

Laser Compton back-scattering is the process of the production of highly intense, highly energetic, and tunable gamma rays by colliding relativistic electrons with the laser photons. An advantage of this method is that the produced photon beam shows a narrow spectral bandwidth. The production of photons via the Compton scattered laser method is schematically represented in the Fig. 1.6. Here P_e is the momentum of incoming electron,

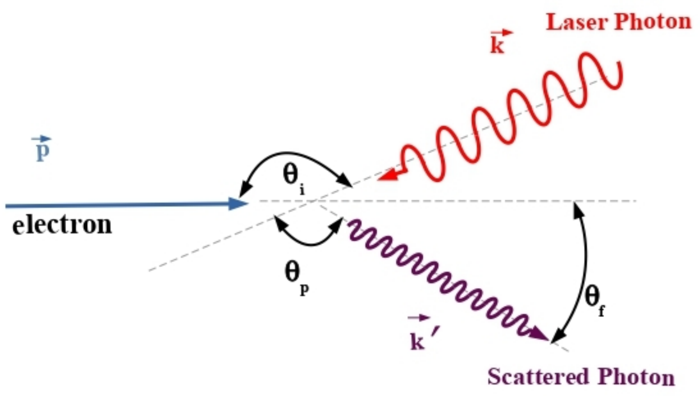

Figure 1.6: Schematic representation for the production of photons via laser Compton back scattering technique

$\hbar\vec{k}$ is the momentum of incident laser photon ($\vec{P_L}$) and $\hbar\vec{k'}$ is the momentum of scattered photon ($\vec{P_\gamma}$). The angle θ_i, θ_p, and θ_f are the angle at which the laser photon incident on the electrons, the angle of the scattered photon with respect to the incident electron, and the same with respect to the photon, respectively. The energy of the Compton Scattered photon can be written as

$$E_\gamma = \frac{(1-\beta cos\theta_i)E_L}{(1-\beta cos\theta_f)+(1-cos\theta_p)E_L/E_e} \tag{1.4}$$

where E_L is the energy of the laser, E_e is the energy of the electron and β is the velocity of electron to the speed of light. For a head on collision to occur θ_i must be equal to π and $\theta_p = \pi - \theta_f$. Hence the photon energy become

$$E_\gamma = \frac{(1+\beta)E_L}{(1-\beta cos\theta_f)+(1+cos\theta_f)E_L/E_e} \tag{1.5}$$

Thus the photon energy depends only on the scattering angle θ_f. The maximum photon energy that can be obtained through this method will be

$$E_\gamma^{max} \approx \frac{4\gamma^2 E_L}{1+4\gamma^2 E_L/E_e} \quad \approx \quad 4\gamma^2 E_L \quad at \quad \theta_f = 0$$

where $\gamma = 1/\sqrt{1-\frac{v^2}{c^2}}$ is the Lorentz factor of the incoming high-energy electron in the lab frame.

The advantage of the LCS photon source is that the energy of the photons at the backward angles can be varied by tuning the energy of the electrons or the laser photons. Hence, we will get a mono-energetic photon source. In addition, the photon obtained through the Compton scattering effect may preserve the polarization as same as the incident Laser. However, the properties of the electron beam will affect the quality of the photon beam produced. Thus, to ensure a highly energetic, less spread photon beam, high quality electron beam should be utilized.

1.4 Photonuclear data libraries

All the experimental photonuclear reaction data viz, photo absorption cross section, photo-proton production cross section, photo-neutron cross section, yields, and partial cross sections, are available in the Experimental Nuclear Reaction Data (EXFOR) library[59]. EXFOR is maintained by the Network of Nuclear Reaction Data Centers. First attempt to compile the photoneutron data was made by B.L. Berman in 1975. The work was published under the name ”Atlas of photoneutron cross sections obtained with mono-energetic photons” and later in 1988, this was modified by S.S Deitrich[60]. Looking into the application of photon induced data, an effort to put together all the available photon induced data was begun in 1983 by the Photonuclear Data Centre of the US National Bureau of Standards. This was the first project under the title ”Photonuclear Data - Abstract sheets 1955-1982”, coordinated by E.G Fuller and H. Gestenberg[61].

The International Atomic Energy Agency had organized a coordinated research project (IAEA CRP), in 1996, to evaluate photonuclear data produced by various groups. As a consequence, the 1999 Photonuclear Data Library was generated with 164 isotopes, within which most useful data using structural materials, biological materials, bremsstrahlung materials, and fissionable materials are incorporated. The advancement in the experimental facility and the production of new photon induced experiment data lead to the updation of this data library in 2014. In addition to the previous 164 isotopes, 46 isotopes with experimental data were also included in the updated evaluation. Other isotopes with no experimental data are also included utilizing model evaluations. Along with this, a photon strength function database is also available on the IAEA website. Other evaluated data libraries, including ENDF, JENDL, TENDL, and KAERI could provide photonuclear reaction data. They store the data based on the evaluation of existing experimental data for the neighboring nuclei by considering the discrepancies or by using suitable nuclear model analysis.

1.5 Motivation of the thesis

One of the major isotopes used in the diagnostic process is ^{99m}Tc, with half-life 6 hours, is the isomeric state of long-lived (10^5 Y)^{99}Tc. On an estimate, about 40 million procedures per year are performed with ^{99m}Tc, which constitute around 80% of all nuclear medicine procedures worldwide[44, 62]. The low energetic de-excitation gamma ray with energy 140 keV is useful for imaging purposes as it causes low exposure to the patient body. A large enough quantity of ^{99m}Tc is obtained from the beta decay of parent isotope ^{99}Mo with half-life 66 years, produced from the fission of ^{235}U in the HEU nuclear reactor. ^{99}Mo is also produced via the neutron induced reactions[63, 64]. Usually, in therapeutic centers, this is used as Mo/Tc generators, from which required technetium is extracted through the process known as elution[65]. Among worldwide production, distribution of ^{99}Mo is only possible with 6 reactors, most of which are very old. Reactor shutdowns cause difficulty in the availability of ^{99}Mo so as ^{99m}Tc. Fuel switching from HEU to LEU also causes a decrease in the amounts of ^{99}Mo. Furthermore, during the process of elution a small fraction of ^{99}Mo is co-eluted with ^{99m}Tc, which contaminates the medical isotope by the emission of energetic beta and gamma radiation. The ground state ^{99}Tc is found to be a radioactive waste formed due to the reactor operation and after treatment purpose at cancer therapy centres. The longer half-life of this isotope results in a longer time for natural transmutation, which could adversely affect the environment. Additionally, it would require large reservoirs to store these long-lived isotopes until their complete conversion into stable products.

Another important isotope in the medical field is ^{18}F. ^{18}F is a pure positron emitter used for PET scan[66]. In the medical field, the use of ^{18}F keeps increasing, indicating the huge demand for ^{18}F. Primarily, ^{18}F is produced via cyclotron using an enriched water target. Major reaction channels such as ^{18}O(p,n)^{18}F, ^{19}F(n,2n)^{18}F, ^{19}F(γ,n)^{18}F, and ^{16}O(t,n)^{18}F are available for the production of ^{18}F. Among these channels, ^{18}O(p,n)^{18}F is the widely used channel for the production of ^{18}F. Along with ^{18}F, several unwanted activation products are formed due to the bombardment of the primary proton beam and the energetic neutron produced in the reaction itself[67]. This, in turn, contaminates the ^{18}F isotope and causes patients to absorb extra doses. Transportation of the radioactive isotope to the hospitals is also a major issue, as the useful activity of the isotope will lost due to its shorter half-life. Hence alternate routes of producing these isotopes are to be explored. This is important as accelerators with high energy photon-electron linear accelerators (LINAC) are being installed in almost all nooks and corners of the country with hospitals having advanced facilities for radiation therapy. This will help local production of such isotopes and hence reduce the risk of safety and transportation. Presently very little data is available on photon induced reactions. Further the prediction of theoretical models of nuclear reactions differ from one another, still many of the reported measurements are not in good agreement.

Photonuclear reactions are important in the field of fission-fusion reactor technology. High energetic gamma radiations are produced inside the fission or fusion reactor due to the inelastic collision of neutrons with the atomic nuclei. Low energetic neutrons cause capture reactions, and high energetic neutrons cause nuclear breakup reactions. This, in turn, causes the de-excitation of the excited nucleus, which further leads to the generation of energetic photons inside the reactor. Luca Reali *et. al* [68, 69] recently evaluated the flux and energies of the photons generated inside the fission and fusion reactors. Energetic photons will interact with the structural materials inside the reactor and cause damage to the material.

R. Gandhi *et. al,*[70–72] B. Pandey *et.al,*[73] and J. Pandey *et. al,*[74] studied the damages to the structural material inside the reactors due to the irradiation of neutrons.

Major constituents of the stainless steel used as the structural material inside the reactor are Cr, Fe, and Ni. The neutron induced reactions on this material can produce other long-lived unwanted isotopes. The high flux, high energetic photons produced inside the reactor during reactor operation may further cause photon induced reactions on these isotopes. This will eventually damage the structural materials. The neutron induced structural damages on the so-produced ^{58}Co isotope have already been studied by R. Gandhi *et. al,*[71]. The study of structural damage caused by photon irradiation on the ^{58}Co isotope is also important for reactor concerns.

1.6 Objective of the thesis

1. To study the production feasibility of ^{99m}Tc isotope via the photonuclear reaction ^{99}Tc(γ, γ'), utilizing the medical linac facility.
2. To study the production feasibility of ^{18}F isotope via the photonuclear reaction ^{19}F(γ,n), utilizing the medical linac facility.
3. To determine the cross section of photon induced reaction ^{58}Co(γ,xp) via the indirect method called surrogate ratio technique.

Bibliography

[1] H. Becquerel. On the rays emitted by phosphorescence. *Comptes Rendus*, 122:420–421, 1896.

[2] N. Bohr. Neutron capture and nuclear constitution. *Nature*, 137:344–348, 1936.

[3] S. N. Ghoshal. An experimental verification of the theory of compound nucleus. *Physical Review*, 80:939–942, Dec 1950.

[4] C. Segebade, H. P. Weise, and G. J. Lutz. *Photon activation analysis.* Walter de Gruyter, 2011.

[5] J. Chadwick and M. Goldhaber. A nuclear photo-effect: Disintegration of the diplon by -rays. *Nature*, 134:237–238, Aug 1934.

[6] W. Bothe and W. Gentner. Atomumwandlungen durch γ-strahlen. *Zeitschrift für Physik*, 106(3-4):236 – 248, 1937. Cited by: 64.

[7] R. E. Welsh and D. J. Donahue. Photonuclear studies with monoenergetic gamma rays from thermal neutron capture. *Physical Review*, 121:880–885, Feb 1961.

[8] L. Green and D. J. Donahue. Photoneutron cross sections with monoenergetic neutron-capture gamma rays. *Physical Review*, 135:B701–B705, Aug 1964.

[9] R.R. Hurst and D.J. Donahue. Photonuclear cross sections with mono-energetic neutron-capture gamma rays. *Nuclear Physics A*, 91(2):365–368, 1967.

[10] J.W. Knowles and N.M. Ahmed. Atomic energy of canada limited report, 1966.

[11] G.C. Baldwin and G.S. Klaiber. Photo-fission in heavy elements. *Physical Review*, 71(1):3 – 10, 1947. Cited by: 172.

[12] F.R. Metzger. Electric dipole transitions from the 2.6-mev septuplet in bi209. *Physical Review*, 187(4):1680 – 1682, 1969. Cited by: 33.

[13] U. Kneissl. Photoexcitation of low-lying, isovector 1+ states in deformed nuclei. *Progress in Particle and Nuclear Physics*, 24:41–59, 1990.

[14] A. Richter. Probing the nuclear magnetic dipole response with electrons, photons and hadrons. *Progress in Particle and Nuclear Physics*, 34:261–284, 1995. Electromagnetic Probes and the Structure Hadrons and Nuclei.

[15] K. Sonnabend, D. Savran, J. Beller, M.A. Büssing, A. Constantinescu, M. Elvers, J. Endres, M. Fritzsche, J. Glorius, J. Hasper, J. Isaak, B. Löher, S. Müller, N. Pietralla, C. Romig, A. Sauerwein, L. Schnorrenberger, C. Wälzlein, A. Zilges, and M. Zweidinger. The darmstadt high-intensity photon setup (dhips) at the s-dalinac. *Nuclear Instruments and Methods in Physics Research Section A: Accelerators, Spectrometers, Detectors and Associated Equipment*, 640(1):6–12, 2011.

[16] R. Schwengner, R. Beyer, F. Dönau, E. Grosse, A. Hartmann, A.R. Junghans, S. Mallion, G. Rusev, K.D. Schilling, W. Schulze, and A. Wagner. The photon-scattering facility at the superconducting electron accelerator elbe. *Nuclear Instruments and Methods in Physics Research Section A: Accelerators, Spectrometers, Detectors and Associated Equipment*, 555(1):211–219, 2005.

[17] T. D. Thiep, Truong T. An, N. T. Khai, N. T. Vinh, P. V. Cuong, I. P. Gangrski, A.G. Belov, and O.D. Maslov. Determination of the total bremsstrahlung photon flux from electron accelerators by simultaneous activation of two monitors. *Physics of Particles and Nuclei Letters*, 9(8):648 – 655, 2012. Cited by: 7.

[18] J. S. O'Connell, P. A. Tipler, and P. Axel. Elastic scattering of 11.5—17.7-mev photons by au measured with a bremsstrahlung monochromator. *Physical Review*, 126:228–239, Apr 1962.

[19] P. Axel, K. Min, N. Stein, and D. C. Sutton. New resonances in photon transition strength functions. *Physical Review Letters*, 10:299–302, Apr 1963.

[20] S.A. Colgate and F.C. Gilbert. Electron-positron annihilation in flight. *Physical Review*, 89(4):790 – 792, 1953. Cited by: 12; All Open Access, Green Open Access.

[21] S.C. Fultz, R.L. Bramblett, J.T. Caldwell, N.E. Hansen, and C.P. Jupiter. Photoneutron cross sections for v51 and co59. *Physical Review*, 128(5):2345 – 2351, 1962. Cited by: 45.

[22] A. Veyssière, H. Beil, R. Bergère, P. Carlos, J. Fagot, A. Leprêtre, and J. Ahrens. The quasi-

monochromatic photon beam used in photoneutron experiments from 20–120 mev at the 600 mev saclay linac. *Nuclear Instruments and Methods*, 165(3):417–437, 1979.

[23] U. Kneissl, E.A. Koop, G. Kuhl, K.H. Leister, and A. Weller. The quasimonoenergetic photon facility at the giessen 65 mev electron linear accelerator. *Nuclear Instruments and Methods*, 127(1):1–10, 1975.

[24] O.F Kulikov, Y.Y Telnov, E.I Filippov, and M.N Yakimenko. Compton effect on moving electrons. *Physics Letters*, 13(4):344–346, 1964.

[25] C. Bemporad, R. H. Milburn, N. Tanaka, and M. Fotino. High-energy photons from compton scattering of light on 6.0-gev electrons. *Physical Review*, 138:B1546–B1549, Jun 1965.

[26] L Casano et al. Laser scanning components and techniques: design considerations. *Laser and Unconventional Optics Journal*, 55:3, 1975.

[27] G. Matone, P. Picozza, D. Prosperi, A. Tranquilli, R. Caloi, C. Schaerf, S. Frullani, and C. Strangio. *A monochromatic and polarized photon beam for photonuclear reactions. The ladon project at Frascati*, pages 149–164. Springer Berlin Heidelberg, Berlin, Heidelberg, 1977.

[28] L. Federici, G. Giordano, G. Matone, G. Pasquariello, P.G. Picozza, R. Caloi, L. Casano, M.P. De Pascale, M. Mattioli, E. Poldi, C. Schaerf, P. Pelfer, D. Prosperi, S. Frullani, and B. Girolami. The ladon photon beam with the esrf 5 gev machine. *Lettere al Nuovo Cimento*, 27:339 – 347, 1980.

[29] L. Federici, G. Giordano, G. Matone, G. Pasquariello, P.G. Picozza, R. Caloi, L. Casano, M.P. De Pascale, M. Mattioli, E. Poldi, C. Schaerf, M. Vanni, P. Pelfer, D. Prosperi, S. Frullani, and B. Girolami. Backward compton scattering of laser light against high-energy electrons: the ladon photon beam at frascati. *Il Nuovo Cimento B Series 11*, 59(2):247 – 256, 1980. Cited by: 96.

[30] D. Babusci, E. Cima, M. Iannarelli, E. Turri, F. Basti, I. Halpern, L. Casano, A. D'Angelo, D. Moricciani, P.G. Picozza, C. Schaerf, and B. Girolami. Taladon: a polarized and tagged gamma ray beam. *Nuclear Instruments and Methods in Physics Research Section A: Accelerators, Spectrometers, Detectors and Associated Equipment*, 305(1):19–24, 1991.

[31] V. N. Litvinenko, B. Burnham, M. Emamian, N. Hower, J. M. J. Madey, P. Morcombe, P. G. O'Shea, S. H. Park, R. Sachtschale, K. D. Straub, G. Swift, P. Wang, Y. Wu, R. S. Canon,

C. R. Howell, N. R. Roberson, E. C. Schreiber, M. Spraker, W. Tornow, H. R. Weller, I. V. Pinayev, N. G. Gavrilov, M. G. Fedotov, G. N. Kulipanov, G. Y. Kurkin, S. F. Mikhailov, V. M. Popik, A. N. Skrinsky, N. A. Vinokurov, B. E. Norum, A. Lumpkin, and B. Yang. Gamma-ray production in a storage ring free-electron laser. *Physical Review Letters*, 78:4569–4572, Jun 1997.

[32] D. Babusci, L. Casano, A. D'Angelo, P.G. Picozza, C. Schaerf, and B. Girolami. Project graal: the scientific case. *Il Nuovo Cimento A*, 103(1):1555–1576, 1990.

[33] A. A. Kazakov, G. Ya. Kezerashvili, L. E. Lazareva, V. G. Nedorezov, A. N. Skrinsky, A. S. Sudov, G. M. Tumaikin, and Yu. M. Shatunov. Fission of U-238 and Np-237 by intermediate energy gamma rays. *JETP Lett.*, 40:1271–1274, 1984.

[34] G.Ya. Kezerashvili, A.M. Milov, and B.B. Wojtsekhowski. The gamma ray energy tagging spectrometer of the rokk-2 facility at the vepp-3 storage ring. *Nuclear Instruments and Methods in Physics Research Section A: Accelerators, Spectrometers, Detectors and Associated Equipment*, 328(3):506–511, 1993.

[35] G. Ya. Kezerashvili, A. M. Milov, N. Yu. Muchnoi, A. N. Dubrovin, V. A. Kiselev, A. I. Naumenkov, A. N. Skrinsky, D. N. Shatilov, E. A. Simonov, V. V. Petrov, and I. Ya. Protopopov. ROKK-1M is the Compton source of the high intensity polarized and tagged gamma beam at the VEPP-4M collider. *AIP Conference Proceedings*, 343(1):260–263, 09 1995.

[36] G.Ya. Kezerashvili, A.M. Milov, N.Yu. Muchnoi, and A.P. Usov. A compton source of high energy polarized tagged γ-ray beams. the rokk-1m facility. *Nuclear Instruments and Methods in Physics Research Section B: Beam Interactions with Materials and Atoms*, 145(1):40–48, 1998.

[37] T. Nakano, H. Ejiri, M. Fujiwara, T. Hotta, K. Takanashi, H. Toki, S. Hasegawa, T. Iwata, K. Okamoto, T. Murakami, J. Tamii, K. Imai, K. Maeda, K. Maruyama, S. Daté, M.M. Obuti, Y. Ohashi, H. Ohkuma, and N. Kumagai. New projects at spring-8 with multi-gev polarized photons. *Nuclear Physics A*, 629(1):559–566, 1998. Quark Lepton Nuclear Physics.

[38] T. Nakano, J.K. Ahn, M. Fujiwara, H. Kohri, N. Matsuoka, T. Mibe, N. Muramatsu, M. Nomachi, H. Shimizu, K. Yonehara, M. Yosoi, T. Yorita, W.C. Chang, C.W. Wang, S.C. Wang, Y. Asano, T. Hotta, Y. Sugaya, R. Zegers, S. Daté, N. Kumagai, Y. Ohashi, H. Ohkuma, H. Toyokawa, T. Iwata, M. Miyabe, Y. Miyachi, A. Wakai, K. Imai, T. Ishikawa, M. Miyabe,

T. Sasaki, H. Kawai, T. Ooba, Y. Shiino, M. Wada, H.C. Bhang, Z.Y. Kim, A. Sakaguchi, M. Sumihama, K. Hicks, H. Akimune, T. Matsumura, C. Rangacharyulu, and S. Makino. Multi-gev laser-electron photon project at spring-8. *Nuclear Physics A*, 684(1):71–79, 2001. Few-Body Problems in Physics.

[39] K. A. Tanaka, K. M. Spohr, D. L. Balabanski, S. Balascuta, L. Capponi, M. O. Cernaianu, M. Cuciuc, A. Cucoanes, I. Dancus, A. Dhal, B. Diaconescu, D. Doria, P. Ghenuche, D. G. Ghita, S. Kisyov, V. Nastasa, J. F. Ong, F. Rotaru, D. Sangwan, P.-A. Söderström, D. Stutman, G. Suliman, O. Tesileanu, L. Tudor, N. Tsoneva, C. A. Ur, D. Ursescu, and N. V. Zamfir. Current status and highlights of the ELI-NP research program. *Matter and Radiation at Extremes*, 5(2):024402, 03 2020.

[40] S. Gales, D. L. Balabanski, F. Negoita, O. Tesileanu, C .A. Ur, D. Ursescu, and N. V. Zamfir. New frontiers in nuclear physics with high-power lasers and brilliant monochromatic gamma beams. *Physica Scripta*, 91(9):093004, aug 2016.

[41] D. W. Bardayan, J. C. Blackmon, C. R. Brune, A. E. Champagne, A. A. Chen, J. M. Cox, T. Davinson, V. Y. Hansper, M. A. Hofstee, B. A. Johnson, R. L. Kozub, Z. Ma, P. D. Parker, D. E. Pierce, M. T. Rabban, A. C. Shotter, M. S. Smith, K. B. Swartz, D. W. Visser, and P. J. Woods. Observation of the astrophysically important 3^+ state in ^{18}ne via elastic scattering of a radioactive ^{17}f beam from ^1h. *Physical Review Letters*, 83:45–48, Jul 1999.

[42] O. Tesileanu, M. Gai, A. Anzalone, C. Balan, J.S. Bihalowicz, M. Cwiok, W. Dominik, S. Gales, D.G. Ghiță, Z. Janas, D.P. Kendellen, M. la Cognata, C. Matei, K. Mikszuta, C. Petcu, M. Pfützner, T. Matulewicz, C. Mazzocchi, and C. Spitaler. Charged particle detection at eli-np. *Romanian Reports in Physics*, 68:S699 – S734, 2016. Cited by: 39.

[43] G.H. Hovhannisyan, T.M. Bakhshiyan, and R.K. Dallakyan. Photonuclear production of the medical isotope 67cu. *Nuclear Instruments and Methods in Physics Research Section B: Beam Interactions with Materials and Atoms*, 498:48–51, 2021.

[44] *Photonuclear Production of Radioisotopes*. Number 2051 in TECDOC Series. International Atomic Energy Agency, Vienna, 2024.

[45] C. S. Loveless, L. L. Radford, S. J. Ferran, S. L. Queern, M. R. Shepherd, and S. E. Lapi. Photonuclear production, chemistry, and in vitro evaluation of the theranostic radionuclide 47sc. *EJNMMI Research*, 9:110840, 2019.

[46] *Manual for Reactor Produced Radioisotopes*. Number 1340 in TECDOC Series. International Atomic Energy Agency, Vienna, 2003.

[47] Valeriia N. Starovoitova, L. Tchelidze, and D. P. Wells. Production of medical radioisotopes with linear accelerators. *Applied Radiation and Isotopes*, 85:39–44, 2014.

[48] Adam K., Andrzej O., and Maria S. Application of therapeutic linear accelerators for the production of radioisotopes used in nuclear medicine. *Polish Journal of Medical Physics and Engineering*, 28(3):107–116, 2022.

[49] R. Ghosh, S. Badwar, B. Lawriniang, S. S. Yerraguntla, H. Naik, Y. Naik, S. V. Suryanarayana, B. Jyrwa, and S. Ganesan. Measurement of photo-neutron cross-sections of gd and ce using bremsstrahlung with an end-point energy of 10 mev. *Journal of Radioanalytical and Nuclear Chemistry*, 314:1983–1990, 2017.

[50] E. Hayward and E.G. Fuller. Photon self-absorption and scattering by the 15.1-mev level in c12. *Physical Review*, 106(5):991 – 995, 1957. Cited by: 13.

[51] L.I. Schiff. Energy-angle distribution of thin target bremsstrahlung. *Physical Review*, 83(2):252 – 253, 1951. Cited by: 361.

[52] S. Lindenstruth, A. Degener, R.D. Heil, A. Jung, U. Kneissl, J. Margraf, H.H. Pitz, H. Schacht, U. Seemann, R. Stock, and C. Wesselborg. Measurements and simulations of low energy, thick target bremsstrahlung spectra. *Nuclear Instruments and Methods in Physics Research Section A: Accelerators, Spectrometers, Detectors and Associated Equipment*, 300(2):293–296, 1991.

[53] Kazuaki K., Koji O., Takashi N., Masashi T., Kouichi S., Takashi K., and Yoshiaki K. Angular distribution of bremsstrahlung from copper and tungsten targets bombarded by 18, 28, and 38mev electrons. *Journal of Nuclear Science and Technology*, 47(3):286–294, 2010.

[54] C. V. Midhun, M. M. Musthafa, S. Akbar, C. Lilly, S. Sajeev, A. Joseph, K.C. Jagadeesan, S. V. Suryanarayana, and S. Ganesan. Spectroscopy of high-intensity bremsstrahlung using compton recoiled electrons. *Nuclear Science and Engineering*, 194:1–6, 11 2019.

[55] H. E. Johns, L. Katz, R. A. Douglas, and R. N. H. Haslam. Gamma-neutron cross sections. *Physical Review*, 80:1062–1068, Dec 1950.

[56] A. S. Penfold and J. E. Leiss. Analysis of photonuclear cross sections. *Physical Review*, 114:1332–1337, Jun 1959.

[57] Kalidas Yeturu. Chapter 3 - machine learning algorithms, applications, and practices in data science. In Arni S.R. S. Rao and C.R. Rao, editors, *Principles and Methods for Data Science*, volume 43 of *Handbook of Statistics*, pages 81–206. Elsevier, 2020.

[58] D.I. Sober, H. Crannell, A. Longhi, S.K. Matthews, J.T. O'Brien, B.L. Berman, W.J. Briscoe, P. L. Cole, J.P. Connelly, W.R. Dodge, L.Y. Murphy, S.A. Philips, M.K. Dugger, D. Lawrence, B.G. Ritchie, E.S. Smith, James M. Lambert, E. Anciant, G. Audit, T. Auger, C. Marchand, M. Klusman, J. Napolitano, M.A. Khandaker, C.W. Salgado, and A.J. Sarty. The bremsstrahlung tagged photon beam in hall b at jlab. *Nuclear Instruments and Methods in Physics Research Section A: Accelerators, Spectrometers, Detectors and Associated Equipment*, 440(2):263–284, 2000.

[59] V.V. Zerkin and B. Pritychenko. The experimental nuclear reaction data (exfor): Extended computer database and web retrieval system. *Nuclear Instruments and Methods in Physics Research Section A: Accelerators, Spectrometers, Detectors and Associated Equipment*, 888:31–43, 2018.

[60] Samuel S. D. and Barry L. B. Atlas of photoneutron cross sections obtained with monoenergetic photons. *Atomic Data and Nuclear Data Tables*, 38(2):199–338, 1988.

[61] E. G. Fuller and H. Gerstenberg. Photonuclear data—abstracts sheets 1955–1982. *National Bureau of Standards*, I-XV, 1975.

[62] *Technetium-99m Radiopharmaceuticals: Status and Trends.* Number 1 in Radioisotopes and Radiopharmaceuticals Series. International Atomic Energy Agency, Vienna, 2010.

[63] *Cyclotron Based Production of Technetium-99m.* Number 2 in Radioisotopes and Radiopharmaceuticals Reports. International Atomic Energy Agency, Vienna, 2017.

[64] *Production Technologies for Molybdenum-99 and Technetium-99m.* Number 1065 in TECDOC Series. International Atomic Energy Agency, Vienna, 1999.

[65] J. L. Vučina. Elution efficiency of mo 99/tc 99m generators. *Physics, Chemistry and Technology*, 2(3):125–130, 2001.

[66] Didier L. B. Fluorine-18 and medical imaging: Radiopharmaceuticals for positron emission tomography. *Journal of Fluorine Chemistry*, 127(11):1488–1493, 2006. The Centenary of Henri Moissan's Nobel Prize.

[67] J. C. Chaves, M. J. Vargas, and R. S. Sánchez. Measurement of activation products generated in the [18f]fdg production by a 9.6mev cyclotron. *Radiation Physics and Chemistry*, 126:32–36, 2016.

[68] Luca R., Mark R. G., Max B., and Sergei L. D. γ-photons and high-energy electrons produced by neutron irradiation in nuclear materials. *Journal of Nuclear Materials*, 585:154584, 2023.

[69] L. Reali, M. R. Gilbert, M. Boleininger, and S. L. Dudarev. Intense γ-photon and high-energy electron production by neutron irradiation: Effects of nuclear excitations on reactor materials. *PRX Energy*, 2:023008, Jun 2023.

[70] R. Gandhi, B. K. Nayak, S. V. Suryanarayana, A. Pal, G. Mohanto, S. De, A. Parihari, A. Kundu, P. C. Rout, S. Santra, K. Mahata, B. Srinivasan, E. T. Mirgule, and J. Pandey. Determination of ^{53}Mn(n, xp) cross sections using the surrogate reaction ratio method. *Physical Review C*, 100:054613, Nov 2019.

[71] R. Gandhi, S. Santra, P. C. Rout, A. Pal, A. Baishya, T. Santhosh, D. Chattopadhyay, K. Ramachandran, G. Mohanto, J. Pandey, A. Diaz-Torres, and R. Palit. Measurement of ^{58}co(n,xp) cross sections by a surrogate method. *The European Physical Journal A*, 59:187, Aug 2023.

[72] R. Gandhi, S. Santra, A. Pal, B. K. Nayak, P. C. Rout, D. Chattopadhyay, A. Kundu, A. Baishya, T. Santhosh, S. K. Pandit, G. Mohanto, and A. Diaz-Torres. Determination of ^{57}Co(n, xp) cross sections using the surrogate reaction ratio method. *Physical Review C*, 106:034609, Sep 2022.

[73] B. Pandey, V. V. Desai, S. V. Suryanarayana, B. K. Nayak, A. Saxena, E. T. Mirgule, S. Santra, K. Mahata, R. Makawana, M. Abhangi, T. K. Basu, C. V. S. Rao, S. Jakhar, S. Vala, B. Sarkar, H. M. Agrawal, G. Kaur, P. M. Prajapati, A. Pal, D. Sarkar, and A. Kundu. Measurement of ^{55}Fe(n, p) cross sections by the surrogate-reaction method for fusion technology applications. *Physical Review C*, 93:021602, Feb 2016.

[74] J. Pandey, B. Pandey, A. Pal, S. V. Suryanarayana, S. Santra, B. K. Nayak, E. T. Mirgule, Alok Saxena, D. Chattopadhyay, A. Kundu, V. V. Desai, A. Parihari, G. Mohanto, D. Sarkar, P. C. Rout, B. Srinivasan, K. Mahata, B. J. Roy, S. De, and H. M. Agrawal. Determination of ^{59}Ni(n, xp) reaction cross sections using surrogate reactions. *Physical Review C*, 99:014611, Jan 2019.

Chapter 2

Theoretical Formalism

2.1 Photonuclear reactions - Theory of direct measurement

A photon can interact with matter in several distinct ways, with the nature of the interaction largely determined by the energy of the incident photon. The primary interaction mechanisms of gamma rays with matter include elastic scattering, inelastic scattering, and absorption. These processes vary depending on the target involved and the energy transfer between the photon and the interacting material. Elastic scattering occurs when a photon interacts with either a bound or free electron, or with a nucleus, without a change in the energy of the incident photon. In this process, the photon simply changes direction while maintaining its energy, except small energy loss on account of target recoil. In contrast, inelastic scattering involves the transfer of energy from the incident photon to an orbital electron. When a gamma radiation with energy E_γ interacts with an electron, the photon loses some of its energy to the electron. If the energy transfer is sufficient to overcome the binding energy of the electron, it may result in the electron being ejected from the atom. This process leads to the production of a secondary electron and a photon with reduced energy. Photon absorption refers to the process by which a material absorbs incoming photons, leading to various physical reactions depending on the energy of photon. This absorption can be categorized into different processes, one of which is the photonuclear reaction. In a photonuclear reaction, the material absorbs a photon and then emits various particles or radiation after reaching equilibrium. A significant phenomenon observed in photonuclear absorption is NRF, which is prominent below the threshold required to produce particles. In this case, the nucleus absorbs the photon and then emits gamma radiation. The following sections of this chapter will further explore NRF and photonuclear reactions in detail.

2.1.1 Nuclear Resonance Fluorescence (NRF)

NRF can be referred to as the process of the resonant absorption of gamma radiation by the atomic nucleus and the corresponding re-emission of the gamma radiation[1]. The process is represented as (γ, γ'), which is known to occur generally below particle separation energies. Using the NRF technique, isotopes can be uniquely identified by measuring the energies of the de-excitation gamma rays. Furthermore, if the NRF transition strength and sample geometry are known, the concentration of the isotope within the sample can also be determined. The transition energies typically range from a few keV to several MeV. Several quantities are involved in the NRF process, including the angular distribution, wavelength, and intensity of the resonance fluorescence, as well as the time delay for re-emission. During the NRF process, the induced radioactivity resulting from resonance absorption can lead to decay into various possible final states. The de-excitation process is governed by the decay branching ratios into the accessible final states. Fig. 2.1 shows a typical representation of the nuclear resonance excitation. Here E and J are the energy and nuclear spin of resonant excited state, E_0 and J_0 are the same for ground state, E_i and J_i are the same for any intermediate state. When an incident gamma ray with energy E_γ is absorbed by a nucleus and de-excited by emitting a gamma ray of energy $E_{\gamma\prime}$, NRF cross section can be determined using the Breit-Wigner formula.

$$\sigma_{NRF} = \frac{1}{4\pi} \frac{2J+1}{2J_0+1} \left(\frac{hc}{E_\gamma}\right)^2 \frac{\Gamma\Gamma_0}{(E_\gamma - E_{\gamma\prime})^2 + \Gamma^2/4} \tag{2.1}$$

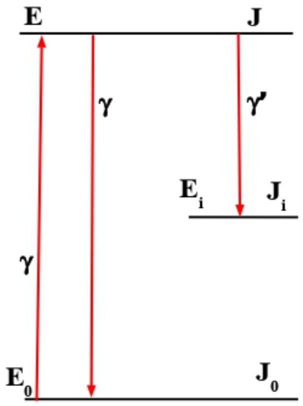

Figure 2.1: Schematic representation of nuclear resonance excitation and de-excitation

where Γ is the total sum of widths corresponding to all possible decay and Γ_0 is the partial width from the excited state to ground state.

One of the most important applications of NRF is Non-Destructive Analysis (NDA) materials. Also this method is very useful in production and structural analysis of isotopes in the isomeric state. The identification of specific isotopes can be achieved by measuring the characteristic energy lines from their NRF states. Further, this technique can be utilized for the production of nuclei in these isomeric states, provided the intermediate level having a sufficient lifetime.

2.1.2 Photonuclear reactions

In a photonuclear reaction, the incoming photon is absorbed by the atomic nucleus and subsequently emits gammas, neutrons, or charged particles, depending on the energy of the incoming photon and state of the nucleus at which it populated[2]. The emission of photo-neutrons, photo-protons, or even multiparticle emission will takes place with its threshold energy. This threshold energy varies for different isotopes. These reactions are analogous to compound nuclear reactions and typically proceed in two distinct stages. After absorbing the incoming photon with specific energy by the target nucleus, it will get excited into its intermediate energy state. By achieving a statistical equilibrium, it may further de-excite by emitting particles or gamma rays. Accordingly, the reaction can be represented as

$$\gamma + A \longrightarrow A^* \longrightarrow B + e \tag{2.2}$$

where A is the target nucleus, A* is the compound nucleus, B is the residual nucleus and e is the ejectile.

The sum of all the cross section possible in a photonuclear reaction is known as the photoabsorption cross section, represented as,

$$\sigma(\gamma, abs) = \sigma_{tot}(\gamma, xn) + \sigma(\gamma, p) + \sigma(\gamma, d) + \sigma(\gamma, \alpha) + ... + \sigma(\gamma, 2p) + \sigma(\gamma, p\alpha) + ... \tag{2.3}$$

where $\sigma_{tot}(\gamma, xn)$ is the total photoneutron cross section, which represents the sum of the cross sections for all photoneutron emission channels. This can be expressed as,

$$\sigma_{tot}(\gamma, xn) = \sum_{\nu} \sigma(\gamma, \nu n) + \sigma(\gamma, np) + \sigma(\gamma, n2p) + \sigma(\gamma, n\alpha) + ... + \sigma(\gamma, f) \tag{2.4}$$

where

$$\sum_{\nu} \sigma(\gamma, \nu n) = \sigma(\gamma, n) + \sigma(\gamma, 2n) + \sigma(\gamma, 3n) + ... \tag{2.5}$$

$\sigma(\gamma, \nu n)$ is the partial photoneutron cross sections. In heavy nuclei, $\sigma(\gamma, \mathrm{abs}) \approx \sigma_{\mathrm{tot}}(\gamma, n)$ can be approximated, as the Coulomb force is strong and the total charged particle cross section is negligibly small. However, in light nuclei, the charged-particle cross section must also be taken into account.

In photonuclear reactions, the cross section typically exhibits a broad peak called the Giant Resonance (GR), a characteristic feature of these processes. The most notable type of Giant Resonance is the GDR, which is particularly prominent in the energy range up to 30 MeV. Above 30 MeV, the Quasi-Deuteron (QD) effect can be observed, which results from the absorption of electric dipole radiation by a neutron-proton pair inside the nucleus, rather than by the nucleus as a whole. In terms of GDR and QD cross section, photo-absorption cross section can be written as,

$$\sigma(\gamma, abs) = \sigma_{GDR}(E_\gamma) + \sigma_{QD}(E_\gamma) \tag{2.6}$$

where $\sigma_{GDR}(E_\gamma)$ is the absorption cross section corresponding to GDR mechanism and $\sigma_{QD}(E_\gamma)$ is the absorption cross section corresponding to quasi deutron (QD) mechanism. Upto 30 MeV we can approximate $\sigma_{tot}(E_\gamma) \approx \sigma_{GDR}(E_\gamma)$. A detailed description of giant resonance and its properties will be provided in the following sections.

2.1.3 Giant Resonances

Giant resonances refer to the collective oscillations of nucleons (protons and neutrons) within the nucleus, arising from the collective behavior of the many-body quantum system. These resonances are a consequence of the nuclear many-body dynamics, where the nucleons move coherently in response to external perturbations, such as photon absorption. The giant resonance can be understood as a transition between the excited states of the nucleus and its ground state, and is typically quantified in terms of transition amplitudes. In a physical sense, the giant resonance can be visualized as a damped, high-frequency vibration of the nuclear density or shape, where the entire nucleus oscillates around its equilibrium configuration. Although these oscillations are generally small in magnitude, they represent a significant collective motion of the nucleons within the nucleus. The existence of collective oscillations was first predicted by A. B. Migdal in 1945[3]. The resonance energy E_R, the width Γ_R, and the strength S_R are the measurable entities describing the giant resonance. Giant resonance depends on the bulk structure of the nucleus rather than the microscopic structure due to its collective behavior. The properties of giant resonance are

1. GR occures in all nuclei except very light nuclei
2. GR parameter shows a smooth function with the mass number A
3. GR obeys the associated sum rule

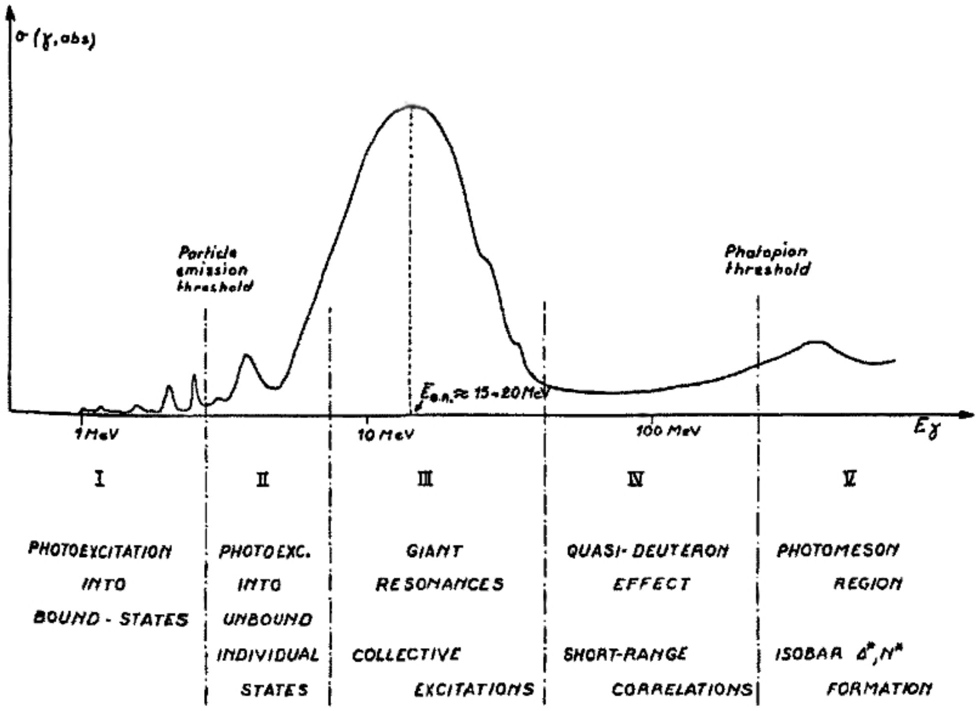

Figure 2.2: Different regions in the photo-absorption cross section.
Note: Figure has been taken fron Lecture notes in Physics, Photonuclear reactions I[4].

The different phenomena in the photo-absorption cross section with respect to the incident photon energy are marked as various regions in Fig 2.2. Region-I, up to a few MeV, shows photo excitations into bound states, and region-II, which is below 10 MeV, shows photo excitations into unbound states. Pygmy resonances, which are low-lying dipole states with strength smaller than the GDR, usually occur in these regions. Above this, a collective excitation is observed in region-III, approximately up to 30 MeV. This region is commonly known as the GR region. Region-IV, which spans in the energy range 40-140 MeV, is the quasi-deuteron region, in which a proton-neutron pair absorbs the incoming photon. The final region marked in the figure is the photo-meson region.

2.1.4 Giant Dipole Resonace (GDR)

The GDR usually occurs in the energy region 13-30 MeV, which is marked as region III in Fig. 2.2. GDR oscillations correspond to the absorption of electric dipole E_1 photons by the atomic nucleus. The phenomena were first observed in two different experiments by

Baldwin and Klaiber[5] in 1947 and 1948. The theoretical interpretations for the observed wide peaks were then put forward by Goldhaber and Teller in 1948. They have made three assumptions while deriving the expressions for resonance energy E_m,

1. The vibration of each proton and each neutron is considered similar to the vibration of ions inside a crystal
2. Oscillations of protons against neutrons are considered similar to compressible liquids, constrained by a fixed surface of the nucleus
3. Oscillations similar to an incompressible hard sphere

Goldhaber and Teller considered the third assumption, which provides an $A^{-1/6}$ dependence for the resonance energy, and the model was then named the Goldhaber-Teller model[6]. Later, Stainwedel and Jensen[7], in 1950, and Danos[8], in 1958, developed the expression of resonance energy by utilizing the second assumption of oscillations of the nucleons. The GDR cross section can be written in terms of Lorentzian form as,

$$\sigma_{GDR}(E_\gamma) = \sum_i \sigma_i \frac{E_\gamma \Gamma_\gamma}{(E_\gamma^2 - E_i^2)^2 + (E_\gamma \Gamma_\gamma)^2} \tag{2.7}$$

where σ_i, E_γ, and Γ_γ are the cross section corresponding to the GDR peak, energy at which GDR occurs, and the width of the GDR peak, respectively.

2.2 Photonuclear reactions - Theory of indirect measurement

Nuclear reactions are typically performed directly, which indcates that a particular projectile and a target will be used for specific nuclear experiments under study. However, many relevant interactions involve unstable targets that are too short-lived to serve as effective targets and are challenging to produce with the current experimental setup. Additionally, obtaining projectiles with the required energy and current is difficult in certain situations. Such situations are handled by introducing some indirect methods, that utilizes alternate projectile-target combination. Among different methods, surrogate reaction methods are

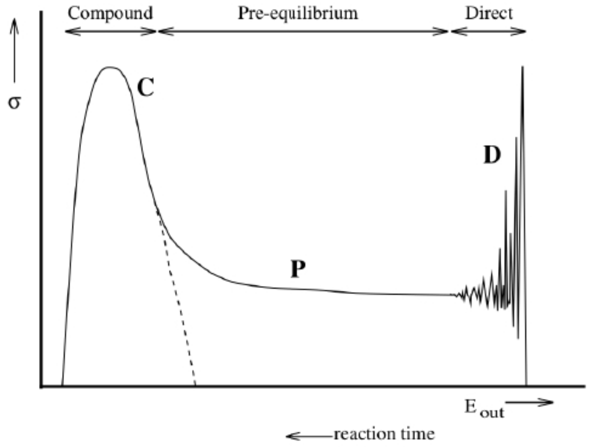

Figure 2.3: Outgoing particle spectra corresponding to different reaction mechanism(Schematic picture).
Note: Figure has been taken fron TALYS manual[10].

the most suitable indirect method to study a specific cross section[9]. The surrogate reaction methods are based on Bohr's hypothesis of the compound nucleus. In the following sections, we will explore the theoretical background of surrogate measurement techniques.

2.2.1 Theory of compound nuclear reaction

A typical particle spectra in a nuclear reaction mechanisms is depicted in Fig.2.3. This classification is based on the time scale at which the reaction occurs. Direct nuclear reactions typically occur at the nuclear surface, where the incident energy of the projectile is sufficiently high that it interacts primarily with the surface rather than the entire nucleus. These reactions are characterized by a shorter time (time scale $\approx 10^{-22}$ sec) scale and a diffraction-like pattern can be observed in the spectra of the outgoing particles. In contrast, compound nuclear reactions take place over a longer time scale due to the equilibration of the incident energy within the target nucleus, resulting in outgoing particle spectra that generally exhibit a Maxwellian distribution. The nuclear reaction mechanism at intermediate time scales is referred to as the pre-equilibrium process. In this mechanism, particle emission occurs before the system reaches statistical equilibrium.

Niels Bohr in 1936[11] described the nuclear reaction mechanism via the formation of a compound nucleus and the corresponding decay. According to Bohr, the projectile and target combine to form an excited state, where the projectile energy gets distributed among the target nucleus. Due to the short mean free path and energy sharing, the projectile particle cannot re-emit from the target. Hence, the compound nuclear reaction is a two-stage process proceeding in a slow time scale. If A is the target nucleus, a is the projectile, B^* is the intermediate state formed, C is the residual nucleus, and c is the ejectile, then the two-stage process can be expressed as

$$A + a \longrightarrow B^* \longrightarrow C + c \tag{2.8}$$

According to Bohr, the second stage in this nuclear reaction is independent of the first stage, known as the independence hypothesis. Thus, the mode of formation does not influence the emission of particles from the Compound Nucleus (CN). The decay of the compound nucleus will depend on the type of the compound nucleus formed and the state. The cross section for the entire compound nuclear reaction can be represented as,

$$\sigma_{ac} = \sigma_a \frac{\Gamma_c}{\Gamma} \tag{2.9}$$

where σ_a is the compound nucleus formation cross section corresponding to the projectile a, Γ_c is the probability of the compound nucleus decaying to the exit channel c, and Γ is the total width, which is equal to the summation of all the partial widths Γ_c.

2.2.2 Hauser-Feshbach theory

The Hauser-Feshbach theory[12] was developed to describe the theoretical framework of compound nuclear reactions. In this theory, the cross section for a particular compound nuclear reaction, as shown in Eq. 2.8, can be written as the product of two terms - compound nuclear formation cross section ($\sigma_a^{CN}(E_x, J, \pi)$) corresponding to particular excitation energy, spin, and angular momentum state, and the associated decay probability

$(\Gamma_c^{CN}(E_x, J, \pi))$.

$$\sigma_{a,c}(E_a) = \sum_{J,\pi} \sigma_a^{CN}(E_x, J, \pi)\Gamma_c^{CN}(E_x, J, \pi) \tag{2.10}$$

The compound nuclear reaction cross section at a particular orbital angular momentum state l can be written as,

$$\sigma_a = \pi \lambdabar_a^2 (2l + 1) T_a \tag{2.11}$$

Here, $\lambdabar$ represents the reduced wavelength corresponding to the incident channel, and T_a is the incident channel transmission coefficient, which is given by $1- |< S_{aa} >|^2$, where S_{aa} is the average S-matrix. Using the transmission coefficients, decay probability can be written as

$$\Gamma_c^{CN}(E_x, J, \pi) = \frac{T_c(E_x, J, \pi)}{\sum_f T_f(E_x, J, \pi)} \tag{2.12}$$

where, T_c represents the transmission coefficient corresponding to the particular decay channel c, and T_f represents the transmission coefficient corresponding to all the exit channels. Thus, the total cross section can be written as

$$\sigma_{a,c}(E_a) = \pi \lambdabar_a^2 (2l + 1) \frac{T_a(E_x, J, \pi) T_c(E_x, J, \pi)}{\sum_f T_f(E_x, J, \pi)} \tag{2.13}$$

By including the spin terms in the total cross section, Eq. 2.13 becomes,

$$\sigma_{a,c}(E_a) = \pi \lambdabar_a^2 \sum_{J,\pi} \frac{(2J + 1)}{(2S + 1)(2l + 1)} \frac{T_a(E_x, J, \pi) T_c(E_x, J, \pi)}{\sum_f T_f(E_x, J, \pi)} \tag{2.14}$$

where J,π is the spin and parity of the compound nucleus, S is the spin of incident particle.

2.2.3 Theory of surrogate reactions

The basic principle behind the surrogate technique is the Bohr hypothesis of compound nuclei. This two-step process helps in determining the cross section of a required compound nuclear reaction by producing the same compound nucleus through an alternate reaction channel. The concept of the surrogate method was first introduced by Cramer and Brit[13] in 1970 to determine the neutron induced fission cross section of various isotopes of thorium, uranium, and plutonium via (t,pf) reactions. Later on, a series of experiments were performed by various groups to determine the (n,f) cross sections[14–23]. Other nuclear reactions, such as neutron capture and reactions involving charged particles in the entrance or exit channels, are also studied using the surrogate technique.

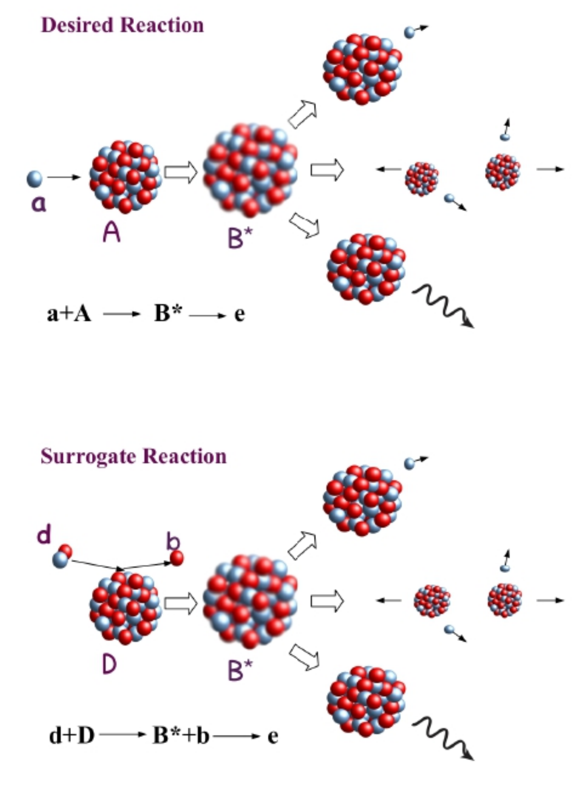

Figure 2.4: Schematic representation for the desired compound nuclear reaction and the corresponding surrogate pair.

The independence in the formation and decay of the compound nucleus is exploited in the surrogate techniques. The detailed theory of compound nuclear reaction has already been explained in the previous section. As the formation channel of the compound nucleus does not influence the decay, the required compound nucleus can be populated in an alternate channel in the surrogate method. The experimental decay probability corresponding to the compound nucleus can thus obtained using the feasible nuclear reaction channel. The pictorial representation of both desired and surrogate reactions is shown in Fig. 2.4. If the projectile target combination in the desired reaction is experimentally not feasible, then the alternate direct reaction channel d+D$\longrightarrow$ B*+b can be used to study the decay probability of the same compound nucleus B*. This alternate reaction channel is known as the surrogate channel. The decay probability of the compound nucleus B* into the desired exit channel c+C can be determined in coincidence with the decay particle c and the outgoing direct emitting particle b. The decay probability can be multiplied by the compound formation cross section corresponding to the entrance channel a+A to obtain the actual cross section of the desired reaction represented in Eq. 2.8. The cross section for the desired reaction can be written as

$$\sigma_{\alpha\beta}(E_a) = \sum_{J,\pi} \sigma_{\alpha}^{CN}(E_x, J, \pi) G_{\beta}^{CN}(E_x, J, \pi) \tag{2.15}$$

where, $\sigma_{\alpha}^{CN}(E_x, J, \pi) = \sigma(a + A \rightarrow B*)$ is the compound nucleus formation cross section, E$_x$ is the excitation energy, Jπ is the corresponding angular momentum and parity, and G$_{\beta}^{CN}$(E$_x$,J,π) is the branching ratio corresponding to the decay of the compound nucleus. Here, α refers to the entrance channel a+A, and β refers to the exit channel c+C. From the surrogate reaction, the kinetic energy of an incident particle in the desired reaction can be calculated using the relation,

$$E_a = \frac{\mathbf{M}_A + \mathbf{M}_a}{\mathbf{M}_A}(E_x - S_a) \tag{2.16}$$

where **M** stands for the mass term and S$_a$ corresponds to the separation energy of the particle a from the compound nucleus.

2.2.4 Surrogate Ratio Method (SRM)

The cross section of a particular nuclear reaction can be determined by utilizing different surrogate approaches viz. Ideal approach, Modeling approach, Approximations, and serendipitous approaches. Among these, the present work utilizes approximations based on the Weisskopf-Ewing (WE) limit[24], incorporating it into the Hauser-Feshbach theory, where the branching ratios are assumed to be independent of spin and parity. Thus, the branching ratios can be experimentally determined from the coincidence probabilities corresponding to the decay particle and the projectile-like particle emitted in the surrogate reaction. Applying WE approximations, Eq. 2.15 becomes,

$$\sigma_{\alpha\beta}(E_a) = \sigma_{\alpha}^{CN}(E_x) G_{\beta}^{CN}(E_x) \tag{2.17}$$

where $\sigma_{\alpha}^{CN}(E_x) = \sum_{J,\pi} \sigma_{\alpha}^{CN}(E_x, J, \pi)$ is the compound nuclear formation cross section, which can be obtained theoretically by applying suitable nuclear reaction code.

In the surrogate ratio method, two different compound nuclei, one corresponding to the desired compound nuclear reaction and the other corresponding to the reference compound nuclear reaction, are populated through different surrogate experiments (transfer reactions).

$$A_1 + a_1 \longrightarrow B_1^* \longrightarrow C_1 + c_1 \tag{2.18}$$

$$A_2 + a_2 \longrightarrow B_2^* \longrightarrow C_2 + c_2 \tag{2.19}$$

Here, Eq. 2.18 represent the desired and Eq. 2.19 represent the reference reactions. The reference reaction should be selected in such a way that the compound nuclear reaction cross section data must be available, or the independent measurement should be possible. Then, the ratio ($R(E_a)$) of the two reactions is determined by applying the Weisskopf-Ewing limit as,

$$R(E_a) \quad = \quad \frac{\sigma_{\alpha_1\beta_1}}{\sigma_{\alpha_2\beta_2}} \quad = \quad \frac{\sigma_{\alpha_1\prime}^{CN}(E_x) \;\; G_{bY_1}^{CN}(E_x)}{\sigma_{\alpha_2\prime}^{CN}(E_x) \;\; G_{bY_2}^{CN}(E_x)} \tag{2.20}$$

In the surrogate experiment, the decay probability can be determined using the coincidence measurement utilizing the expression,

$$\Gamma^{exp}_{\alpha\prime\beta}(E_x) = G^{CN}_{\beta}(E_x) = \frac{N_{\alpha\prime\beta}}{N_{\alpha\prime}\epsilon_{\beta}} \tag{2.21}$$

where α' is the entrance channel corresponding to the surrogate reaction (d+D), $N_{\alpha'\beta}$ is the number of coincidence events between the direct emitting particle b and the decay particle c, $N_{\alpha'}$ is the total number of required surrogate events, and ϵ_β is the efficiency of the detector that used to detect the decay particle c from the compound nucleus, populated through the surrogate reaction.

The Surrogate Ratio Method (SRM) can be utilized to determine the photon induced nuclear reaction cross section only after achieving any of the following three conditions: (i)both of the γ induced reactions and corresponding surrogate reactions (here transfer reaction) populate the compound nuclei with the same (or similar) J^π distributions, (ii) It should satisfy the weak Weaskopf-Ewing condition, that is, the branching ratio of the compound nuclei populated does not depend on its spin and parity, or (iii)the ratio of branching ratios for the observable from the CN populated in surrogate reactions is not sensitive to the difference in J^π distributions populated in γ induced reactions and corresponding surrogate reactions. The first condition can be achieved by selecting surrogate reactions with targets having similar level structures and reaction mechanisms. The other two conditions can be checked through suitable statistical nuclear reaction models.

These reaction model analyses are specifically implemented in a computer program known as a nuclear reaction code. One such code, TALYS 1.96, deals with reactions at low and medium energies, and will be discussed in the upcoming section.

2.3 TALYS - A statistical nuclear reaction code

Building upon the theoretical concepts discussed in the previous sections, this section outlines the statistical theoretical code used in this work, namely TALYS 1.96[10], a nuclear reaction code developed by Arjan Koning to provide an accurate and complete simulation of various nuclear reactions, particularly those below 200 MeV. Utilizing TALYS, one can analyze basic nuclear reaction experiments and generate nuclear data for various applications. The code TALYS can simulate nuclear reactions that include projectiles such as neutrons, protons, gammas, deuterons, alphas, ^{3}He, and tritons with energies ranging from eV to 200 MeV. The compound nuclear reactions are governed by Hauser-Feshbach formalism, and width fluctuation correction is applied in TALYS. Different optical potential models, pre-equilibrium models, γ-ray strength functions, level densities, and fission models are also included in TALYS. The parameters required for calculations, such as GRD parameters, level density parameters, nuclear masses, γ-ray strength functions, etc. are taken from a database of nuclear structure parameters, which is based on the Reference Input Parameter Library (RIPL3)[25]. The code can provide output that includes cross sections, spectral and angular distributions of the emitted particles, etc. In the following section, we will discuss nuclear level density models and γ-ray strength function models available in TALYS in detail.

2.4 Nuclear Level Densities (NLD)

Nuclear level density (NLD) is the fundamental property of the nucleus, which is defined as the number of energy levels occupied per unit energy interval at given excitation energy E$_x$ and particular spin parity state J$^\pi$. Utilizing the correct level density, one can theoretically evaluate the cross sections, angular distributions, particle spectra, and other nuclear reaction entities. The basic expression for total level density ($\rho^{tot}(E_x)$) can be written in terms of excitation energy E$_x$, spin J and parity π as,

$$\rho^{tot}(E_x) = \sum_J \sum_\pi \rho(E_x, J, \pi) \tag{2.22}$$

As the nuclear levels degenerate in magnetic quantum number M, which includes the 2J + 1 states for each level, the total state density $\omega^{tot}(E_x)$ will be,

$$\omega^{tot}(E_x) = \sum_J \sum_\pi (2J+1)\rho(E_x, J, \pi) \tag{2.23}$$

The level density can be further written in as a factorized form with a parity distribution term $P(E_x, J, \pi)$ and spin distribution term $R(E_x, J)$ as,

$$\rho(E_x, J, \pi) = P(E_x, J, \pi)R(E_x, J)\rho^{tot}(E_x) \tag{2.24}$$

By applying the statistical mechanics, the Eq.2.23 can be expressed in terms of entropy S as,

$$\omega^{tot}(E_x) = \frac{\exp[S(E_x)]}{\sqrt{D(E_x)}} \tag{2.25}$$

where the determinant D(E$_x$), is related to the saddle-point approximation. There are two main classifications of nuclear level density models, phenomenological level densities and microscopic level densities. Phenomenological level density models consist of analytical expressions and associated adjustable parameters. The level density models that consider the discrete structure of the single-particle spectra corresponding to the realistic effective potentials are referred to as the microscopic level density models. Different phenomenological and microscopic level density models considered in the present study (which is available in code TALYS) are briefly described below.

2.4.1 Fermi Gas Model (FGM)

The Fermi Gas Model (FGM) assumes equally spaced single-particle states, which build the excited nuclear levels[26]. It also assumes that the collective levels are not present in the system. For a two-Fermion system consisting of distinguishable excited neutrons and protons, the total state density in the Fermi gas model can be written as,

$$\omega_F^{tot}(E_x) = \frac{\sqrt{\pi}}{12}\frac{\exp[2\sqrt{aU}]}{a^{1/4}U^{5/4}} \tag{2.26}$$

Here a is the level density parameter and theoretically, it can be written as $a = \frac{\pi^2}{6}(g_\pi + g_\nu)$, where g_π is the spacing of proton single particle state near Fermi energy and g_ν is the same but for neutron. U is the effective excitation energy, which is equal to E$_x$ $-$ Δ, where Δ

is the energy shift. The Fermi gas level density is given by

$$\rho_F(E_x, J, \pi) = \frac{1}{2\sqrt{2\pi}\sigma}\frac{\sqrt{\pi}}{12}\frac{\exp[2\sqrt{aU}]}{a^{1/4}U^{5/4}}R_F(E_x, J) \tag{2.27}$$

where the 1/2, in the beginning, came from equiparity distribution and σ^2 is the spin cut-off parameter which quantifies the distribution of spin states around a given energy level. $R_F(E_x, J)$ is the Fermi gas spin distribution given by

$$R_F(E_x, J) = \frac{2J+1}{2\sigma^2}\exp\left[-\frac{(J+\frac{1}{2})^2}{2\sigma^2}\right] \tag{2.28}$$

The total Fermi gas state density will be

$$\rho_F^{tot}(E_x) = \frac{\omega_F^{tot}(E_x)}{\sqrt{2\pi}\sigma} \tag{2.29}$$

2.4.2 Constant Temperature Model (CTM)

In the Constant Temperature Model (CTM)[27], the energy regime is divided into two, the low-energy part and the high-energy part. The low energy part is the energy range at which constant temperature law applies and covers an energy range starting from 0 MeV up to the matching energy E$_M$ and above E$_M$ is the high energy part at which the Fermi gas model applies. The level density corresponding to constant temperature part will be

$$\rho_T^{tot}(E_x) = \frac{1}{T}\exp(\frac{E_x - E_0}{T}) \tag{2.30}$$

where T is the nuclear temperature and E$_0$ is the parameter adjustable to the experimental data. Total level density can be written as

$$\begin{aligned}\rho_{CTM}^{tot}(E_x) &= \rho_T^{tot}(E_x), \;\; if E_x \leq E_M \\ &= \rho_F^{tot}(E_x), \;\; if E_x > E_M\end{aligned}$$

The level density equation become

$$\begin{aligned}\rho_{CTM}(E_x, J, \pi) &= \tfrac{1}{2}R_F(E_x, J)\rho_T^{tot}(E_x), \;\; if E_x \leq E_M \\ &= \rho_F(E_x, J, \pi), \;\; if E_x > E_M\end{aligned}$$

In the Fermi gas region, the effective excitation energy U=E$_x$ − Δ^{CTM}, where

$\Delta^{CTM} = \chi\frac{12}{\sqrt{A}}$, where χ is the pairing shift parameter given by

$$\begin{aligned}\chi &= 0, \quad for\ odd-odd \\ &= 1, \quad for\ odd-even \\ &= 2, \quad for\ even-even\end{aligned}$$

2.4.3 Back-shifted Fermi Gas Model (BFM)

In the Back-shifted Fermi Gas Model (BFM)[28], the pairing effects of odd-even nuclei were considered through a pairing energy shift. Hence, the pairing energy Δ is considered as an adjustable parameter. The same expressions correspond to total Fermi level density and Fermi state density, as in the FGM, is used in the entire energy regime for BFM. However, the effective excitation energy U=E$_x - \Delta^{BFM}$ is used in all expressions, with

$$\Delta^{BFM} = \chi\frac{12}{\sqrt{A}} + \delta \tag{2.31}$$

$$\begin{aligned}\chi &= -1, \quad for\ odd-odd \\ &= 0, \quad for\ odd \\ &= 1, \quad for\ even-even\end{aligned}$$

Here δ is an adjustable parameter that is placed according to experimental fitting. Due to the divergence of level density expression when U tends to 0, a modification to this model was provided by Grossjean and Feldmeier[29] and later finalized by Demetriou and Goriely[30] as,

$$\rho^{tot}_{BFM} = \left[\frac{1}{\rho^{tot}_F(E_x)} + \frac{1}{\rho_0(t)}\right]^{-1} \tag{2.32}$$

the term $\rho_0(t)$ is given by,

$$\rho_0 = \frac{\exp(1)}{24\sigma}\frac{(a_n + a_p)^2}{\sqrt{a_n a_p}}\exp(4a_n a_p t^2) \tag{2.33}$$

where $a_n = a_p = a/2$ and $t = \sqrt{\frac{U}{a}}$

2.4.4 Generalized Superfluid Model (GSM)

The Generalized Superfluid Model (GSM)[31] is developed based on the Bardeen–Cooper–Schrieffer theory and the associated superconductive pairing correlations. During the energy change from the low energy regime, where the level density obeys CTM, to high energy, where the level density obeys FGM, a phase transition from the superfluid behavior is expected. At the low energy range, the level density is strongly influenced by pairing correlations. The transition energy does not depend on a discrete energy level, but the total level density in the GSM can be divided into two, one is below a critical energy U_c and one is above U_c. The critical energy U_c can be written in terms of thermodynamic quantities as,

$$U_c = a_c T_c^2 + E_{cond} \tag{2.34}$$

where the critical temperature $T_c = 0.567\Delta_0$ and pairing correlation $\Delta_0 = \frac{12}{\sqrt{A}}$. E_{cond} is the condensation energy, given by

$$E_{cond} = \frac{3}{2\pi^2} a_c \Delta_0^2 \tag{2.35}$$

a_c is the critical level density parameter. The effective excitation energy U' is given by,

$$U' = E_x + \chi\Delta_0 + \delta \tag{2.36}$$

where,

$$\begin{aligned} \chi &= 2, \quad for\ odd - odd \\ &= 1, \quad for\ odd \\ &= 0, \quad for\ even - even \end{aligned}$$

At $U' \geq U_c$, the total level density is given by the Eq. 2.29. At $U' > U_c$, where FGM is applicable, the effective excitation energy $U = E_x - \Delta^{GSM}$, with $\Delta^{GSM} = E_{cond} - \chi\Delta_0 - \delta$.

2.4.5 Skyrme-Hartree-Fock-BCS level density model

Microscopic level densities are devoloped based on the Hartree-Fock model calculations. In the Skyrme-Hartree-Fock-Bardeen-Cooper-Schrieffer (HF-BCS) level density model, level densities up to excitation energy 150 MeV and spin (J)=30 are calculated by S.Goriely[32]. A zero-range Skyrme-type interaction is assumed to govern the interactions between nucleons within the nucleus. Additionally, the nucleons are treated as Cooper pairs in accordance with the Bardeen-Cooper-Schrieffer (BCS) theory of superconductivity. The corresponding pairing interaction generates an energy gap between paired and unpaired nucleons, and the resulting pairing corrections are computed using the statistical partition function approach, with the pairing force given by,

$$\nu_{pair}(r_{ij}) = V_{\pi q}\delta(r_{ij}) \tag{2.37}$$

where $V_{\pi q}$ is the pairing strength parameter, which is different for protons and neutrons inside the nucleus.

2.4.6 Skyrme-Hartree-Fock-Bogoliubov level density model

A modification to HF-BCS, based on the microscopic combinatorial models with modified values of excitation energy, spin and parity is proposed by Hilaire and Goriely[33]. Along with these, partial particle-hole (ph) dependence on nuclear level density is also considered. The method utilizes the axially symmetric Hartree-Fock-Bogoliubov (HFB) model by including the collective enhancement and intrinsic state densities. In the Bogoliubov approach, pairing correlations are considered in a fully self consistent way. During the transition from spherical nuclei to deformed nuclei, a phenomenological approach is considered for representing the damping function. This method calculated level densities for above 8500 nuclei, for excitation energies upto 200 MeV and spin values upto J=49 in table format.

2.4.7 Gogny-Hartree-Fock-Bogoliubov level density model

Gogny force is the finite range effective interaction between nucleons inside the nuclei and D1M referes to the modified version of Gogny force, consisting of experimentally adjusted parameters. The Gogny force offers the advantage of providing an accurate description of low-energy collective properties, particularly when compared to the Skyrme force. The temperature-dependent HFB model, employing the Gogny force [34], facilitates a microscopic description of energy-dependent effects such as shell structure, pairing, and deformation. This model also accounts for the transition from deformed to spherical shapes in nuclei at various temperatures.

2.5 Gamma strength function models

The gamma strength function, or the Photon Strength Function (PSF) is a crucial quantity that describes the gamma transitions in a nuclear reaction. The gamma strength function is the average probability for the gamma transition, which is essential while studying the radiative neutron capture and photo-neutron reactions. Since gammas may be emitted in association with charged particle emissions, gamma strength functions are considered an appropriate model for describing the theory. $f_{Xl}(E_\gamma)$ denote the gamma transition at energy E$_\gamma$, where X stands for either of the transitions, that is, electric (E) or magnetic (M) with multipolarity l. There are various models describing the PSF, including phenomenological and microscopic models. Phenomenological models are developed by considering the Lorentzian form with GDR parameters. The major strength function models used in the present thesis are described in detail below.

2.5.1 Brink-Axel model

In this model of PSF[35, 36], standard Lorentzian form with giant resonance parameters is considered to describe the strength function.

$$f_{Xl}(E_\gamma) = K_{Xl}\frac{\sigma_{Xl}E_\gamma\Gamma_{Xl}^2}{(E_\gamma^2 - E_{Xl}^2)^2 + E_\gamma^2\Gamma_{Xl}^2} \tag{2.38}$$

where σ_{Xl} is the strength of giant resonance, E$_{Xl}$ is the energy of giant resonance, and Γ_{Xl} is the width of the giant resonance, and K$_{Xl} = \frac{1}{(2l+1)\pi^2\hbar^2c^2}$.

2.5.2 Kopecky-Uhl model

TALYS 1.96 utilizes the Kopecky-Uhl model [37, 38] strength function as the default option for E_1 transitions. This model was developed to address the discrepancies observed in the Brink-Axel model below the neutron binding energy. Specifically, as $(E_\gamma) \longrightarrow 0$, the Brink-Axel model fails to accurately describe electric dipole transitions. To resolve this limitation, the Kopecky-Uhl model employs a generalized Lorentzian function, given by

$$f_{E_1}(E_\gamma, T) = K_{E_1}\left[\frac{E_\gamma \tilde{\Gamma}_{E_1}(E_\gamma)}{(E_\gamma^2 - E_{E_1}^2)^2 + E_\gamma^2 \tilde{\Gamma}_{E_1}(E_\gamma)^2} + \frac{0.7\Gamma_{E_1} 4\pi^2 T^2}{E_{E_1}^3}\right]\sigma_{E_1}\Gamma_{E1} \quad (2.39)$$

where $\tilde{\Gamma}_(E_\gamma)$ is the energy dependent damping given by

$$\tilde{\Gamma}(E_\gamma) = \Gamma_{E1}\frac{E_\gamma^2 + 4\pi^2 T^2}{E_{E1}^2} \quad (2.40)$$

and T is the nuclear temperature is given by Kopecky et al[38],

$$T = \sqrt{\frac{E_n + S_n - \Delta - E_\gamma}{a(S_n)}} \quad (2.41)$$

where E$_n$ is the incident neutron energy and S$_n$ is the seperarion energy, a is the level density parameter and Δ is the pairing correction.

2.5.3 Skyrme-Hartree-Fock BCS model

In this model, gamma strength functions are calculated according to the microscopic model of the Skyrme-Hartree-Fock BCS model[39] with quasi-random phase approximation (QRPA). An important feature of this model is its self-consistency, that is, the same Skyrme effective interaction is used in calculating the residual interaction and mean field. Here, HF+BCS approximation is used to calculate the ground state properties. The strength function calculated by Goriely and Khan is given by

$$f_{E1}(E_\gamma) = f^{norm} f_{table}(E_\gamma + E_{shift}) \tag{2.42}$$

where the default value of f^{norm} is 1 and E_{shift} is 0.

2.5.4 Skyrme-Hartree-Fock-Bogoliubov model

In this model[40], the strength function is evaluated using the Skyrme-Hartree-Fock-Bogoliubove model with QRPA. Here, the ground state is calculated using the HFB model, and the Skyrme-type interactions that are defined by different values of the nucleon effective mass and associated prescriptions for the pairing interaction are also considered. In this model, the nucleon-nucleon effective interaction is used to calculate the residual interaction. The damping corresponding to the collective motions is described using some phenomenological models. Here, the strength is calculated using the folded Lorentzian given by,

$$f_L(E_x, E) = \frac{1}{2\pi} \frac{\Gamma(E)}{(E' - E - \Delta(E))^2 + \Gamma(E)^2/4} \tag{2.43}$$

where E$_x$ is the excitation energy correspond to the particle-hole QRPA response, $\Delta(E)$ and $\Gamma(E)$ are real and complex part of the self energy, respectively. The width $\Gamma(E)$ can be obtained from the expression given below.

$$\Gamma(E) = \frac{1}{E} \int_0^E d\epsilon[\gamma_p(\epsilon) + \gamma_h(\epsilon - E)](1 + C_{ST}) \tag{2.44}$$

where γ_p, γ_h are the decay widths of particle and hole states, respectively and C$_{ST}$ is the Skyrme interaction factor.

2.5.5 Hybrid model

The hybrid strength function model is the phenomenological model developed by Goriely[41], utilizing the Lorentzian function with temperature and energy-dependent width. This form results in a different functional form at low energy than the Kopecky-Uhl model. The energy-dependent width is given by

$$\Gamma(E_\gamma) = \sqrt{\frac{1+\frac{2}{3}F'}{1+2F}}\Gamma_{GDR}\frac{E_\gamma^2 + 4\pi^2 T_n^2}{E_\gamma E_{GDR}} \tag{2.45}$$

where T_n is the nuclear temperature and F′ and F are Migdal constants.

2.5.6 Temperature-dependent Skyrme-Hartree-Fock Bogoliubov model

The temperature-dependent Skyrme-Hartree-Fock-Bogoliubov model[40] is the extension of Skyrme-Hartree-Fock-Bogoliubov model with QRPA. In this model a temperature correction to the width expression given by

$$\Gamma' = \Gamma\left[1 + \alpha\frac{4\pi T^2}{EE_{GDR}}\right] \tag{2.46}$$

where T is the temperature of the absorbing state and α is the normalizing constant.

2.5.7 Temperature-dependent Relativistic Mean Field model

In this model[42], correct description of the continuum, deformation effects, spreading width, and temperature effects are included to determine the continuum random phase approximation (CRPA) E_1 strength function using the relativistic mean field approach. The strength is given by

$$S(E) = \int_0^\infty dE_x S_{RPA}(E') f_L(E, E_x) \tag{2.47}$$

where E_x is the excitation energy of the CRPA response. $f_L(E, E_x)$ is the Lorentzian function given by

$$f_L(E, E') = \frac{2}{\pi}\frac{\Gamma(E)E^2}{[E^2 - (E_x - \Delta(E_x)^2)]^2 + \Gamma(E)^2E^2} \tag{2.48}$$

where the time-dependent width $\Gamma(E)$ is given by,

$$\Gamma'(E,T) = \Gamma(E)\frac{1}{E_{GDR}^2}\left[E^2 + \frac{4\alpha\pi^2 T^2 E_{GDR}}{E+\delta}\right] \tag{2.49}$$

Here T is the temperature of the nucleus in the final state and $\delta = 0.1$ is a constant parameter.

2.5.8 Gogny-Hartree-Fock-Bogoliubov model

In the Gogny-Hartree-Fock-Bogoliubov model[43], the D1M Gogny force is used, and an energy shift parameter that varies with energy is empirically included in the expression. The model includes contributions from both the E1 and M1 transitions beyond one-particle and one-hole excitations. The final strengths correspond to E1 and M1 is given by

$$\overleftarrow{f_{E1}}(E_\gamma) = f_{E1}^{QRPA}(E_\gamma) + f_0 E_x/[1 + e^{(E_\gamma - E_0)}] \tag{2.50}$$

$$\overleftarrow{f_{M1}}(E_\gamma) = f_{M1}^{QRPA}(E_\gamma) + Ce^{\eta E_\gamma} \tag{2.51}$$

where f_{X1}^{QRPA} (X stands for E or M) represent the D1M+QRPA dipole strength, E$_x$ (in MeV) is the excitation energy correspond to the initial de-exciting state, $f_0, \eta, C and E_0$ are the free parameters.

2.5.9 Simplified version of Modified Lorentzian (SMLO)

In this model[44], an axial symmetry is considered for nuclei. For deformed nuclei, the effective quadrupole deformation parameter $\beta 2$ is used in the SMLO model. The expression for width is given by

$$\Gamma_j^{SMLO}(E_\gamma) = \frac{\Gamma_{r,j}^{SMLO}}{E_{r,j}^{SMLO}} E_\gamma \tag{2.52}$$

The index j represent the normal mode of giant vibrations

Bibliography

[1] A. Zilges, D.L. Balabanski, J. Isaak, and N. Pietralla. Photonuclear reactions—from basic research to applications. *Progress in Particle and Nuclear Physics*, 122:103903, 2022.

[2] E. Hayward. *Photonuclear reactions*. Number 118. National Bureau of Standards, Washington DC 20234, 1970.

[3] A. Migdal. Quadrupole and dipole γ-radiation of nuclei. *J. Phys. Acad. Sci.*, 8(1-6):331–336, 1944.

[4] S. Costa and C. Schaerf. *Photonuclear Reactions I: International School on Electro- and Photonuclear Reactions, Erice Italy 1976*. Lecture Notes in Physics. Springer Berlin Heidelberg, 1977.

[5] G. C. Baldwin and G. S. Klaiber. Photo-fission in heavy elements. *Physical Review*, 71:3–10, Jan 1947.

[6] M. Goldhaber and E. Teller. On nuclear dipole vibrations. *Physical Review*, 74:1046–1049, Nov 1948.

[7] H. Steinwedel and J. H. D.Jensen. Hydrodynamik von kerndipolschwingungen. *Zeitschrift für Naturforschung A*, 5(8):413–420, 1950.

[8] M. Danos. On the long-range correlation model of the photonuclear effect. *Nuclear Physics*, 5:23–32, 1958.

[9] J. E. Escher, J. T. Harke, F. S. Dietrich, N. D. Scielzo, I. J. Thompson, and W. Younes. Compound-nuclear reaction cross sections from surrogate measurements. *Review of Modern Physics*, 84:353–397, Mar 2012.

[10] Koning, A., Hilaire, S., and Goriely, S. Talys: modeling of nuclear reactions. *Eur. Phys. J. A*, 59(6):131, 2023.

[11] N. Bohr. Neutron capture and nuclear constitution. *Nature*, 137:344–348, 1936.

[12] W. Hauser and H. Feshbach. The inelastic scattering of neutrons. *Physical Review*, 87:366–373, Jul 1952.

[13] J. D. Cramer and H. C. Britt. Fission studies of thorium, uranium, and plutonium isotopes with (t, pf) reactions. *Physical Review C*, 2:2350–2358, Dec 1970.

[14] H. C. Britt and J. B. Wilhelmy. Simulated (n,f) cross sections for exotic actinide nuclei. *Nuclear Science and Engineering*, 72(2):222–229, 1979.

[15] G. Kessedjian, B. Jurado, M. Aiche, G. Barreau, A. Bidaud, S. Czajkowski, D. Dassié, B. Haas, L. Mathieu, L. Audouin, N. Capellan, L. Tassan-Got, J.N. Wilson, E. Berthoumieux, F. Gunsing, Ch. Theisen, O. Serot, E. Bauge, I. Ahmad, J.P. Greene, and R.V.F. Janssens. Neutron-induced fission cross sections of short-lived actinides with the surrogate reaction method. *Physics Letters B*, 692(5):297 – 301, 2010.

[16] J. E. Escher and F. S. Dietrich. Determining (n, f) cross sections for actinide nuclei indirectly: Examination of the surrogate ratio method. *Physical Review C*, 74:054601, Nov 2006.

[17] J. Pandey, B. Pandey, A. Pal, S. V. Suryanarayana, S. Santra, B. K. Nayak, E. T. Mirgule, Alok Saxena, D. Chattopadhyay, A. Kundu, V. V. Desai, A. Parihari, G. Mohanto, D. Sarkar, P. C. Rout, B. Srinivasan, K. Mahata, B. J. Roy, S. De, and H. M. Agrawal. Determination of ^{59}Ni(n, xp) reaction cross sections using surrogate reactions. *Physical Review C*, 99:014611, Jan 2019.

[18] B. Pandey, V. V. Desai, S. V. Suryanarayana, B. K. Nayak, A. Saxena, E. T. Mirgule, S. Santra, K. Mahata, R. Makawana, M. Abhangi, T. K. Basu, C. V. S. Rao, S. Jakhar, S. Vala, B. Sarkar, H. M. Agrawal, G. Kaur, P. M. Prajapati, A. Pal, D. Sarkar, and A. Kundu. Measurement of ^{55}Fe(n, p) cross sections by the surrogate-reaction method for fusion technology applications. *Physical Review C*, 93:021602, Feb 2016.

[19] R. Gandhi, B. K. Nayak, S. V. Suryanarayana, A. Pal, G. Mohanto, S. De, A. Parihari, A. Kundu, P. C. Rout, S. Santra, K. Mahata, B. Srinivasan, E. T. Mirgule, and J. Pandey. Determination of ^{53}Mn(n, xp) cross sections using the surrogate reaction ratio method. *Physical Review C*, 100:054613, Nov 2019.

[20] R. Gandhi, S. Santra, P. C. Rout, A. Pal, A. Baishya, T. Santhosh, D. Chattopadhyay, K. Ramachandran, G. Mohanto, J. Pandey, A. Diaz-Torres, and R. Palit. Measurement of

^{58}co(n,xp) cross sections by a surrogate method. *The European Physical Journal A*, 59:187, Aug 2023.

[21] R. Gandhi, S. Santra, A. Pal, B. K. Nayak, P. C. Rout, D. Chattopadhyay, A. Kundu, A. Baishya, T. Santhosh, S. K. Pandit, G. Mohanto, and A. Diaz-Torres. Determination of ^{57}Co(n, xp) cross sections using the surrogate reaction ratio method. *Physical Review C*, 106:034609, Sep 2022.

[22] A. Pal, S. Santra, B. K. Nayak, K. Mahata, V. V. Desai, D. Chattopadhyay, and R. Tripathi. Determination of ^{238}Pu(n, f) and ^{236}Np(n, f) cross sections using surrogate reactions. *Physical Review C*, 91:054618, May 2015.

[23] B. K. Nayak, A. Saxena, D. C. Biswas, E. T. Mirgule, B. V. John, S. Santra, R. P. Vind, R. K. Choudhury, and S. Ganesan. Determination of the ^{233}Pa(n, f) reaction cross section from 11.5 to 16.5 mev neutron energy by the hybrid surrogate ratio approach. *Physical Review C*, 78:061602, Dec 2008.

[24] V. F. Weisskopf and D. H. Ewing. On the yield of nuclear reactions with heavy elements. *Physical Review*, 57:472–485, Mar 1940.

[25] R. Capote, M. Herman, P. Obložinský, P.G. Young, S. Goriely, T. Belgya, A.V. Ignatyuk, A.J. Koning, S. Hilaire, V.A. Plujko, M. Avrigeanu, O. Bersillon, M.B. Chadwick, T. Fukahori, Zhigang Ge, Yinlu Han, S. Kailas, J. Kopecky, V.M. Maslov, G. Reffo, M. Sin, E.Sh. Soukhovitskii, and P. Talou. Ripl – reference input parameter library for calculation of nuclear reactions and nuclear data evaluations. *Nuclear Data Sheets*, 110(12):3107 – 3214, 2009. Special Issue on Nuclear Reaction Data.

[26] Alberto M. and Yutaka N. Fermi-gas model parametrization of nuclear level density. *Journal of Nuclear Science and Technology*, 31(2):151–162, 1994.

[27] A. Gilbert and A. G. W. Cameron. A composite nuclear-level density formula with shell corrections. *Canadian Journal of Physics*, 43:1446, January 1965.

[28] W. Dilg, W. Schantl, H. Vonach, and M. Uhl. Level density parameters for the back-shifted fermi gas model in the mass range 40 ¡ a ¡ 250. *Nuclear Physics A*, 217(2):269–298, 1973.

[29] M.K. Grossjean and H. Feldmeier. Level density of a fermi gas with pairing interactions. *Nuclear Physics A*, 444(1):113–132, 1985.

[30] P. Demetriou and S. Goriely. Microscopic nuclear level densities for practical applications. *Nuclear Physics A*, 695(1):95–108, 2001.

[31] A. V. Ignatyuk, K. K. Istekov, and G. N. Smirenkin. Collective effects in level density, and the probability of fission. *Sov. J. Nucl. Phys. (Engl. Transl.); (United States)*, 30:5, 11 1979.

[32] S. Goriely, F. Tondeur, and J.M. Pearson. A hartree–fock nuclear mass table. *Atomic Data and Nuclear Data Tables*, 77(2):311–381, 2001.

[33] S. Goriely, S. Hilaire, and A. J. Koning. Improved microscopic nuclear level densities within the hartree-fock-bogoliubov plus combinatorial method. *Physical Review C*, 78:064307, Dec 2008.

[34] S. Hilaire, M. Girod, S. Goriely, and A. J. Koning. Temperature-dependent combinatorial level densities with the d1m gogny force. *Physical Review C*, 86:064317, Dec 2012.

[35] D.M. Brink. Individual particle and collective aspects of the nuclear photoeffect. *Nuclear Physics*, 4:215–220, 1957.

[36] P. Axel. Electric dipole ground-state transition width strength function and 7-mev photon interactions. *Physical Review*, 126:671–683, Apr 1962.

[37] J. Kopecky and M. Uhl. Test of gamma-ray strength functions in nuclear reaction model calculations. *Physical Review C*, 41:1941–1955, May 1990.

[38] J. Kopecky, M. Uhl, and R. E. Chrien. Radiative strength in the compound nucleus ^{157}Gd. *Physical Review C*, 47:312–322, Jan 1993.

[39] S. Goriely and E. Khan. Large-scale qrpa calculation of e1-strength and its impact on the neutron capture cross section. *Nuclear Physics A*, 706(1):217–232, 2002.

[40] S Goriely, E Khan, and M Samyn. Microscopic hfb + qrpa predictions of dipole strength for astrophysics applications. *Nuclear Physics A*, 739(3):331–352, 2004.

[41] S. Goriely. Radiative neutron captures by neutron-rich nuclei and the r-process nucleosynthesis. *Phys. Lett. B*, 436:10–18, 1998.

[42] I. Daoutidis and S. Goriely. Large-scale continuum random-phase approximation predictions of dipole strength for astrophysical applications. *Physical Review C*, 86:034328, Sep 2012.

[43] S. Goriely, S. Hilaire, S. Péru, and K. Sieja. Gogny-hfb+qrpa dipole strength function and

its application to radiative nucleon capture cross section. *Physical Review C*, 98:014327, Jul 2018.

[44] V. Plujko, O. Gorbachenko, and K. Solodovnyk. Description of nuclear photoexcitation by lorentzian expressions for electric dipole photon strength function. *European Physical Journal A*, 55:014327, Nov 2019.

Chapter 3

Materials and Methods

3.1 Part I - Direct photonuclear measurement

In this thesis, the photonuclear cross sections of various isotopes are investigated through both direct and indirect methods. The direct determination of these cross sections were performed using bremsstrahlung photons generated by a medical Linear Accelerator (LINAC) facility. The corresponding photonuclear reaction yields were quantified employing the activation technique, where samples were irradiated with the specified photon beam for a predefined duration. This approach enabled precise measurement of the reaction yields, facilitating the calculation of the photonuclear cross sections for the selected isotopes. After a specified cooling period, the gamma ray counts in the samples were measured with suitable gamma detectors. Isotopes with shorter half-lives were counted immediately, while those with longer half-lives were counted after specific cooling time. This technique allows for the identification of radioisotopes with specific gamma decay. Due to the spectrum of the source, the integral cross section of the reaction, up to the bremsstrahlung endpoint energy, can be analyzed. In the present study, the integral cross section of the ^{99}Tc$(\gamma, \gamma\prime)^{99m}$Tc and ^{19}F$(\gamma$,n$)^{18}$F reactions were determined using indium as a monitor target. Essential components of the photon activation technique include a medical linear accelerator, which is used to produce photon beams, and a gamma detector, which is employed to detect the associated gamma lines. These components are explained in detail below.

3.1.1 Medical linear accelerator

A linear particle accelerator, or shortly LINAC, belongs to a class of particle accelerators that accelerates subatomic particles or ions to higher energies[1, 2]. In a LINAC, particles are accelerated by passing through a series of linearly arranged electric potentials. The LINAC-producing x-ray photons and energetic electrons find their extensive application in radiation therapy. Such accelerators are generally known as electron LINAC. Electron LINACs are frequently available in S-band (2-4 GHz) frequency. However, for treatments such as tomotherapy and stereotactic radiotherapy, X-band (8-12 GHz) medical LINACs[3] are used.

An electron LINAC comprises an electron source, commonly referred to as an electron gun. The electrons emitted from the electron gun are directed into radio frequency (RF) cavities for further acceleration, typically within the energy range of 4–8 MeV[1–3]. A klystron or magnetron is typically employed as the RF power source, supplying the necessary power to the RF cavities to facilitate the acceleration process. Once accelerated, the electron beam is allowed to incident on a suitable high-Z material, where it generates a bremsstrahlung photon beam. This high-energy photon beam is subsequently utilized for radiation therapy applications. A schematic representation of medical LINAC is shown in Fig. 3.1. The key components of the medical LINAC can be broadly categorized into two groups: internal components and external components. The details of each component of the medical LINAC can be briefly discussed.

Internal components

1. Electron gun and electron modulator - Electron beam source or electron gun is an essential part of the medical LINAC system. Medical LINAC utilize two types of electron guns: diode and triode. Both types share common components, including a heated filament cathode, an anode, and a focusing electrode. The triode electron gun, however, features an additional control grid. In both systems, electrons are emitted from the spherical cathode, which is heated and held at a negative potential

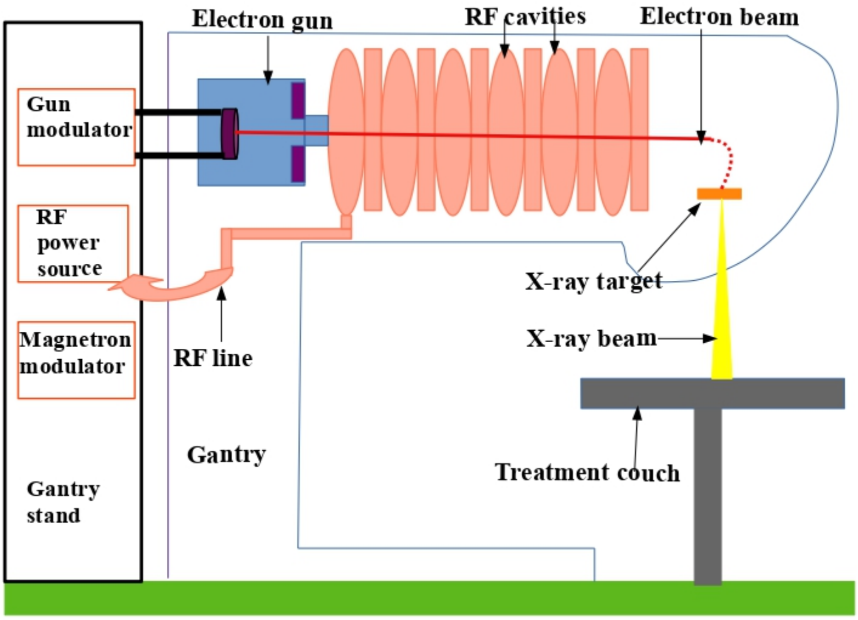

Figure 3.1: The schematic diagram of the medical LINAC.

relative to the grounded anode. These electrons are then accelerated towards the anode, after which they are focused and guided into the RF cavities for further acceleration. Beam size and emittance are the two important factors considered during the injection of the beam into RF cavities. In the present study, we have employed the Varian CLINAC-iX medical LINAC, which consists of a diode-type electron gun.

2. LINAC RF cavities - LINAC RF cavities are a series of segments used for further electron acceleration. RF cavities are built using copper to reduce microwave power loss and powered by an RF power supply. The radio frequency power generator supply an oscillating electric field inside the cavities with a frequency ranges from 1 to 10 GHz. Before entering the cavity, the electrons are made in to bunches with the help of a buncher cavity. The electron beam will gain sufficient energy as it passes through each of the RF cavities.

3. RF power source - Klystron or magnetron are generally used as the RF power source

at LINAC design frequency to produce Microwave (MW) level peak power. The LINACs producing high-energy beams uses Klystrons, where as low-energy LINAC uses magnetrons. The major distinction between klystrons and magnetrons is that the klystron is basically an amplifier with a low-power microwave input, where as the magnetron is a self-oscillator, which produce microwaves by applying a DC input. In klystrons, electron bunches are allowed to propogate inside the klystron vacuum tube, where the cavity of the vacuum tube and the propogation of electron bunch will be in resonance.

4. RF line components:
    (a) Wave guides : A medical LINAC uses accelerating waveguide, which is the hollow metallic structure, through which the particles are accelerated to the required energy. The wave guide size is inversely proportional to the frequency. The RF power supply provide neccessary power to the wave guide, for the electrons to be accelerated. The wave guide is usually made using copper to acheive high electrical conductivity and minimum microwave power loss.
    (b) Waveguide bends : Waveguide bends are used to direct high-frequency signals passing through the waveguide. The radius of the bend should be larger than twice the signal wavelength to minimize signal loss and distortion. Waveguide E-bends are employed to control electric field distortion, while waveguide H-bends are used to manage magnetic field distortion.
    (c) RF transmission window : These windows are the barrier between the vacuum sections of the LINAC and the air filled wave guide.
    (d) RF circulator : Circulators are generally three port or four port component, used for power transmission from RF generator to the air filled wave guide without power loss. The reverse transmission is not possible.
    (e) RF load/terminator : The purpose of an RF load is to terminate the propagating wave in the waveguide by absorbing microwave energy.
5. X-ray target and treatment head - X-ray target is usually a high Z material re-

quired to produce high energy bremsstrahlung radiation using the accelerated electron beam. Usually, tungsten or lead are used as converting targets to obtain a better conversion efficiency. Thick targets are preferred for radiation production, so that all the electrons will stop inside the target. The target is kept inside the treatment head along with a flattening filter, an optical distance indicator, and the beam collimator, etc. The flattening filter, made of aluminum, copper, steel, etc. has a cylindrical symmetry and is used to flatten the beam profile. For the use of an electron beam, two scattering foils, one for generating a broad electron spectrum and the other for producing the mono-energetic beam, are used. Water cooling through copper channels is provided to remove excess heat produced during the X-ray production.

6. Auxiliary systems - The above-mentioned components are kept inside the ultra-high vacuum. Certain components, such as turbomolecular pump (TMP), sputter ion pumb (SIP), gate valves, and pressure gauges, are necessary to maintain a vacuum. A water or air cooling system is necessary to maintain the required temperature in the LINAC cavities

External components

1. Treatment couch - The treatment couch is designed to support the patient during radiation therapy. It can be adjusted in three dimensions to ensure accurate positioning for each treatment.

2. Electronic portal imaging device (EPID) - The EPID, placed at the beam exit, provides real-time monitoring of the radiation passing through the patient, during the radiotherapy treatment. The new generation of EPID systems is based on amorphous silicon. In this system, a scintillator converts radiation into visible light, which is then detected by an array of photodiodes embedded in the amorphous silicon panel. The photodiodes convert the light into charge, which is captured for further processing.

3. Gantry -The entire LINAC is housed within a rotating gantry, which is supported

by a drive stand. The primary purpose of the gantry is to enable the delivery of radiation treatment from multiple angles, ensuring precise targeting of tumors while minimizing exposure to surrounding healthy tissues. The rotation of the gantry allows for optimal positioning of the radiation beam, providing flexibility and accuracy in treatment planning.

4. Gantry stand - The Gantry stand connects the gantry and the treatment room floor. It consists of all the auxiliary systems necessary for the LINAC operation.

3.1.2 Gamma ray detectors

Gamma radiation, high-energy radiation produced either through atomic nuclear interactions or radioactive decay, requires specialized detectors for imaging purposes. Gamma-ray detectors operate on the principle of interaction between gamma rays and the detector material. The most commonly used types of gamma-ray detectors include gas-filled detectors, scintillation detectors, and semiconductor detectors. The choice of a specific gamma-ray detector depends on factors such as the energy of the gamma ray to be detected, as well as the efficiency and resolution of the detector. In the present study, a semiconductor detector, specifically the Cadmium Zinc Telluride (CZT) detector, was employed. This detector is compact and easily portable. Additionally, the CZT detector requires only a laptop for data acquisition. In contrast to HPGe detectors, CZT does not require any associated cooling systems. Therefore, for the present experimental scenario, which involves the activity measurement of a short-lived isotope, the CZT detector represents a highly suitable option. Applying a bias across the detector enables the collection of ionization signals, which correspond to the energy deposited by the electrons.

3.1.3 Cadmium Zinc Telluride (CZT) detector

CZT is a semiconductor gamma ray detector that contains cadmium zinc telluride in the composition $\mathrm{Cd}_{1-x}\mathrm{Zn}_x\mathrm{Te}$ with x around 0.1. The density of the semiconductor is ≈ 5.8 g/cm^3 and effective atomic number (Z_{eff}) is ≈ 50. CZT crystal is grown as a single crystal in a hermetically sealed container at 1100^0 C. Electrical contacts are provided after cutting the crystal into wafers. A speciality of CZT crystal is that its thickness can be varied depending on the application. A larger thickness of around 15 mm is used for high-energy applications and a thinner crystal of thickness of 1 mm is used for low-energy detection. In the present study, a 10 mm ×10 mm×10 mm Kromek GR1 detector with energy resolution <2.5% FWHM at 662 keV and timing resolution less than 100 ns is used. The associated electronic components, such as the preamplifier, shaping amplifier, pulse height digitizer, baseline restorer, and high-voltage supply, are integrated within the compatible detector. The Kromek CZT detector is connected to the acquisition system (laptop) via a USB cable. Signals received from the CZT crystal are processed, digitized, and transmitted to the acquisition system through the USB connection. The MultiSpect software is used for spectrum analysis, visualization and data storage. Major features of the CZT detector are listed below.

- Its semiconducting properties and solid state durability
- High density and effective atomic number
- High stopping power
- Higher absorption coefficients
- Small volume and requirement of low bias voltage
- Can be operated at room temperature
- High counting rate and good energy discrimination

3.1.4 Detector calibration

In gamma ray spectroscopy, a pulse-height spectrum corresponding to the gamma rays emitted from the radioisotope is obtained using a detector. The photopeak position (V_0) and the photopeak width are characteristics of both the detector and the incident energy. Moreover, the position of this peak is proportional to the gamma ray energy, E_γ, and can

Table 3.1: Details of the calibration sources

Source	Activity (μCi) Nov 2001	Half-life (year)	γ energies (keV)	Intensity %
^{133}Ba	3.5	10.551	356	62.05
			80.99	32.9
			302.85	18.34
			383.85	8.94
			276.39	7.16
^{60}Co	3.2	5.27	1332.5	99.98
			1173.23	99.85
^{22}Na	2	2.6	1274.54	99.9
			511	180
^{137}Cs	4	30.08	661.66	85.1

be expressed as straight line equation with slope 'm' and intercept 'c' as:

$$E_\gamma = mV_0 + c \tag{3.1}$$

Therefore, the unknown gamma ray energy of the sample can be determined by fitting the above equation with known gamma ray energies. This process is known as the detector calibration. The standard calibration sources viz. ^{22}Na, ^{137}Cs, ^{60}Co, and ^{133}Ba were used for the energy efficiency calibration of the detector. Further details of these source are tabulated in Table. 3.1. The values of parameters m (slope) and c (intercept) obtained are 0.7501 ± 0.0001 and -1.09 ± 0.16, respectively, and the calibration curve is shown in Fig. 3.2.

The efficiency of the detector for corresponding energies of the gamma lines were determined using the relation

$$\epsilon(E_\gamma) = \frac{C}{A_0 e^{-\lambda t} I_\gamma} \tag{3.2}$$

where C is the count rate, I_γ is the intensity of the gamma transition, A_0 is the activity of the source at the time of standardization, t is the time gap between standardization and calibration, λ is the decay constant of the radioactive source. To determine the efficiency,

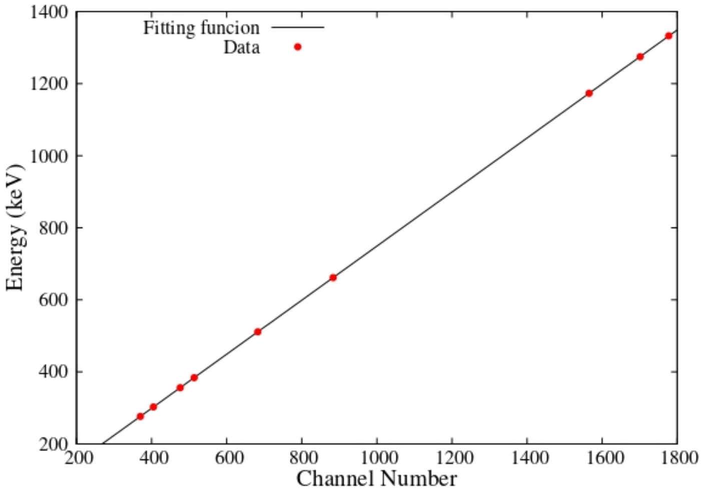

Figure 3.2: Energy calibration of CZT detector

the counts emitted from the sample is recorded for a finite time, using the detector under study.

Table 3.2: The parameters of the fitting function used to model detector efficiency for point source geometry, along with their uncertainties and correlation coefficients, are reported

Parameter	Value	Correlation coefficient		
a	0.74808± 0.099	1		
b	$(3.5\pm0.26)\times10^{-3}$	0.912	1	
c	$(7.02\pm0.16)\times10^{-3}$	0.788	0.971	1

The efficiency data obtained from standard sources are based on point source geometry. We also evaluated the geometry-dependent efficiency for the study of liquid samples. To estimate the efficiency for this specific cylindrical configuration, we employed the Monte Carlo code EFFTRAN[4]. The efficiency data thus obtained is subjected to fitting with the function $f(x) = ae^{-bx} + c$ to determine the detector's efficiency in the desired energy range. The resulting fitting parameters, along with their associated uncertainties, are detailed in Table 3.2 for point source geometry and Table 3.3 for cylindrial source geometry. Furthermore, energy efficiency data for both point source and cylindrical sample geometries, along with their respective uncertainties, are visualized in Fig. 3.3. The detector efficiency for detecting the 140 keV gamma line, corresponding to the ^{99m}Tc isotope, is 0.494±0.042, while the efficiency for detecting the 511 keV gamma line, corresponding to

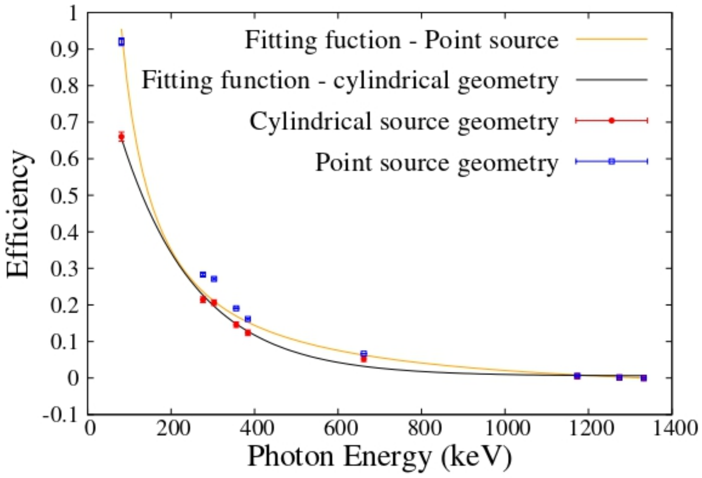

Figure 3.3: Detector efficiency of CZT detector measured for point source and calculated for cylindrical sample geometry using the Monte Carlo code EFFTRAN.

the ^{18}F isotope, is 0.12±0.02.

Table 3.3: The parameters of the fitting function used to model detector efficiency for cylindrical geometry, along with their uncertainties and correlation coefficients, are reported

Parameter	Value	Correlation coefficient		
a	1.0176± 0.0416	1		
b	$(5.525\pm0.023)\times10^{-3}$	0.728	1	
c	$(5.722\pm0.114)\times10^{-3}$	0.085	0.58	1

3.1.5 Target preparation

In photon activation analysis, thick targets are usually used for irradiation. In the present study, ^{99}Tc, ^{19}F, and ^{115}In are the samples to be irradiated. Since ^{99}Tc was a radioactive waste found in radiotherapy centres, the leftover ^{99}Tc isotope from a molybdenum-technetium generator available at hospitals was employed to investigate the production of ^{99m}Tc radiopharmaceuticals. The ^{99}Tc liquid target was placed in a glass bottle with cylindrical geometry, having dimensions of 2 cm× 2 cm. The number of particles in the target was calculated based on the loaded activity of ^{99}Mo used in the generator and the elution efficiency. For the study of ^{18}F production, lithium fluoride (LiF) samples were utilized. The LiF powder was weighed and pressed into pellets using a pelletizer at optimal pressure. Pellets with thicknesses of 245.3 mg/cm^2, 320 mg/cm^2, and 748.9 mg/cm^2 were prepared. Indium was used as a monitor sample in both experiments, with indium foils of thicknesses 388 mg/cm^2, 212 mg/cm^2, and 872 mg/cm^2 included in the setup.

3.1.6 Data analysis

In the present work, we measure the integral cross section associated with the photonuclear reaction induced by bremsstrahlung photons. The expression for the cross section using photon activation can be written as[5],

$$\sigma = \frac{A\lambda e^{\lambda t_2}}{N_0 \phi I K G_\epsilon (1 - e^{-\lambda t_1})(1 - e^{-\lambda t_3})} \tag{3.3}$$

where A is the activity of gamma peak, λ is the decay constant of the residual nucleus, N_0 is the no.of target nuclei per unit area of the irradiated sample, ϕ is the beam flux, G_ϵ is the geometry-dependent efficiency of the detector, I is the branching ratio of the gamma-ray, K is the self-absorption correction factor for gamma-ray in the sample and t_1, t_2, t_3 are the irradiation time, the cooling time and the counting time, respectively.

Since we are using the bremsstrahlung photon beam produced from a corresponding electron beam of sufficient energy, the flux of the incident beam remains an unknown quantity. Thus, we can determine the yield per target nucleus using the relation:

$$\frac{Y}{N_0} = \phi\sigma = \frac{A\lambda e^{\lambda t_2}}{N_0 I K G_\epsilon (1 - e^{-\lambda t_1})(1 - e^{-\lambda t_3})} \tag{3.4}$$

Using Eq. 3.4, the yield ratio R can be expressed as:

$$R = \frac{Y_S}{Y_M} = \frac{A_S N_{0M} I_M K_M G_{\epsilon M}}{A_M N_{0S} I_S K_S G_{\epsilon S}} T \tag{3.5}$$

where Y_S is the yield of sample and Y$_M$ is the yield of monitor reaction. The subscript S refers to the sample and M refers to the monitor. T refers to the time factors, which is given by,

$$T = \frac{\lambda_S e^{\lambda_S t_{2S}}}{\lambda_M e^{\lambda_M t_{2M}}} \frac{(1 - e^{-\lambda_M t_{1M}})(1 - e^{-\lambda_M t_{3M}})}{(1 - e^{-\lambda_S t_{1S}})(1 - e^{-\lambda_S t_{3S}})} \tag{3.6}$$

The yield ratio obtained can then be used to calculate the integral cross-section of the actual reaction using the following relation[6]:

$$\int_{E_{th}}^{E_\gamma} \sigma_S(E)\phi(E)dE = R \int_{E_{th}}^{E_\gamma} \sigma_M(E)\phi(E)dE \tag{3.7}$$

where σ_S and σ_M are the theoretical cross sections of the sample and monitor reactions, respectively. E$_{th}$ and E$_\gamma$ are the threshold and bremsstrahlung end point energies. To calculate the integral cross section $\int_{E_{th}}^{E_\gamma} \sigma_M(E)\phi(E)dE$ for the monitor reaction, the energy-dependent cross section data for the reaction is obtained from the experimental data library, EXFOR. The most suitable theoretical model that predicts the data is then identified, and the corresponding integral cross section is calculated. This integral cross section for the monitor reaction serves as a reference for the final integral cross section measurement of the desired sample.

Table 3.4: The self absorption factor (K) calculated for LiF and Indium

Sample thickness mm	Density g/cm^3	K
LiF		
1.2	2.64	1.013
1.52		1.016
2		1.021
Indium		
1	7.31	1.016
1		1.016
1.82		1.028

Self absorption factor (K)

Self-absorption correction factor (K) for a particular gamman ray is the loss of gamma ray energy in the sample itself due to the sample thickness. The quantity K can be calculated by the Eq. 3.8, proposed by E. Robu and C. Giovani [7].

$$K = \frac{\mu_m \rho x}{1 - exp(-\mu_m \rho x)} \tag{3.8}$$

where μ_m is the mass attenuation coefficient, ρ is the sample density and x is the sample thickness. μ_m and ρ are retrieved from the XMuDat ver. 1.01[8] program. The self absorption factor, calculated for both technetium and indium samples are 1.1803 and 1.0058, respectively. The values of K obtained for different LiF samples are tabulated in Table. 3.4.

3.2 Part II - Indirect photonuclear measurement

Direct cross-section measurements may encounter challenges in certain scenarios, such as unavailability of projectile beams, studying unstable targets, or in energy regimes that are difficult to achieve for specific applications like nuclear astrophysics. To overcome these challenges, indirect experiments that lead to the actual reactions have been developed in recent years. One such approach is the surrogate nuclear reaction method, based on the Bohr hypothesis of the compound nucleus, which is used to determine the cross sections of nuclear reactions involving targets that are difficult to produce. Among various surrogate approaches, the Surrogate Ratio Method (SRM)[9], which utilizes a reference reaction with known experimental data, is used in the present study. An important advantage of the Surrogate Ratio Method is that, by selecting surrogate targets with similar properties, the efficiency factor associated with the detector setup can be eliminated by taking the ratio of the decay probabilities. Here, we utilize the SRM to measure the ^{58}Co(γ,xp) reaction cross section. The radioisotope ^{58}Co is produced in nuclear reactors, as a result of continuous neutron exposure to the reactor's structural materials. Studying the ^{58}Co(γ,xp) reaction is crucial because the energetic gamma rays generated within the reactor can further induce nuclear reactions with ^{58}Co. Since ^{58}Co is an unstable nucleus, direct cross-section measurements are impossible, so we rely on the surrogate approach. To determine the cross section using the SRM technique, a reference reaction is essential to minimize uncertainties associated with the efficiency terms in the cross-section expression. In the present study, the ^{61}Ni(γ,xp) reaction is used as the reference reaction to determine the ^{58}Co(γ,xp) reaction cross section. The compound nuclei ^{58}Co* and ^{61}Ni* are populated through two distinct transfer reactions: ^{56}Fe(^{6}Li,α) and ^{59}Co(^{6}Li,α), respectively. Unlike conventional photonuclear experimental setups, this indirect experiment relies primarily on an accelerator to accelerate charged particles. The working principle of the LINAC, the detectors used in the experiment, and the analysis methodology are thoroughly explained in the following sections.

3.2.1 The Palletron-Linac accelerator facility

The experiment was performed at the BARC-TIFR Pelletron Accelerator Facility, Mumbai, India, utilizing ^{6}Li beam of energy 5-6 MeV/nucleon. A schematic diagram of this accelerator is shown in Fig 3.4.

A negative ion source called MC-SNICS (Multi-Cathode Source of Negative Ions by Cesium Sputtering) is placed at the top of accelerator. High-intensity negative ions with low emittance are delivered from this ion source. The negative ions so-produced are extracted horizontally at an extraction voltage of 150-250 V and then allowed to pass through an injector magnet to reach the vertical accelerator column (VAC) by bending through 90°. The injector magnet analyzes the mass and allows only the mass-selected ions to pass through. During the first stage of acceleration, the negative ion beam will be attracted electrostatically toward the positive high-voltage terminal at the center of the accelerator. To transfer positive charge continuously to the voltage terminal, chain of steel pellets separated by nylon links is used and thus the accelerator is named a Pelletron. The maximum terminal voltage that can be attained is 14 MV. During the first stage of operation, the accelerated singly charged negative ions will gain an energy equivalent to eV$_T$, where V$_T$ is the terminal voltage and charge q=-1e. A carbon stripper foil of thickness $\approx 5\mu$g/cm^2 or a gas stripper is placed inside the terminal for charge exchange collision. The purpose of stripper foil or stripper gas is to remove electrons from the negatively charged ions. Thus, the accelerated negative ions passing through the stripper foil acquire

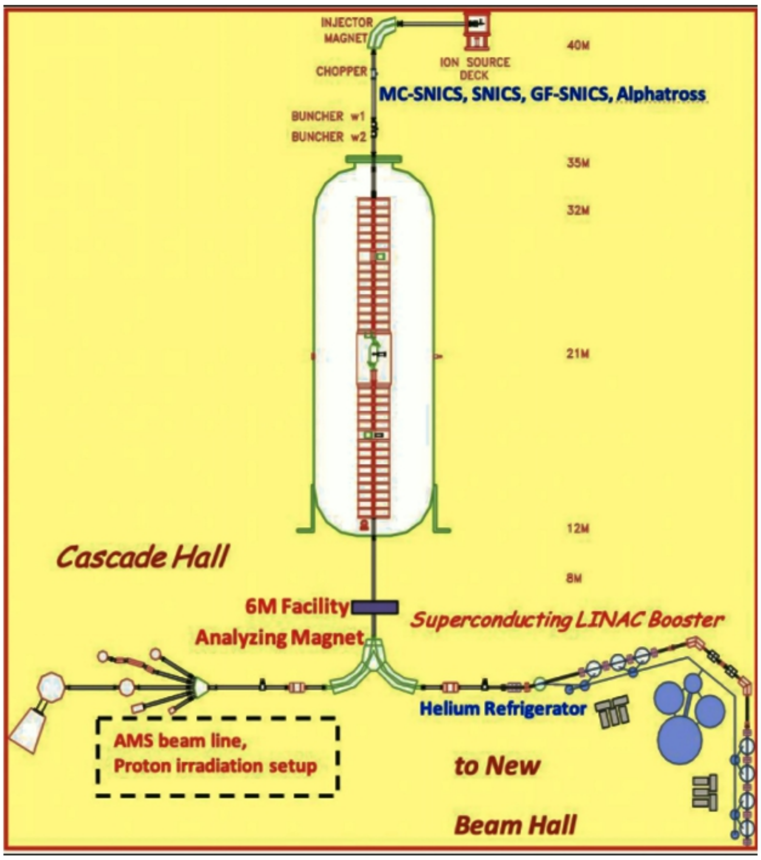

Figure 3.4: A schematic diagram of the BARC-TIFR 14UD Pelletron-LINAC accelerator facility located in Mumbai, India.

a high positive charge. The charge state will depend on the type of the accelerating ions, the terminal voltage, and the stripper. During the second stage of acceleration, the energy of the ions gets boosted to qeV_T (where q is the charge state of the positive ion beam), due to the repulsion experienced from the positive terminal voltage. In this manner, ions injected into the vertical column gain a total energy of (q+1)eV_T in tandem mode before reaching the analyzing magnet at the bottom. An analyzing magnet is used to select the beam with the required charge state and energy and finally directed towards the Palletron beam Hall. With the help of a switcher magnet, it can be further directed into one of the five beam lines namely, 0°, 15° N, 15° S, 30° N, and 30° S. The measurements presented in this thesis were conducted using a general-purpose scattering chamber.

3.2.2 Target Preparation

Target preparation is a crucial part of performing a nuclear experiment. While preparing the target, the thickness of the target is an important parameter that must be determined based on various experimental considerations. To achieve a higher reaction rate, thick targets should be used. However, to ensure accurate measurements, the observables emitted during the reaction must not be confined within the target, making it essential to determine the optimal target thickness for the experiment. Surrogate experiments require two targets: one for the desired reaction and the other for the reference reaction. Both should be self-supporting with an approximate thickness in the range of 500–900 μg/cm^2. Thin nuclear targets can be prepared using various methods, such as electron beam deposition, thermal evaporation, rolling, electroplating, and pulsed laser deposition. The choice of method will depend on the specific properties of the target.

For the present study, a self-supporting thin metallic target made of natural iron (^{56}Fe, with 91.754% abundance), with a thickness of $\approx$ 700 μg/cm^2, was prepared using the rolling method. Inorder to soften the sample for better rolling, natural Fe sample was heated in a tungsten boat for up to 30 minutes at 400°C. Rolling was then performed using a metal rolling machine available in the target laboratory at TIFR, Mumbai. To prepare cobalt (^{59}Co) target, which is 100% abundant, thermal evaoration technique were used. The melting point of cobalt is 1495°C, boiling point is 2927°C and density is 8.834 g/cm^3. Aluminium foil with a thickness of 2 mg/cm^2 was used as the backing, and after thermal evaporation of cobalt, it was removed. A self supporting cobalt target of thickness approximately 650 μg/cm^2 was obtained.

3.2.3 Semiconductor detectors

In a nuclear reaction experiment, detectors play a crucial role in identifying the reaction products. Neutrons, gamma rays, charged particles, and other products formed in the reaction are detected through their interactions with the detector material. Among the various types of detectors, semiconductor radiation detectors are widely used for charged particle spectroscopy, providing precise measurements in nuclear experiments. Specifically, silicon and germanium are utilized widely due to their small band gap (∼1.1eV for Si and ∼0.72eV for Ge), their linear response w.r.t energy of incident particles, and very high density. Semiconductor detectors are essentially reverse-biased p-n junction diodes, with the active volume of the detector determined by the thickness of the depletion region. In the present study Silicon surface barrier detectors (SSB) and single sided silicon strip detectors were used to detect the charged particle. The SSB detector is a p-n-type silicon diode with a thin depletion layer. It is made of n-type silicon with one of the surface is coated with gold (typically ∼40 μg/cm2) after etching and the other surface coated with a thin layer of aluminum (typically ∼40 μg/cm2) to provide electrical contact. Si strip detectors are segmented n-type or p-type (doped) semiconductor detectors. Strip detectors are large area detectors and are segmented into several strips for position resolution. In our experiments, we have used strip detectors of 50 mm x 50 mm area segmented into 50 mm x 3.1 mm sized sixteen strips, vertically.

3.2.4 Charged particle detection using semiconductor detector

As the charged particle passes through a semiconductor detector, it will interact with the orbital electrons inside the atom of the detector material. This Coulomb interaction will result in the reduction of energy of the interacting charged particles. The energy loss of the charged particle passing through the detector material is calculated using the Bethe-Bloch formula[10], which is given in Eq. 3.9.

$$-\frac{dE}{dx} = \frac{4\pi e^4 z^2 NB}{m_0 v^2} \tag{3.9}$$

where

$$B = Z\left[ln\left(\frac{2m_0 v^2}{I}\right) - ln(1-\frac{v^2}{c^2}) - \frac{v^2}{c^2})\right] \tag{3.10}$$

The negative sign in Eq. 3.9 indicates that the particle's energy decreases as it traverses through the material. The symbol v represents the velocity, and ze is the charge of the incident particle. The variables m_0, and e correspond to the rest mass and the electronic charge of the electron, respectively. Similarly, N, Z, and I represent the atomic density, the atomic number, and the ionization potential of the material, respectively. The nature of Eq. 3.10 describes a slow variation with the particle's energy. For non-relativistic particles, $v^2 = \frac{2E}{M}$, where E is the kinetic energy and M is the mass of the particle. Thus, the nature of the stopping power can be approximated as

$$-\frac{dE}{dx} \propto \frac{M(ze)^2}{E} \tag{3.11}$$

According to Eq. 3.11, if we allow the charged particle to first pass through a thin detector (ΔE) and then through a thick detector (E), which is enough to stop the particle and plot the energy loss as ΔE vs E, we will get a rectangular hyperbola. Here, the position of the hyperbola will depend on the M(ze)^2 value of the charged particle. Thus, we can uniquely identify the projectile-like fragments passing through the detectors.

3.2.5 Experimental setup

The experimental setup for the present measurement is shown in Fig. 3.5. ^{6}Li beam obtained from the palletron was used as the projectile for both the transfer reactions. The compound nucleus ^{58}Co* and ^{61}Ni* were populated at the same excitation energies $\approx$ 20-32 MeV with beam energy of 35.9 MeV incident on ^{nat}Fe and 40.5 MeV on ^{59}Co, respectively.

To identify the projectile-like fragments (PLFs), a silicon surface barrier detector telescope T was mounted inside the scattering chamber at an angle of 25^0 from the beam direction around the grazing angle. The telescope T consists of ΔE-E detectors with thickness of 150 μm and 1 mm. To record the evaporated particles from the compound nucleus, 2 sets of strip detectors S$_1$ and S$_2$ are placed in the backward angles covering an angular range of 110^0-130^0 and 140^0-160^0. Thickness of ΔE strip detector is $\approx$ 60 μm and that of E is $\approx$ 1500 μm and having an active area $\approx$50 mm$\times$50 mm. The evaporating protons from the compound nucleus ^{58}Co and ^{61}Ni in the two different transfer reactions are identified in strip detectors in coincidence with the outgoing alphas for both ^{58}Co and ^{61}Ni

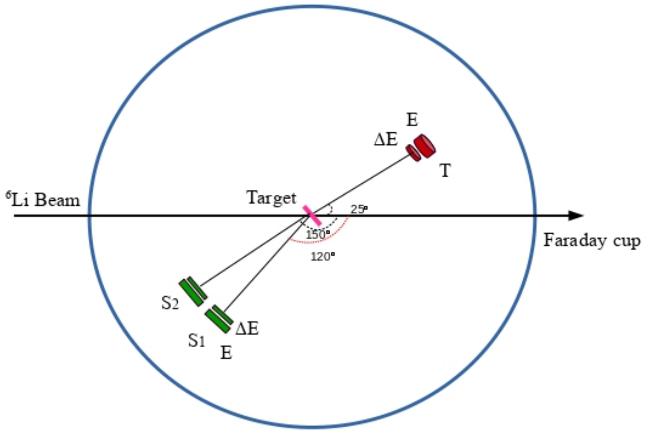

Figure 3.5: The schematic diagram of the experimental setup. T represents the particle telescope for identifying projectile-like fragments (PLF) from the transfer reactions, and S_1 and S_2 are the strip detectors to detect decaying particles from the compound nuclei. The detectors are placed inside the scattering chamber of 1.5 m diameter.

using the same telescope. Inorder to isolate the random coincidences, a time-to-amplitude converter (TAC) between the projectile-like fragments, detected in the telescope and the decay particles, detected in strips, was generated.

3.2.6 Detector calibration

The telescope T and strip telescopes S_1 and S_2 were calibrated using the discrete energy spectrum of ^{16}O* obtained from the experiment ^{12}C(^{6}Li,d)^{16}O* at 18 MeV with a beam current 3nA. The detectors were placed as shown in Fig. 3.5. The deuteron PLF energy has been calculated using the relation,

$$E_d = E_{beam} + Q - E_{lev} \tag{3.12}$$

where Q is the q-value of the calibration reaction and E_{lev} is the energies correspond to different excited levels of ^{16}O formed in the experiment. The energy calibration was also performed using the known energies of α particles from plutonium and americium (Pu-Am) α sources. Details of the radiation sources, used in the calibration process are

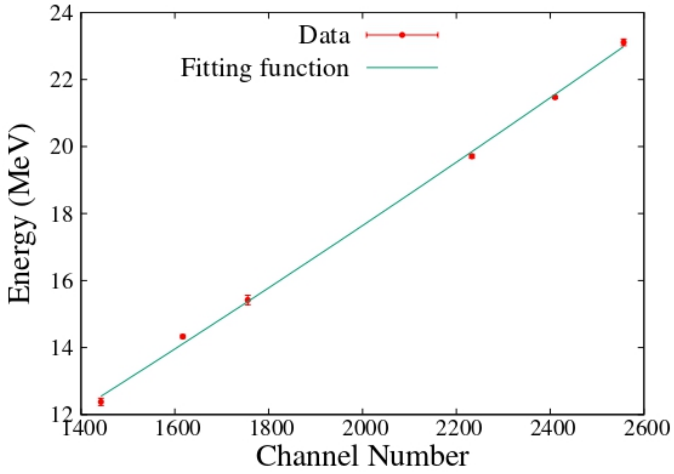

Figure 3.6: Calibration of telescope T

tabulated in Table 3.5. Calibration plot corresponding to telescope T is shown in Fig. 3.6.

Table 3.5: Details of the calibration sources

Source	Half-life (years)	α energies (MeV)	Intensity
^{239}Pu	24,110	5.156	70.77%
^{241}Am	43	5.485	84.8%

3.2.7 Electronic setup and signal processing

The block diagram for the electronic setup associated with the present experiment is illustrated in Fig. 3.7. The most crucial information obtained from a detector is the energy data and the timing data. The electronic devices used for energy processing are pre-amplifier (PRE-AMP), amplifier (AMP), and analog-to-digital converter (ADC), and the same but for time processing are timing filter amplifier (TFA), constant fraction discriminator (CFD), time-to-digital converter (TDC), LOGIC unit, gate and delay generator (GDG).

In the present experimental setup a pre-amp MSI-8 (Mesytec) with 8 channels is used for the SSB detector, while an MPR-16 (Mesytec) with 16 channels is used for the silicon strip detectors, to integrate and convert the current signal from the detector into a voltage

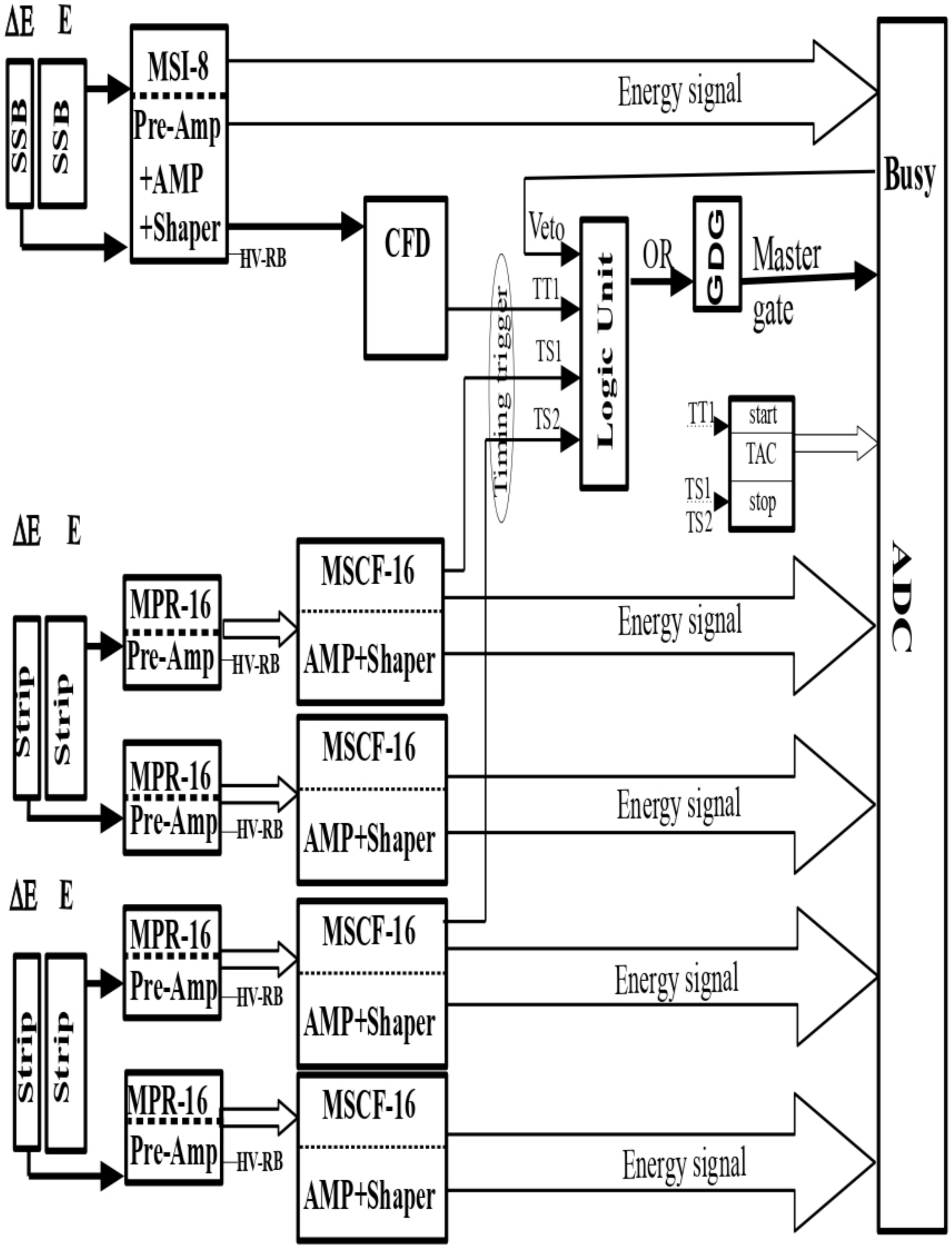

Figure 3.7: The schematic representation of elctronic setup.

pulse. When the projectile beam strikes the target material, the telescope T begins to collect the charged particles incident it. Consequently, a timing signal is generated from the E detector of telescope T and processed through the MSI-8 module. The voltage signal from the pre-amp is then fed to a gain amplifier/shaper (AMP) to optimize the signal-to-noise ratio. The MSI-8 module, which includes both a pre-amp and amplifier, is used for the SSB detector, while the MSCF-16 module serves as the amplifier for the silicon strip detector. The gain of the amplifier can be adjusted to ensure the voltage signal falls within the ADC range. The amplified signal is then fed to the ADC, where it is converted from an analog to a digital signal. In this setup, a CAEN V-785 was used as the ADC. Similarly, timing signals from strip detectors S_1 and S_2 are obtained from their respective E detectors using the MSCF-16 module. The TFA provides precise timing signals after amplifying and filtering, typically used to indicate the start time. However, even though the TFA produces output signals that exceed a certain threshold, electronic noise can cause some spread in the output signal, potentially degrading the timing resolution. To address this issue, a CFD is incorporated into the electronic setup to minimize the spread in the timing signal. In the CFD, the input signal is split into two paths—one is attenuated to a fraction of its original amplitude, while the other is delayed and inverted. These two signals are then merged to produce a constant fraction bipolar pulse. Timing jitter and signal spread are minimized by carefully optimizing the zero-crossing reference and delay. The coincidence events between two different detectors were recorded through a TAC. The TAC has two inputs: one for the start pulse, which is typically obtained from the first detector, and the other for the stop signal from the second detector. The resulting output is a rectangular voltage pulse with a width proportional to the time difference between the start and stop pulses. This output signal from the TAC is then directly fed into the ADC. A LINUX-based data collection program named LAMPS[11] is used to acquire and store all signals from the entire data acquisition system.

3.2.8 Data analysis

Two body kinematics are employed to analyze the data obtained in the experiment. The energy of the α particle detected in telescope T is used in determining the excitation energy corresponding to the compound nucleus formed. Here, the compound nucleus formed are ^{58}Co in ^{56}Fe(^{6}Li,α) reaction and ^{61}Ni in ^{59}Co(^{6}Li,α) reaction. The two-body kinematic equation used for the excitation energy determination is given by

$$E_{beam} + E_{target} = E_{ejectile} + E_{recoil} + Q + E_x \tag{3.13}$$

here E_{beam} is the beam energy, after the energy loss in the target half-thickness, E_{target} is the energy of the target, which is usually zero for immobile target, $E_{ejectile}$ is the energy of the PLF detected in telescope T, E_{recoil} is the recoil energy of the residual nucleus, Q is the q value of the corresponding transfer reaction and E_x is the excitation energy of the residual nucleus. The energy of the ejectile can be determined from the 2D spectra corresponding to telescope T, following energy calibration. A coincidence is established between the PLF detected in the telescope and the evaporation particle detected in the strip detector. Using these quantities, the excitation energy, E_x, can be calculated via Equation 3.13. The decay probability can then be determined by the ratio of the coincidence count for the evaporation particles detected in the strip detector to the singles count for the PLF detected in the telescope.

Bibliography

[1] M. Vretenar. Linear accelerators. *Proceedings of the CAS-CERN Accelerator School: Advanced Accelerator Physics*, 2013.

[2] T. C. Zhu and Ken K.-H. Wang. *Linear Accelerators (LINAC)*, pages 437–450. Springer Berlin Heidelberg, Berlin, Heidelberg, 2013.

[3] S.V. Kutsaev, R. Agustsson, A. Arodzero, R. Berry, A. Bezhanov, S. Boucher, O. Chimalpopoca, A. Diego, L. Faillace, D. Gavryushkin, M. Harrison, J.J. Hartzell, J. McNevin, M. Ruelas, A. Yu Smirnov, A. Verma, and K. Woods. Compact x-band electron linac for radiotherapy and security applications. *Radiation Physics and Chemistry*, 185:109494, 2021.

[4] Tim V., Günter K., and Gaj V. Calculation of true coincidence summing corrections for extended sources with efftran. *Applied Radiation and Isotopes*, 69(6):908–911, 2011.

[5] P.T. M. Shan, M.M. Musthafa, T. Najmunnisa, P. M. Aslam, K.K. Rajesh, K. Hajara, P. Surendran, J.P. Nair, A. Shanbagh, and S. Ghugre. Measurement of excitation functions and analysis of isomeric population in some reactions induced by proton on natural indium at low energy. *Nuclear Physics A*, 974:9–21, 2018.

[6] V. D. Nguyen, T. L. Nguyen, T. X. Nguyen, T. T. Kim, V. L. Bui, T. H. Nguyen, and Guinyun K. Measurement of the integrated cross section of 110pd(γ,n)109mpd, 110pd(γ,n)109gpd, and 110pd(γ,x)108mrh reactions with 70 mev bremsstrahlung. *Radiation Physics and Chemistry*, 203:110598, 2023.

[7] E. Robu and C. Giovani. Gamma-ray self-attenuation corrections in environmental samples. *Romanian Reports in Physics*, 61(2):295–300, 2009.

[8] Frederick C. H., Alvie A. A., Cheri A. M. D., Julius F. M. J., Abigaile M. V. J. H., Mon B. Z. G., Charlotte V. B., Girlie E. P. L., Neil R. D. G., and Alberto V. A. Epixs: A windows-based

program for photon attenuation, dosimetry and shielding based on epics2017 (endf/b-viii) and epdl97 (endf/b-vi.8). *Radiation Physics and Chemistry*, 182:109331, 2021.

[9] J. E. Escher, J. T. Harke, F. S. Dietrich, N. D. Scielzo, I. J. Thompson, and W. Younes. Compound-nuclear reaction cross sections from surrogate measurements. *Review of Modern Physics*, 84:353–397, Mar 2012.

[10] Emilio G. S., Hans A. B., Norman R., Philip S. M., and Bernard T. F. Experimental nuclear physics. 1953.

[11] A. Chatergee. Lamps.

Chapter 4

Measurement of the cross section for the ^{99}Tc$(\gamma,\gamma')^{99m}$Tc reaction

4.1 Introduction

^{99m}Tc with a half-life of 6 hours, is widely used for medical purposes as it emits 140 keV gamma radiation during its transition from the meta-stable to the ground state. The energy of the ^{99m}Tc is ideal for radiation imaging. The low-energy gamma radiation can easily be counted using gamma cameras. ^{99m}Tc ensures the patient radiation exposure to a minimum as it does not possess any unwanted beta or alpha radiations. Molybdenum-99 having half-life 66 hours, decay to isomeric state of ^{99}Tc, is the radio-active parent of ^{99m}Tc. The partial decay scheme for the ^{99}Mo isotope, based on ENSDF data[1], is presented in Fig. 4.1. Approximately 82% of ^{99}Mo undergoes β^- decay to form ^{99m}Tc. The ^{99m}Tc then decays to its ground state by emitting a 140.5 keV gamma ray. This ground-state technetium will remain as radioactive nuclear waste due to its longer half-life (10^5 Y). The most common and accepted route for the production of ^{99}Mo is the fission of Highly Enriched Uranium (HEU) in nuclear reactors. ^{99}Mo with high specific activity can be produced through this process. This ^{99}Mo is used as Mo-Tc generators to produce ^{99m}Tc for practical purpose. During the fission process, large quantities of unwanted fission products are formed along with ^{99}Mo. Hence this method requires expensive processing facilities after irradiation for the separation of highly toxic radiation emitters.

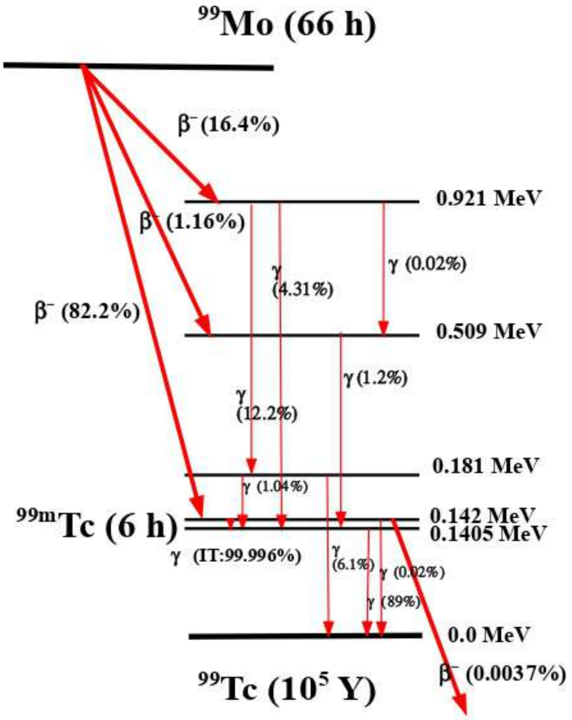

Figure 4.1: The partial decay scheme for the ^{99}Mo isotope

Currently, Technetium-Molybdenum generators which contain ^{99}Mo are used for producing ^{99m}Tc. However, there are certain downside for the usage of generator to produce ^{99m}Tc in hospitals. During the production of ^{99}Mo, the ^{99m}Tc also begins to produce as a decay product. This ^{99m}Tc will complete 4 half-lives in 24 hours due to its shorter half-life. In hospitals, the generators are usually replaced after one week of continuous use and after a few months, they get discarded as radioactive waste. A major portion of ^{99m}Tc isotope is lost due to time consumption in the chemical processing, transportation delay from the production site to the hospitals, storage period in the hospitals etc. Hence at the hospitals, very limited quantity of ^{99m}Tc is available for practical medical purpose. ^{99m}Tc is isolated from the generator through a process known as elution[2].

In the case of ^{99}Tc, a significant quantity is produced during the fission process, which ultimately remains as nuclear waste [3]. The leftover technetium from Mo-Tc generators used in hospitals also contributes to nuclear waste. Technetium-99 causes serious hazards to the environment and human health due to its potential solubility in the natural surface and water bodies, long half-life and radiotoxicity[4–6]. Natural transmutation of technetium-99 to a shorter half-life or stable product generally takes 10^{15} years. This longer duration will adversely affect the environment. Further, this will require large reservoirs for the storage of these long-lived isotopes till their complete conversion into stable products. Inorder to reduce the transmutation time, thermal neutron capture is the transmutation method presently proposed by various research groups[7]. The accelerator-driven transmutation (ADT)[8] systems are generally proposed to work in the sub-critical condition. During the ADT operation, there may be a chance for the excess production of neutrons, which further affects the criticality of the reactor. In addition to this, the neutron capture will open up other reaction channels leading to the production of unwanted isotopes having a longer half life. Hence, an efficient method is the re-utilization of this long lived technetium-99 to produce medically important ^{99m}Tc radioisotope.

Table 4.1: Details of the photon induced reactions of the sample and the monitor.

Isotope of interest	Reaction Channel	Threshold Energy (keV)	Gamma Energy (keV)	Branching ratio(%)	Half-life hours
^{99m}Tc	$^{99}\text{Tc}(\gamma,\gamma\prime)^{99m}\text{Tc}$	140	140	89±4	6
^{115m}In	$^{115}\text{In}(\gamma,\gamma\prime)^{115m}\text{In}$	336	336	45.9±0.1	4.48

4.2 Experimental details

The experiment was carried out at KIMS hospital, Trivandrum, utilizing the Varian CLINAC-iX Medical Linear Accelerator (LINAC) facility. Bremsstrahlung photon beams of endpoint energies 4, 6, 9, 12, 16, and 20 MeV were produced by an electron LINAC. The electron beam of corresponding energy to fall on a 1 mm thick lead target. The current of the electron beam was 35 μA during the time of irradiation. $^{115}\text{In}(\gamma,\gamma\prime)^{115m}\text{In}$ reaction has been used as a monitor reaction, for the flux normalization of the bremsstrahlung spectrum. Natural Indium foil of thickness 388 mg/cm^2 was used as a monitor target.

Details of important quantities of the reactions and the isotope are shown in Table 4.1. The masses used in the calculation were taken from the 2020 Atomic Mass Evaluation by M. Wang et al.[9], and the decay data were obtained from the ENSDF database [1].

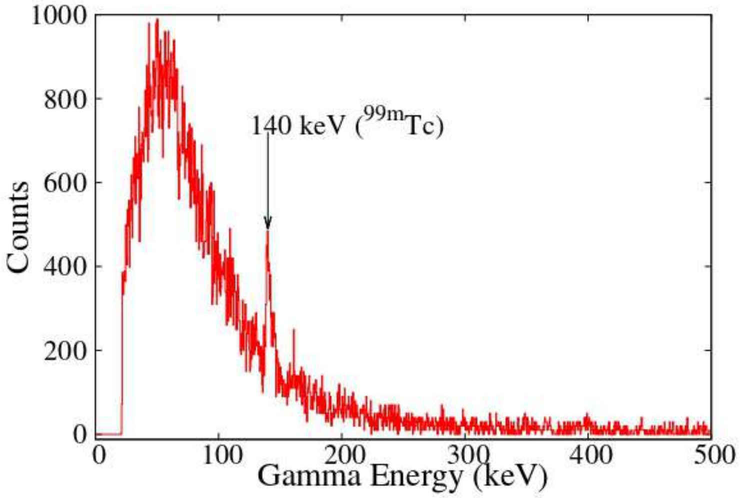

Figure 4.2: Gamma ray spectrum measured for ^{99m}Tc using CZT detector at 20 MeV bremsstrahlung photon.

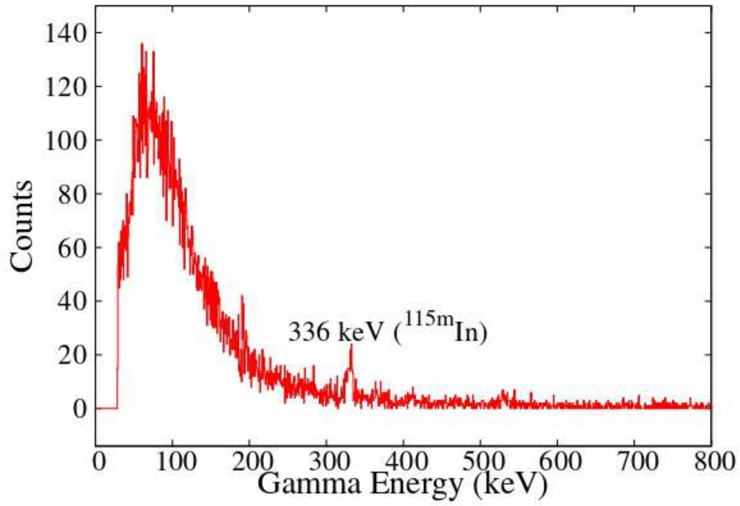

Figure 4.3: Gamma ray spectrum measured for ^{115m}In using CZT detector at 20 MeV bremsstrahlung photon.

The leftover ^{99}Tc isotope from the generator itself has been used to study the production of ^{99m}Tc radiopharmaceutical. The liquid target of ^{99}Tc was taken in a cylindrical geometry with dimension 2 cm×2 cm placed in the beam path along with the monitor target and irradiated for 20 minutes with a dose rate of 1000 cGy/min. The number of particles in the target was calculated from the loaded activity of ^{99}Mo used in the generator and from the elution efficiency. The sample and the monitor were irradiated simultaneously to ensure that the same beam flux is reaching on both of them. Sufficient cooling time was allowed after the irradiation. The activity of the irradiated samples was counted for 6 hours using Kromeck CZT (Cadmium Zinc Telluride) semiconductor detector with crystal dimensions 1 cm×1 cm×1 cm. A typical gamma ray spectrum obtained for ^{99m}Tc and ^{115m}In, at bremsttrahlung end point energy 20 MeV is shown in Figs. 4.2 and 4.3 respectively.

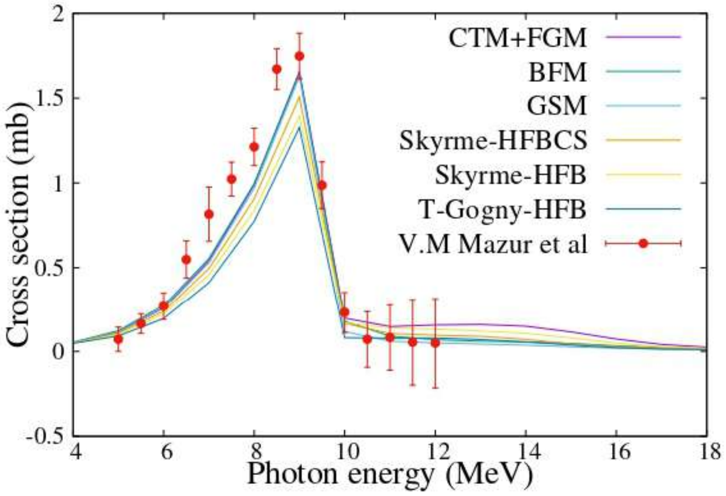

Figure 4.4: Experimental cross section of ^{115}In$(\gamma,\gamma\prime)^{115m}$In reaction taken from EXFOR along with TALYS model predictions.

4.3 Result and Discussions

The integral cross section for the ^{99}Tc$(\gamma,\gamma\prime)^{99m}$Tc reaction was determined using the yield ratio obtained through the activation technique. The statistical nuclear reaction code TALYS 1.96[10] has been used for the theoretical model calculations. The experimental data of ^{115}In$(\gamma,\gamma\prime)^{115m}$In reaction was taken from EXFOR nuclear data library[11]. Different level density models viz. the Constant Temperature + Fermi Gas Model (CTM+FGM) [12], the Back-shifted Fermi Gas Model (BFM) [13], the Generalized Superfluid Model (GSM) [14], the Skyrme-Hartree-Fock BCS model [15], the Skyrme-

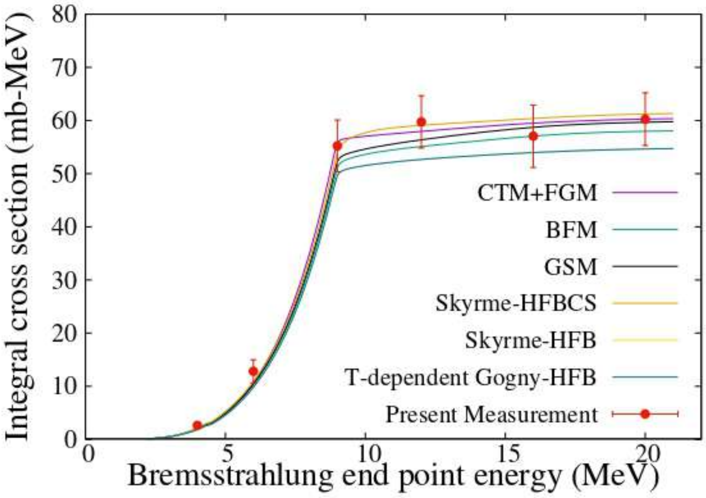

Figure 4.5: Integral cross section of ^{99}Tc$(\gamma,\gamma\prime)^{99m}$Tc reaction along with theoretical predictions for different level density models.

Hartree-Fock-Bogoliubov model [16], and the Temperature-dependent Gogny-Hartree-Fock-Bogoliubov models [17] described in Chapter 2 were utilized in the theoretical model calculations. The experimental monitor data taken from EXFOR data library, along with the theoretical predictions is shown in Fig 4.4. A χ^2 minimized approach is applied to determine the best theoretical model, and Back-shifted Fermi gas model appears the best-predicting model among different level density models. The Back-shifted Fermi gas Model treats the levels of the excited nucleus as equally spaced single-particle state. The integral cross section of the reaction ^{115}In$(\gamma,\gamma\prime)^{115m}$In is calculated theoretically, corresponding to the minimum χ^2 value. The intgration is performed from threshold upto bremsstrahlung endpoint energy. The yield of the sample and the monitor was determined using the Eq. 3.4 given in Chapter 3. By utilizing the sample-to-monitor yield ratio and the integral cross section of the ^{115}In$(\gamma,\gamma\prime)^{115m}$In reaction, we determined the integral cross section for the ^{99}Tc$(\gamma,\gamma\prime)^{99m}$Tc reaction, using Eq. 3.7 in Chapter 3. The uncertainties associated with the counts of gamma peaks, corresponding intensities, detector efficiency, the number of target atoms for both the sample and the monitor, isotopic abundance, and time-related factors are included in the calculation. The errors associated to the efficiency estimation is primarily generated from the uncertainty in the activity of the standard source and the counting statistics. The uncertainties in the detector efficiency from the standard source

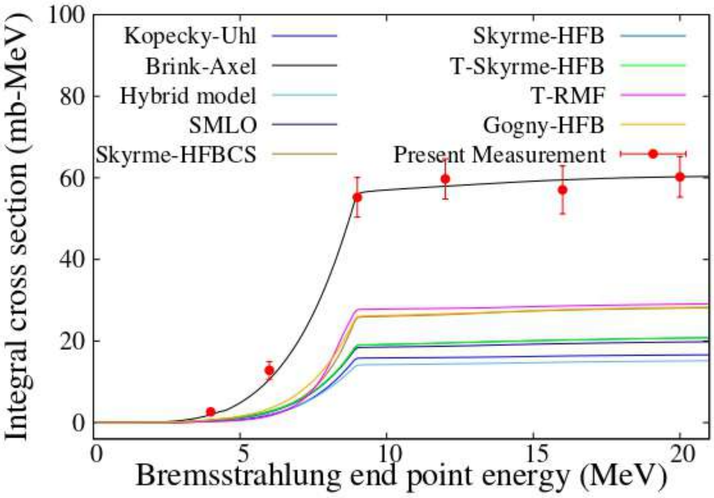

Figure 4.6: Integral cross section of $^{99}\mathrm{Tc}(\gamma,\gamma\prime)^{99m}\mathrm{Tc}$ reaction along with theoretical predictions for different strength function models.

contributes about 0.1%. To estimate the efficiency of the cylindrical sample geometry, a Monte Carlo approach was employed, incorporating factors like cylindrical sample geometry, attenuation within the sample container, properties of the bulk liquid, and detector specifications. This calculation introduced a Monte Carlo uncertainty of approximately 0.7%.

Table 4.2: The theoretical integral cross section of the monitor and the integral cross section of the $^{99}\mathrm{Tc}(\gamma,\gamma\prime)^{99m}\mathrm{Tc}$ reaction corresponding to each bremsstrahlung end point energies.

Bremsstrahlung	Integral cross section of	
end point energy	$^{115}\mathrm{In}(\gamma,\gamma\prime)^{115m}\mathrm{In}$	$^{99}\mathrm{Tc}(\gamma,\gamma\prime)^{99m}\mathrm{Tc}$
(MeV)	TALYS optmized (mb-MeV)	Present measurement (mb-MeV)
4	0.68	2.62±0.5
6	7.78	12.81±2.18
9	57.52	55.22±4.88
12	63.93	59.73±4.93
16	65.32	57.05±5.87
20	65.49	60.24±4.96

The theoretical integral cross section of the $^{115}\mathrm{In}(\gamma,\gamma\prime)^{115m}\mathrm{In}$ reaction, and the final integral cross section determined for $^{99}\mathrm{Tc}(\gamma,\gamma\prime)^{99m}\mathrm{Tc}$ along with their associated uncertainties, are summarized in Table 4.2. Figure 4.5 shows the integral cross section of the $^{99}\mathrm{Tc}(\gamma,\gamma\prime)^{99m}\mathrm{Tc}$ reaction along with the theoretical predictions performed using TALYS

1.96 nuclear reaction code. The Constant Temperature + Fermi Gas Model (CTM+FGM) of level density is found to be the best model explaining the present experimental data, with minimum χ^2 value. The theoretical data for all level density models show strong agreement with current measurements. The cross section displays an increasing trend up to 9 MeV, after which it remains nearly constant within the bremsstrahlung photon end-point energy range of 9 to 20 MeV. A measurement by Sekine *et al.*[18] also indicates a constant behavior for the integral cross section of ^{99}Tc$(\gamma,\gamma\prime)^{99m}$Tc in the energy range of 15 to 50 MeV. However, their study did not measure the lower energy region. Table 4.3 presents a comparison between the current data and the previous measurement conducted by Sekine *et al.* The integral cross section of ^{99}Tc$(\gamma,\gamma\prime)^{99m}$Tc obtained at the same energies exhibits a difference of one order of magnitude. This contrast is also observed in the integral cross section of ^{115}In$(\gamma,\gamma\prime)^{115m}$In, which serves as the monitor data for determining the final cross sections. In the present study, Mazur *et al.*'s data, well reproduced with theoretical nuclear model calculations from the TALYS code has been employed. The corresponding integral cross section for ^{115}In$(\gamma,\gamma\prime)^{115m}$In reaction obtained is around 60 mb-MeV. Hence, the observed order difference may be attributed to the utilization of distinct sets of ^{115}In$(\gamma,\gamma\prime)^{115m}$In data in determining the ^{99}Tc$(\gamma,\gamma\prime)^{99m}$Tc integral cross sections.

Table 4.3: Comparison of present measurement with the previously reported data of ^{99}Tc$(\gamma,\gamma\prime)^{99m}$Tc

Energy (MeV)	Integral cross section of ^{99}Tc$(\gamma,\gamma\prime)^{99m}$Tc (mb-MeV)	
	Present work	Literature
50	—	5.5±1.5
30	—	5.7±0.4
20	60.24±4.96	6.9±0.4
16	57.05±5.87	—
15	—	5.5±0.6
12	59.73±4.93	—
9	55.22±4.88	—

We have also investigated the dependence of the present data on the photon strength function models, as this posess a crucial role in the photonuclear cross section. Analysis performed utilizing various PSF models viz. Kopecky-Uhl model [19] the Brink-Axel

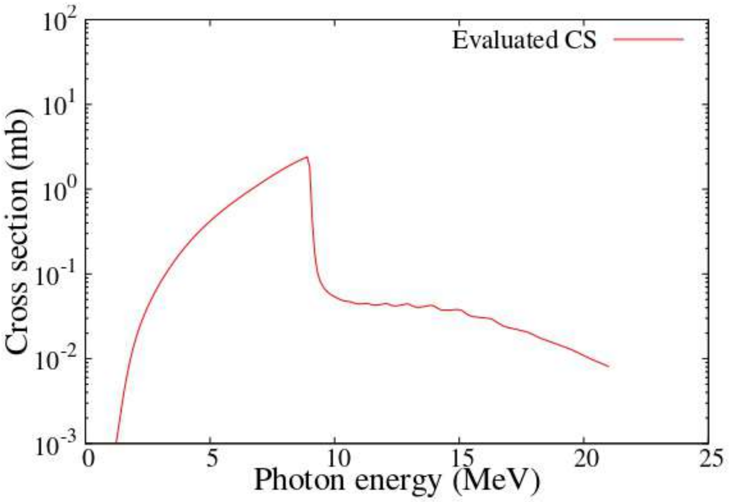

Figure 4.7: The excitation function derived for $^{99}\mathrm{Tc}(\gamma,\gamma\prime)^{99m}\mathrm{Tc}$ reaction using TALYS 1.96 code.

Lorentzian model [20, 21], Goriely's hybrid model [22], the Simplified Modified Lorentzian model (SMLO) [23], the Skyrme-Hartree-Fock BCS model (Skyrme-HFBCS) [24], the Skyrme-Hartree-Fock Bogoliubov model (Skyrme-HFB) [25], the Temperature-dependent Skyrme-Hartree-Fock Bogoliubov model (T-Skyrme-HFBCS) [25], the Temperature-dependent Relativistic Mean Field model (T-RMF) [26], and the Gogny-Hartree-Fock-Bogoliubov model (Gogny-HFB) [27], is shown in Fig. 4.6. From the figure, it is clear that the Brink-Axel Lorentzian model is the best strength function model predicting the present measured data. The total cross sections were derived utilizing the optimized models, i.e, Constant Temperature + Fermi Gas Model (CTM+FGM) of level density and Brink-Axel model of strength function. Corresponding plot is shown in Fig.4.7. The ^{99m}Tc production cross section is found to be increasing up to 8.9 MeV and after that, a sharp decrease in the cross section is observed. Above this energy threshold, neutron emission becomes the dominant process, with a neutron separation energy of 8.9 MeV. As a result, for the efficient production of ^{99m}Tc, it is crucial to concentrate efforts below the particle emission threshold, where a sufficiently high photon flux can be maintained to optimize the production process.

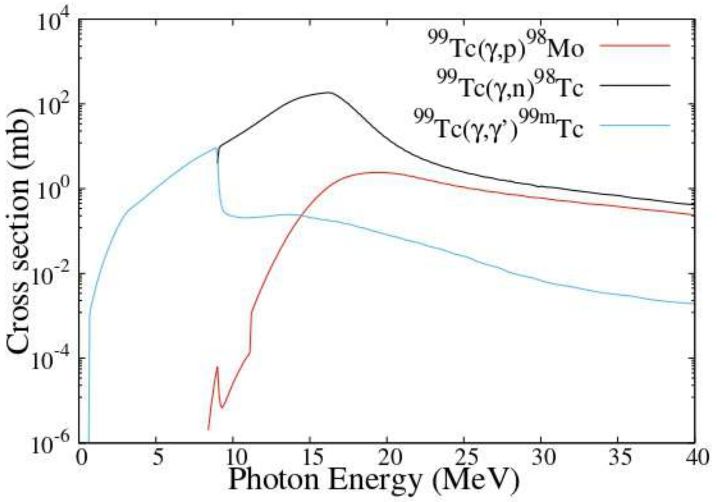

Figure 4.8: TALYS 1.96 model calculation of major channels produced in the photon induced reaction on ^{99}Tc isotope.

Table 4.4: Transmutation rate for a 1g technetium sample across various channels

Channels	Transmutation rate ($\times 10^{6}$/s)
$(\gamma, \gamma\prime)$	45.57
(γ, p)	1.63
(γ, n)	429

4.3.1 Transmutation via (γ, p) channel

We have investigated the re-utilization of ^{99}Tc isotope through (γ, γ') channel, leading to the production of ^{99}Tc. The transmutation probability of the long-lived radioisotope ^{99}Tc is also evaluated theoretically via the (γ, p) channel, which leads to the production of stable ^{98}Mo. Optimized theoretical parameters, such as level density and gamma-ray strength functions, are employed in the calculations. Major reaction channels in the photon-induced reactions on ^{99}Tc, including (γ, γ'), (γ, p), and (γ, n), were calculated using the theoretical code TALYS 1.96, as shown in Fig. 4.8. The figure clearly demonstrates that the production of ^{99m}Tc increases up to 8.9 MeV, after which a sharp decline in the cross section occurs as the incident energy approaches the neutron separation energy. Beyond this threshold, the nucleus begins to emit neutrons, marking a significant change in the reaction dynamics. The (γ, n) reaction channel then leads to the production of ^{98}Tc, a nuclear waste with a considerably longer half-life (4.2 × 10^{6} years). Notably, the cross section for the (γ, n) channel is significantly higher than that of the (γ, p) transmutation channel, emphasizing the challenges associated with managing the resulting nuclear waste.

The transmutation rates for irradiating a 1-gram technetium sample under typical flux conditions for 20 minutes across various reaction channels are presented in Table 4.4. The transmutation rate for the (γ, p) channel is significantly smaller compared to the (γ, n) channel. Therefore, the transmutation of ^{99}Tc to stable ^{98}Mo is only feasible when high-flux photon beams are employed below the neutron threshold energy. However, rather than focusing on transmutation, a better approach to minimize the disposal of ^{99}Tc as radioactive waste from hospitals is to reutilize the ^{99}Tc isotope. Available electron LINAC in hospitals can be used for this purpose, enabling the in-house production of the ^{99m}Tc isotope.

4.4 Conclusions

The integral cross section of the reaction $^{99}\mathrm{Tc}(\gamma, \gamma\prime)^{99m}\mathrm{Tc}$ is determined with bremsstrahlung photon beam of endpoint energies 4, 6, 8, 12, 16, and 20 MeV. The total production cross section of ^{99m}Tc is estimated using parameter values that were experimentally optimized. Although the cross sections are relatively low, this method proves to be highly beneficial for the local production of the ^{99m}Tc radioisotope. Furthermore, the transmutation potential of the photon beam is thoroughly investigated. The long-lived ^{99}Tc isotope can be efficiently transmuted into the stable ^{98}Mo isotope through the (γ,p) reaction channel, provided the photon beam is of sufficiently high intensity and the energy is maintained below the neutron separation energy. However, transmuting ^{99}Tc into stable ^{98}Mo is practically difficult under these conditions. In contrast, the threshold for initiating the (γ, γ') reaction is only 140 keV, which is far below the particle emission threshold. This suggests that reutilizing ^{99}Tc offers a better solution for nuclear waste management, as no particle emissions or contamination channels occur below 6.5 MeV

Bibliography

[1] National Nuclear Data Center. Evaluated nuclear structure data file (ensdf). `https://www.nndc.bnl.gov/ensdf/`, 2025. Accessed: 2025-08-04.

[2] J. L. Vučina. Elution efficiency of mo 99/tc 99m generators. *Physics, Chemistry and Technology*, 2(3):125–130, 2001.

[3] E.R. Merz. Nuclear waste: A source of valuable raw material or just a troublesome pollutant? In *Energy: Money, Materials and Engineering*, Institution of Chemical Engineers Symposium Series, pages T4–1–T4–13. Pergamon, 1982.

[4] Ruby P., Jaison M., Puja ., Siddhartha M., and Ramyakrishna K. Chapter 40 - microbial bioremediation and biodegradation of radioactive waste contaminated sites. In Junaid Ahmad Malik, editor, *Microbes and Microbial Biotechnology for Green Remediation*, pages 733–746. Elsevier, 2022.

[5] Malcolm Joyce. Chapter 5 - the actinides and related isotopes. In Malcolm Joyce, editor, *Nuclear Engineering*, pages 87–110. Butterworth-Heinemann, 2018.

[6] P.A. Taylor. 10 - physical, chemical, and biological treatment of groundwater at contaminated nuclear and norm sites. In Leo van Velzen, editor, *Environmental Remediation and Restoration of Contaminated Nuclear and Norm Sites*, Woodhead Publishing Series in Energy, pages 237–256. Woodhead Publishing, 2015.

[7] Vladimir P., Viacheslav R., Andrei K., Valeriy ., Iury T., Konstantin R., Lidia L., Sergey R., and Victor E. Technetium transmutation and production of artificial stable ruthenium. *Comptes Rendus Chimie*, 7(12):1215–1218, 2004.

[8] A Stanculescu. Accelerator driven systems (ads) and transmutation of nuclear waste: Options and trends, Dec 2001.

[9] M. Wang, W.J. Huang, F.G. Kondev, G. Audi, and S. Naimi. The ame 2020 atomic mass evaluation (ii). tables, graphs and references*. *Chinese Physics C*, 45(3):030003, mar 2021.

[10] A. J. Koning, S. Hilaire, and S. Goriely. *Talys User Manual, A NuclearReaction Program.* NRG-1755 ZG PETTEN, Netherlands(2017).

[11] V.M. Mazur, I.V. Sokolyuk, Z.M. Bigan, and I.Yu. Kobal. Nuclear isomer excitation cross section in $(\gamma, \gamma\prime)$-m reactions at 4 - 15 mev. *Yadernaya Fizika*, 56, 1993.

[12] A. Gilbert and Cameron. A composite nuclear-level density formula with shell corrections. *Canadian Journal of Physics*, 43:1446, January 1965.

[13] W. Dilg, W. Schantl, H. Vonach, and M. Uhl. Level density parameters for the back-shifted fermi gas model in the mass range 40 ¡ a ¡ 250. *Nuclear Physics A*, 217(2):269–298, 1973.

[14] A V Ignatyuk, K K Istekov, and G N Smirenkin. Collective effects in level density, and the probability of fission. *Sov. J. Nucl. Phys. (Engl. Transl.); (United States)*, 30:5, 11 1979.

[15] S. Goriely, F. Tondeur, and J.M. Pearson. A hartree–fock nuclear mass table. *Atomic Data and Nuclear Data Tables*, 77(2):311–381, 2001.

[16] S. Goriely, S. Hilaire, and A. J. Koning. Improved microscopic nuclear level densities within the hartree-fock-bogoliubov plus combinatorial method. *Physical Review C*, 78:064307, Dec 2008.

[17] S. Hilaire, M. Girod, S. Goriely, and A. J. Koning. Temperature-dependent combinatorial level densities with the d1m gogny force. *Physical Review C*, 86:064317, Dec 2012.

[18] Tsutomu Sekine, Kenji Yoshihara, László Lakosi, Zsolt Németh, and Árpád Veres. Integral cross section of the 99tc$(\gamma, \gamma\prime)$99mtc reaction in the 15–50 mev energy region. *International Journal of Radiation Applications and Instrumentation. Part A. Applied Radiation and Isotopes*, 42(2):149–153, 1991.

[19] J. Kopecky, M. Uhl, and R. E. Chrien. Radiative strength in the compound nucleus ^{157}Gd. *Physical Review C*, 47:312–322, Jan 1993.

[20] D.M. Brink. Individual particle and collective aspects of the nuclear photoeffect. *Nuclear Physics*, 4:215–220, 1957.

[21] P. Axel. Electric dipole ground-state transition width strength function and 7-mev photon interactions. *Physical Review*, 126:671–683, Apr 1962.

[22] S. Goriely. Radiative neutron captures by neutron-rich nuclei and the r-process nucleosynthesis. *Physics Letter B*, 436:10–18, 1998.

[23] V. Plujko, O. Gorbachenko, and K. Solodovnyk. Description of nuclear photoexcitation by lorentzian expressions for electric dipole photon strength function. *European Physical Journal A*, 55:014327, Nov 2019.

[24] S. Goriely and E. Khan. Large-scale qrpa calculation of e1-strength and its impact on the neutron capture cross section. *Nuclear Physics A*, 706(1):217–232, 2002.

[25] S Goriely, E Khan, and M Samyn. Microscopic hfb + qrpa predictions of dipole strength for astrophysics applications. *Nuclear Physics A*, 739(3):331–352, 2004.

[26] I. Daoutidis and S. Goriely. Large-scale continuum random-phase approximation predictions of dipole strength for astrophysical applications. *Physical Review C*, 86:034328, Sep 2012.

[27] S. Goriely, S. Hilaire, S. Péru, and K. Sieja. Gogny-hfb+qrpa dipole strength function and its application to radiative nucleon capture cross section. *Physical Review C*, 98:014327, Jul 2018.

Chapter 5

Measurement of the cross section for the ^{19}F(γ,n)^{18}F reaction

5.1 Introduction

^{18}F is commonly used for positron emission tomography (PET) scanning due to its properties as a pure positron emitter[1, 2]. The partial decay scheme for the ^{18}F isotope is presented in Fig. 5.1. ^{18}F provides 97% positron emission with a maximum energy of 635 keV in a shorter half-life period (109 min). This isotope has also been identified as the only low-energetic positron emitter used in PET scanning. The low energetic positron with a low diffusion rate provides high-resolution PET images. The shorter half-life helps the patients to lose the activity received in a shorter time. Further, ^{18}F will decay to stable ^{18}O so that the patient does not receive any unwanted exposure. Along with its nuclear properties, the chemical properties such as a small van der Waals radius, the ability to form a strong bond with carbon, and high electronegativity make ^{18}F a unique candidate among all other positron emitters. In clinical oncology, ^{18}F is used as 2-[^{18}F]fluoro-2-deoxy-D-glucose ([^{18}F]FDG). In addition to the application in PET, ^{18}F is also utilized in gamma cameras for tracer studies in bone scanning scintigraphy[3]. Due to its bone imaging capability, ^{18}F may be given orally or intravenously so that 50% of it accumulates in the bone.

Presently, ^{18}F is produced via the proton irradiation on enriched water target ($H_2^{18}O$)[4, 5] at a typical proton beam energy of 18 MeV, utilizing a cyclotron facility. The cyclotron production yields an aqueous solution of fluoride ion ($^{18}F_2$). However, the use of enriched ^{18}O target, which has only 0.2% natural abundance, makes the method much costlier. In the production using water target, the so-produced ^{18}F contained in water is allowed to pass through a quaternary ammonium column to trap the ^{18}F ion, which is then eluted by an aqueous base solution. In this mode of production, there may be a chance of mixing the radioisotope with toxic hydrogen fluorides, which will affect the patients. Further, the primary proton beam used in the production of ^{18}F and the energetic neutrons produced within the reaction can produce a large number of unwanted radioisotopes along with ^{18}F. In this procedure, a major radionuclide impurity formed is ^{13}N through the reaction ^{16}O(p,α)^{13}N, having high cross section in the energy range 6-20 MeV. Further, ^{13}N may be found in different forms viz. nitrites, nitrates and N_2 gas, with varying toxicity. An alternative method for producing ^{18}F involves irradiating ^{20}Ne with deuterons through $^{20}\mathrm{Ne}(d,\alpha)^{18}\mathrm{F}$. This two-step process results in ^{18}F in its gaseous form. The primary advantage of this method over the ^{18}O(p,n)^{18}F reaction is the high abundance of ^{20}Ne (90.48%) gas targets. However, producing a deuteron beam using a cyclotron makes this method more challenging. Additionally, this process generates toxic fluorine gas, which is highly corrosive and can damage transfer lines and the target. Various other reaction channels, such as ^{19}F(n,2n)^{18}F[6], ^{16}O(t,n)^{18}F[7], and ^{23}Na(γ, αn)^{18}F[8], have also been investigated by different research groups for producing the ^{18}F isotope. Among these, ^{19}F(n,2n)^{18}F is carried out using reactor neutrons. For the production of ^{16}O(t,n)^{18}F, tritium (^{3}H) is first generated through the reaction ^{6}Li(n, α)^{3}H. Due to the two-step nature of this process, the reaction rate is very low. ^{23}Na(γ, αn)^{18}F is produced using high energy photons of microtron bremsstrahlung with NaOH as the target.

In this context, both theoretical analysis and logical exploration suggest that the utilization of the ^{19}F(γ,n)^{18}F reaction channel presents a promising alternative for the production of ^{18}F. Fluorine is monoisotopic, and various ^{19}F compounds are widely available, making it a practical choice. Furthermore, medical linear accelerators, capable of generating

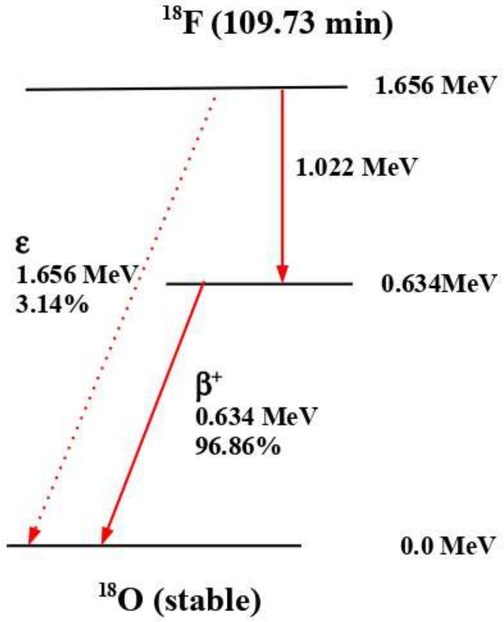

Figure 5.1: The partial decay scheme for the ^{18}F isotope.

bremsstrahlung with endpoint energies up to 20 MeV, are commonly found in radiation therapy centers, which are occupied by experienced radiation professionals. This method offers several advantages, including cost-effectiveness, the elimination of hazardous HF gas production, and the reduction of isotope transportation losses, as it enables local production. Additionally, this approach significantly minimizes contamination from competing reaction channels, resulting in a cleaner and more efficient production route. Moreover, most of the isotopes generated within this energy range are stable. A summary of the probable reaction channels below 20 MeV, including their threshold energies and typical TALYS-simulated peak cross sections, are provided in Table 5.1. Notably, the $(\gamma,p\alpha)$ reaction, which produces ^{14}C with a threshold energy of 14.23 MeV, is the only channel that results in the production of a radioisotope. Moreover, the β^- radiation emitted from ^{14}C is of very low energy with longer half-life. Presice cross section data for the ^{19}F$(\gamma,n)^{18}$F reaction and competing channels is essential to optimize both experimental and theoretical conditions for the production of ^{18}F through photonuclear reactions.

Table 5.1: Probable photon-induced reaction channels of ^{19}F and their corresponding threshold energies.

Isotope	Reaction Channel	Threshold Energy (MeV)	Half-life	TALYS simulated Peak cross section (mb)	TALYS simulated at Energy (MeV)
^{15}N	^{19}F(γ,α)	4.01	Stable	2.56	16.9
^{18}O	^{19}F(γ,p)	7.99	Stable	1.87	17.3
^{18}F	^{19}F(γ,n)	10.43	Un-stable	4.53	17
^{16}O	^{19}F(γ,t)	11.7	Stable	0.45	14.2
^{17}O	^{19}F(γ,d)	13.82	Stable	0.79	20.1
^{14}C	^{19}F(γ,pα)	14.23	Un-stable	0.74	21.6
^{14}N	^{19}F(γ,nα)	14.85	Stable	5.03	21
^{11}B	^{19}F(γ,2α)	15.01	Stable	0.43	23.7

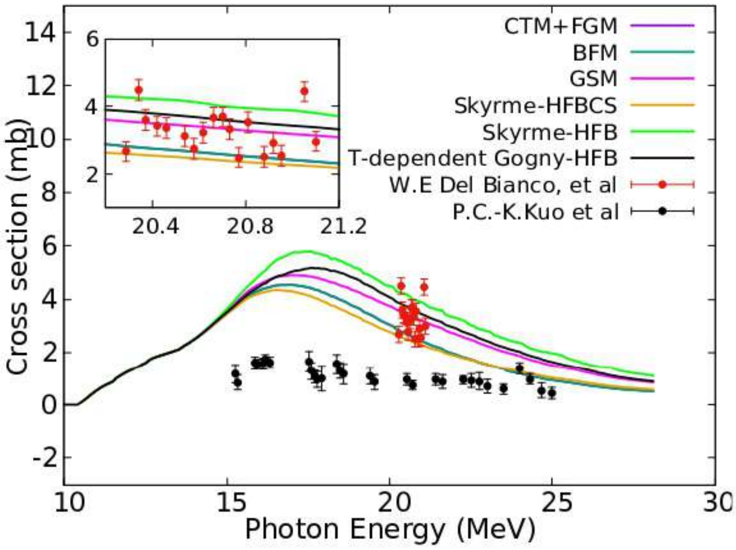

Figure 5.2: Experimental data of ^{19}F(γ, n)^{18}F reaction taken from EXFOR data library, along with theoretical model calculations using TALYS 1.96 code.

Currently, there are limited energy-dependent cross section data[9–11] for the ^{19}F(γ, n)^{18}F reaction available in the literature, and these data exhibit large discrepancies both among themselves and when compared with theoretical predictions using code TALYS 1.96[12], as shown in Fig. 5.2. Kuo *et al.*[9] performed the experiment using bremsstrahlung photon employing neutron time of flight method, determining the n_0 cross section, populating the ground state of ^{18}F with the objective of determining resonance width leading to a discrepancy in the integral cross section. Sherman *et al.*[10] used the same technique and shows comparable results for the integral cross section but including n_1 colony. Del Bianco *et al.*[11] determined the cross section with monoenergetic photons produced

Table 5.2: Details of the photon induced reactions of the sample and the monitor.

Isotope of interest	Mass	Reaction Channel	Threshold Energy (MeV)	Gamma Energy (keV)	Branching ratio (%)	Half-life
^{18}F	18	^{19}F(γ,n)^{18}F	10.43	511	193.46±0.08	109.8 min
^{114m}In	114	^{115}In(γ,n)^{114m}In	9.04	190	15.56±0.15	49 days

Table 5.3: The bremsstrahlung end point energies, irradiation time and dose rate for each irradiation is given

Bremsstrahlung end point energy (MeV)	Irradiation time (Minutes)	Dose rate (Grey/min)	Beam current (Electron) (μA)
20	20	10	35
14.6	15	6	12.36
12	10	6	9.03

from a proton-induced nuclear reaction on tritium isotope. They counted the positrons emitted from ^{18}F isotope using a 2π proportional counter. However, the experimental data shows multiple peaks within a very narrow energy range (which is shown in the inset figure), which the theoretical models fail to explain. Kato and Oka[13] measured the relative yield of the reaction ^{19}F(γ,n)^{18}F using the bremsstrahlung activation technique at bremsstrahlung endpoint energies above 30 MeV. However, at energies above 30 MeV, contamination channels are found to be prominent. Hence, the generation of systematic data covering wide range of energies, above threshold up to 20 MeV, is essential for theoretical modelling for the estimation of actual isotopic yield. With this objective, we have measured the integral ^{19}F(γ,n)^{18}F cross section over the energy range from threshold to 20 MeV, where contamination from other component in the compound is minimum. Measuring the integral cross section is important, as it allows the determination of the isotope's production yield from the entire bremsstrahlung spectrum, from the threshold up to the endpoint energy. Hence, we have measured the integral cross section using a monitor reaction, which was irradiated under the same beam conditions and at the same time. In the present study, the photonuclear reaction ^{19}F(γ,n)^{18}F is investigated using LiF as the target material. A detailed description of the experimental setup and methodology is provided in the subsequent sections.

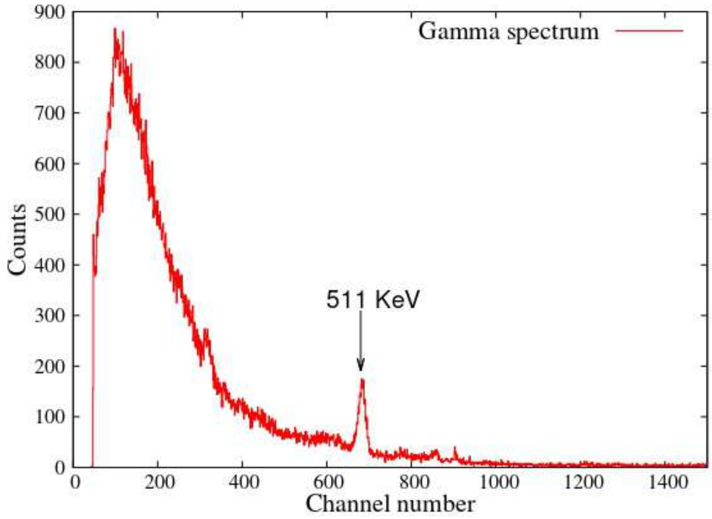

Figure 5.3: Gamma ray spectrum measured for ^{18}F using CZT detector at 20 MeV bremsstrahlung photon.

5.2 Experimental details and data analysis

The experiment was carried out at two different Medical Linear Accelerator (LINAC) facilities: 20 MeV bremsstrahlung energy at Kerala Institute of Medical Sciences (KIMS), Trivandrum, and 14.6 MeV and 12 MeV bremsstrahlung photon endpoint energies at Malabar Cancer Centre (MCC), Thalassery. The bremsstrahlung photon beam was produced by directing an electron beam of the corresponding energy onto a 1 mm thick lead target. A comprehensive overview of the reactions and the produced isotope is provided in Table 5.2. The masses used in the calculation were taken from the 2020 Atomic Mass Evaluation by M. Wang et al.[14], and the decay data were obtained from the ENSDF database [15]. Details of the sample were provided in Chapter.3. Both the sample and the monitor target were positioned in the beam path and irradiated simultaneously to ensure that both targets received the same beam flux. The photon energy, irradiation time, electron beam current, and dose rate are shown in Table 5.3. Sufficient cooling time was allowed after the irradiation. The activity of the irradiated samples was counted for 6 hours using Kromeck CZT (Cadmium Zinc Telluride) semiconductor detector with crystal dimensions 1cm×1cm×1cm. A typical gamma ray spectrum obtained for both ^{18}F and ^{114m}In, at bremsstrahlung end point energy 20 MeV is shown in Figs. 5.3 and 5.4

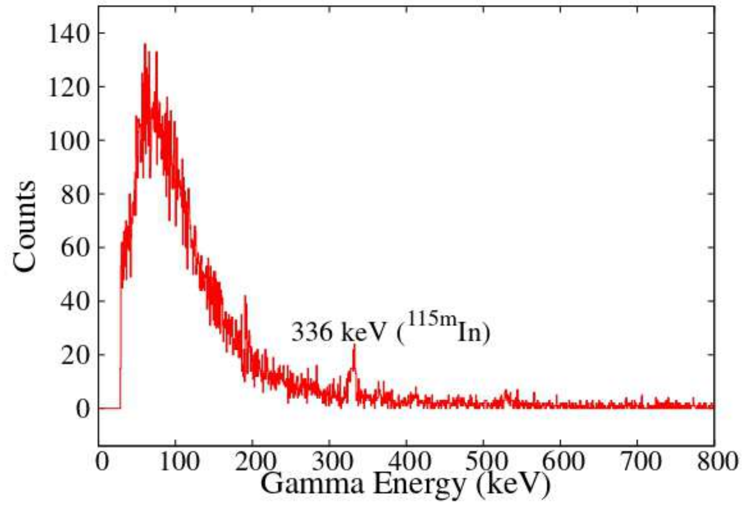

Figure 5.4: Gamma ray spectrum measured for ^{114m}In using CZT detector at 20 MeV bremsstrahlung photon.

respectively.

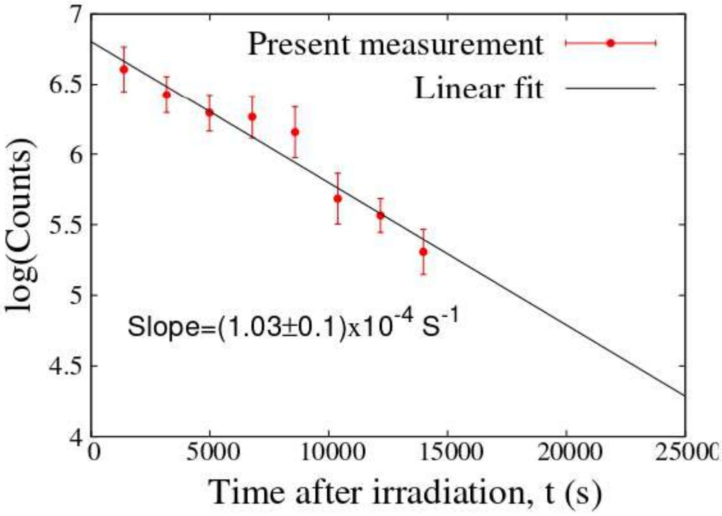

Figure 5.5: Time dependence of the counts in the decay of ^{18}F after irradiating LiF sample at 20 MeV bremsstrahlung photon.

In ^{18}F, two 511 keV gamma rays were produced from the annihilation of positrons (β^+) with the electrons. The two simultaneously produced gamma radiation will be emited at an angle of 180^0. In the present experimental set up, the coincidence measurement of both the gamma rays are not possible. Hence, to confirm that the 511 keV gamma rays are solely coming from ^{18}F, we have determined the decay constant obtained from the measurement.

Activity of the sample was counted for 30 minutes time interval and the log of the count rate was plotted against time after irradiation. In order to obtain accurate count rate, the background count consisting of naturally occurring β^+ emitters were subtracted. Fitting the data linearly gives the decay constant of ^{18}F, which is found to be (1.03±0.1)x10^{-4} S^{-1}. This confirms that the counted 511 keV gammas are coming from the activated ^{18}F isotope only. Present measurement along with linear fit are shown in Fig. 5.5. In this study, the reaction ^{115}In(γ,n)^{114m}In was used as the monitor reaction, with the corresponding data measured by Bohinyuk *et al,*[16], obtained from the EXFOR[17] data library.

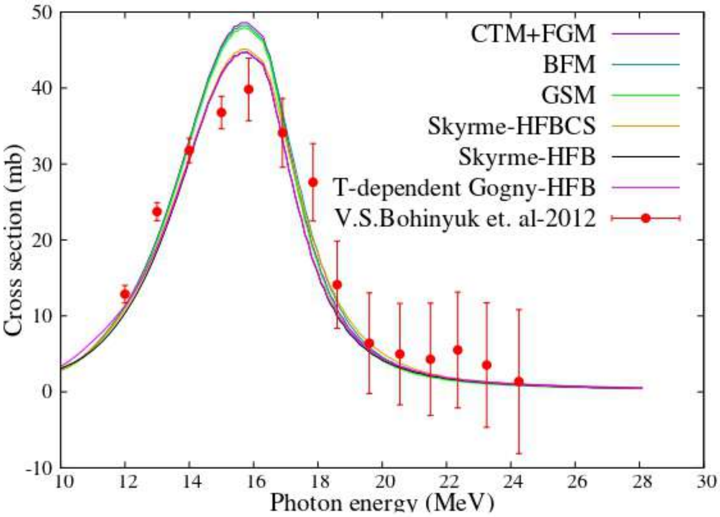

Figure 5.6: Experimental cross section of ^{115}In(γ,n)^{114}In reaction taken from EXFOR along with Talys model predictions.

Table 5.4: The measured yield ratio of the sample to monitor corresponding to each bremsstrahlung end point energies along with photopeak acivity of ^{18}F.

Bremsstrahlung end point energy (MeV)	Yield ratio $\frac{Y_{^{18}F}}{Y_{^{114m}In}}$	Photopeak Activty ^{18}F (cpm/mg)
20	0.126	11.68
14.6	0.0697	3.65
12	0.0693	0.83

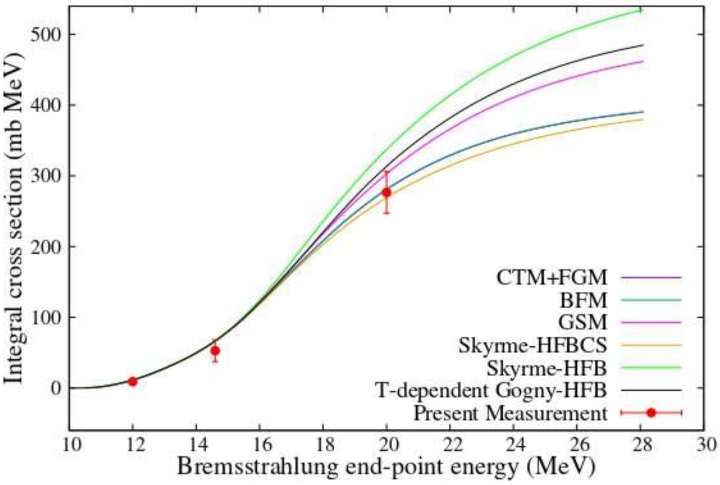

Figure 5.7: Integral cross section of ^{19}F(γ,n)^{18}F reaction along with theoretical predictions for different level density models.

5.3 Result and Discussions

The radioisotope ^{18}F has been produced via the reaction ^{19}F(γ,n)^{18}F using the photon activation technique. LiF samples with various thicknesses were used in the measurements at three different photon energies above the threshold. The yield ratio of ^{18}F to ^{114m}In obtained at different bremsstrahlung endpoint energies are shown in the Table 5.4, along with the photopeak activity, which is presented in the units of counts per minute per milligram (cpm/mg) of the sample. The activity is found to be increasing with beam energy, beam current and irradiation time.

The integral cross section of the reaction ^{19}F(γ,n)^{18}F at bremsstrahlung endpoint energies of 12, 14.6, and 20 MeV has been determined using the measured yield ratio. The experimental data for the monitor reaction ^{115}In(γ,n)^{114m}In were taken from the experimental nuclear data library EXFOR. The experimental ^{115}In(γ,n)^{114m}In data were plotted along with the energy-dependent cross section calculated using TALYS 1.96, for various level density models are shown in Fig. 5.6. Different level density models viz. the Constant Temperature + Fermi Gas Model (CTM+FGM) [18], the Back-shifted Fermi Gas Model (BFM) [19], the Generalized Superfluid Model (GSM) [20], the Skyrme-Hartree-Fock BCS model [21], the Skyrme-Hartree-Fock-Bogoliubov model [22], and the Temperature-dependent Gogny-Hartree-Fock-Bogoliubov models [23] are incorporated in TALYS 1.96. Through χ^2 minimization, it was found that the Skyrme-Hartree-Fock BCS model of level density as the best model explaining the experimental data for ^{115}In(γ,n)^{114m}In reaction. The integral cross section thus calculated using optimized nuclear level density parameter for this reaction was taken as the monitor for determining the integral cross section for ^{18}F production at this energy, applying correction for threshold energy shift.

Table 5.5: The theoretical integral cross section of the monitor and the integral cross section of the ^{19}F(γ,n)^{18}F reaction.

Bremsstrahlung end point energy (MeV)	Integral cross section of ^{115}In(γ,n)^{114m}In TALYS optmized (mb-MeV)	Integral cross section of ^{19}F(γ,n)^{18}F Present measurement (mb-MeV)
20	2195	276.53±29.35
14.6	522.5	43.94±15.42
12	131.6	9.08±1.46

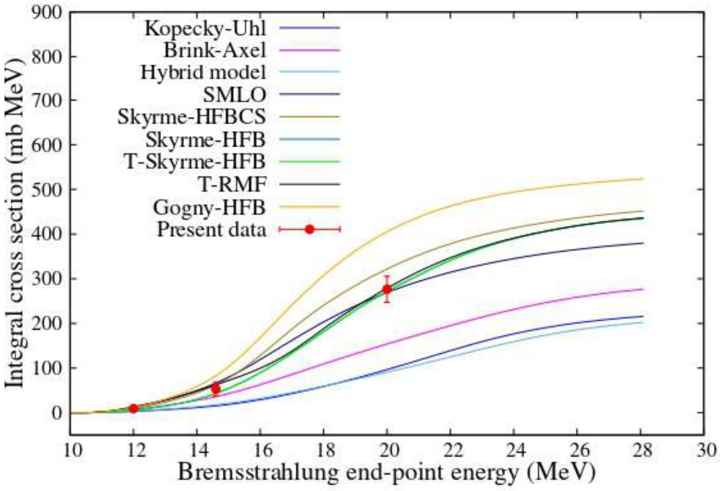

Figure 5.8: Integral cross section of ^{19}F(γ,n)^{18}F reaction along with theoretical predictions for different strength function models.

The integral cross sections of the ^{19}F(γ,n)^{18}F reaction for different bremsstrahlung endpoint energies, along with the theoretical integral cross section of the monitor reaction, ^{115}In(γ,n)^{114m}In, are tabulated in Table 5.5. Inorder for the completeness of analysis, attempt has been made to optimize the theoretical parameters for the desired reaction. Accordingly, the experimental data for ^{19}F(γ,n)^{18}F are plotted in Fig. 5.7

along with the predictions for various level density models from the TALYS code. The χ^2 analysis shows that the Skyrme-HFBCS model predicts the experimental data very well. Further, predictions of phenomenological models (lying one on another) also agree well with the experimental data. As a part of theoretical optimization,

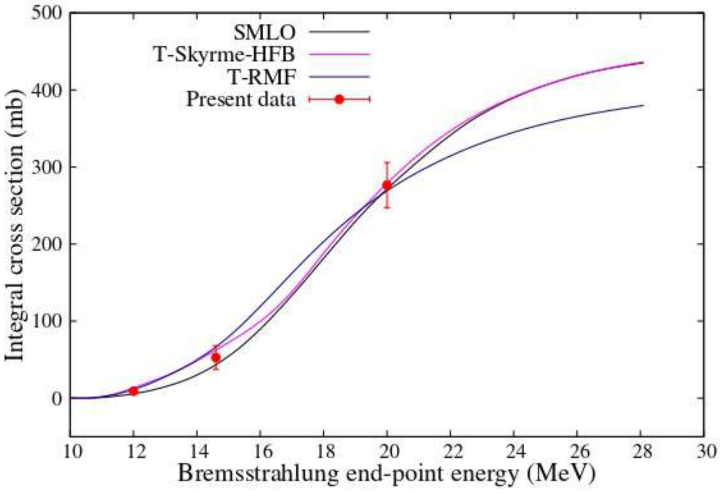

Figure 5.9: Same as Fig. 5.8, but only the matching strength function models are considered for clarity.

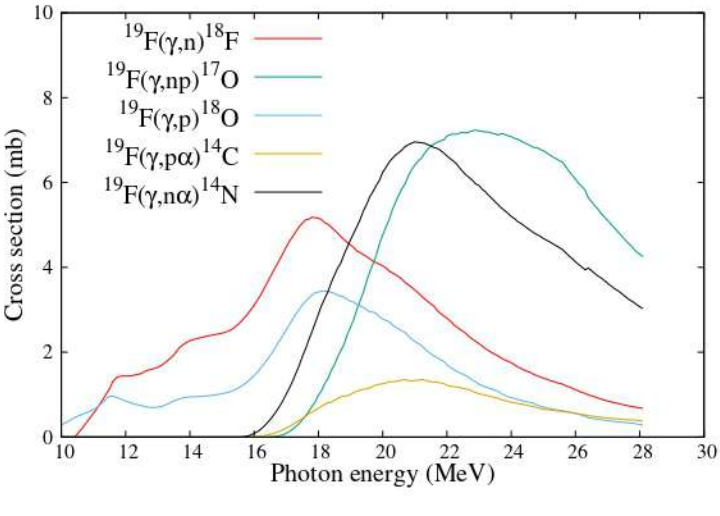

Figure 5.10: Total theoretical cross section for different photon-induced channels, obtained using the TALYS 1.96 code with optimized level density and strength function models.

analyses were also performed with various photon strength function models viz. the

Kopecky-Uhl model [24] the Brink-Axel Lorentzian model [25, 26], the Goriely's hybrid model [27], the Simplified Modified Lorentzian model (SMLO) [28], the Skyrme-Hartree-Fock BCS model (Skyrme-HFBCS) [29], the Skyrme-Hartree-Fock Bogoliubov model (Skyrme-HFB) [30], the Temperature-dependent Skyrme-Hartree-Fock Bogoliubov model (T-Skyrme-HFB) [30], the Temperature-dependent Relativistic Mean Field model (T-RMF) [31], and the Gogny-Hartree-Fock-Bogoliubov model (Gogny-HFB) [32], as shown in Fig. 5.8. The strength function models themselves exhibit significant deviations. However, the Simplified Modified Lorentzian model, the Temperature-dependent Skyrme-Hartree-Fock Bogoliubov model, and the Temperature-dependent Relativistic Mean Field model are found to be consistet with the present data as shown in Fig. 5.9. Among them, χ^2 minimization shows the Temperature-dependent Relativistic Mean Field model, which accounts for width spreading, deformation effects, and temperature effects, as the best predicting model for ^{19}F(γ,n)^{18}F reaction. The large deviation observed in the integral cross section for both level density and strength function models may be due to the effect of the GDR phenomenon, which is observed in the energy region above 20 MeV for fluorine isotopes.

The total cross sections for various prominent photon-induced channels were derived using the optimized models, as shown in Fig. 5.10. From the figure, it is evident that the maximum production of ^{18}F occurs at the peak cross section near 17.8 MeV. At this energy, the contribution from other contamination channels is minimized.

5.4 Conclusions

The integral cross section of the ^{19}F(γ,n)^{18}F reaction was determined at bremsstrahlung photon endpoint energies of 12, 14.6, and 20 MeV, using ^{115}In(γ,n)^{114m}In for flux normalization. The experiments were carried out using the photon activation technique. The results were analyzed with the statistical nuclear reaction code TALYS 1.96, incorporating all the level density and photon strength function models. These measurements facilitated the optimization of theoretical models, including level density and photon strength function, which are critical for precise yield determination, minimizing the contaminating channels.

Bibliography

[1] Didier Le Bars. Fluorine-18 and medical imaging: Radiopharmaceuticals for positron emission tomography. *Journal of Fluorine Chemistry*, 127(11):1488–1493, 2006. The Centenary of Henri Moissan's Nobel Prize.

[2] *Production and Quality Control of Fluorine-18 Labelled Radiopharmaceuticals*. Number 1968 in TECDOC Series. INTERNATIONAL ATOMIC ENERGY AGENCY, Vienna, 2021.

[3] Robert L. B., Chris R. W., John C. C., and Adam P. S. An introduction to na18f bone scintigraphy: Basic principles, advanced imaging concepts, and case examples. *Journal of Nuclear Medicine Technology*, 35(2):64–76, 2007.

[4] J.C. Clark and D.J. Silvester. A cyclotron method for the production of fluorine-18. *The International Journal of Applied Radiation and Isotopes*, 17(3):151–154, 1966.

[5] Allyson Bishop, N Satyamurthy, Gerald Bida, George Hendry, Michael Phelps, and Jorge R Barrio. Proton irradiation of [18o]o2: Production of [18f]f2 and [18f]f2 + [18f]of2. *Nuclear Medicine and Biology*, 23(3):189–199, 1996.

[6] C. L. Hartmann and P. M. DeLuca Jr. Measurement of the 19f(n,2n)18f cross section from 18 to 27 mev. *Nuclear Science and Engineering*, 109(3):319–323, 1991.

[7] A. Bishop, N. Satyamurthy, G. Bida, M. Phelps, and J. R. Barrio. Production of [18f]f2 using the 16o(3he,p)18f reaction. *Nuclear Medicine and Biology*, 23(4):385–389, 1996.

[8] R. A. Aliev, S. S. Belyshev, L. Z. Dzhilavyan, B. S. Ishkhanov, V. V. Khankin, and V. I. Shvedunov. Study of the possibility of the production and separation of the 18f radioisotope at electron accelerators. *Moscow University Physics Bulletin*, 69(3):233–236, May 2014.

[9] P.C.-K. Kuo, J.W. Jury, K.G. McNeill, N.K. Sherman, and W.F. Davidson. Photoneutron angular distribution of 19f. *Nuclear Physics A*, 499(2):328–338, 1989.

[10] N. K. Sherman, K. H. Lokan, and R. W. Gellie. Photoneutrons from 19f. *Canadian Journal of Physics*, 54(11):1178–1189, 1976.

[11] W. E. Del Bianco and W. E. Stephens. Photonuclear activation by 20.5-mev gamma rays. *Physical Review*, 126:709–717, Apr 1962.

[12] A. J. Koning, S. Hilaire, and S. Goriely. *Talys User Manual, A NuclearReaction Program.* NRG-1755 ZG PETTEN, Netherlands(2017).

[13] T. Kato and Y. Oka. Yields of photonuclear reactions for photon-activation analysis with high-energy bremsstrahlung. *Talanta*, 19(4):515–525, 1972.

[14] M. Wang, W.J. Huang, F.G. Kondev, G. Audi, and S. Naimi. The ame 2020 atomic mass evaluation (ii). tables, graphs and references*. *Chinese Physics C*, 45(3):030003, mar 2021.

[15] National Nuclear Data Center. Evaluated nuclear structure data file (ensdf). `https://www.nndc.bnl.gov/ensdf/`, 2025. Accessed: 2025-08-04.

[16] V.S.Bohinyuk, V.I.Zhaba, A.M.Parlag, and L.O.Shabalina. Research of excitation of the isomers states in (gamma,n)-reactions. *Scientific Herald of Uzhhorod University Series Physics*, (0):39–44, 2012.

[17] N. Otuka, E. Dupont, V. Semkova, B. Pritychenko, A.I. Blokhin, M. Aikawa, S. Babykina, M. Bossant, G. Chen, S. Dunaeva, R.A. Forrest, T. Fukahori, N. Furutachi, S. Ganesan, Z. Ge, O.O. Gritzay, M. Herman, S. Hlavač, K. Katō, B. Lalremruata, Y.O. Lee, A. Makinaga, K. Matsumoto, M. Mikhaylyukova, G. Pikulina, V.G. Pronyaev, A. Saxena, O. Schwerer, S.P. Simakov, N. Soppera, R. Suzuki, S. Takács, X. Tao, S. Taova, F. Tárkányi, V.V. Varlamov, J. Wang, S.C. Yang, V. Zerkin, and Y. Zhuang. Towards a more complete and accurate experimental nuclear reaction data library (exfor): International collaboration between nuclear reaction data centres (nrdc). *Nuclear Data Sheets*, 120:272–276, 2014.

[18] A. Gilbert and Cameron. A composite nuclear-level density formula with shell corrections. *Canadian Journal of Physics*, 43:1446, January 1965.

[19] W. Dilg, W. Schantl, H. Vonach, and M. Uhl. Level density parameters for the back-shifted fermi gas model in the mass range 40 ¡ a ¡ 250. *Nuclear Physics A*, 217(2):269–298, 1973.

[20] A V Ignatyuk, K K Istekov, and G N Smirenkin. Collective effects in level density, and the probability of fission. *Sov. J. Nucl. Phys. (Engl. Transl.); (United States)*, 30:5, 11 1979.

[21] S. Goriely, F. Tondeur, and J.M. Pearson. A hartree–fock nuclear mass table. *Atomic Data and Nuclear Data Tables*, 77(2):311–381, 2001.

[22] S. Goriely, S. Hilaire, and A. J. Koning. Improved microscopic nuclear level densities within the hartree-fock-bogoliubov plus combinatorial method. *Physical Review C*, 78:064307, Dec 2008.

[23] S. Hilaire, M. Girod, S. Goriely, and A. J. Koning. Temperature-dependent combinatorial level densities with the d1m gogny force. *Physical Review C*, 86:064317, Dec 2012.

[24] J. Kopecky, M. Uhl, and R. E. Chrien. Radiative strength in the compound nucleus ^{157}Gd. *Physical Review C*, 47:312–322, Jan 1993.

[25] D.M. Brink. Individual particle and collective aspects of the nuclear photoeffect. *Nuclear Physics*, 4:215–220, 1957.

[26] P. Axel. Electric dipole ground-state transition width strength function and 7-mev photon interactions. *Physical Review*, 126:671–683, Apr 1962.

[27] S. Goriely. Radiative neutron captures by neutron-rich nuclei and the r-process nucleosynthesis. *Physics Letter B*, 436:10–18, 1998.

[28] V. Plujko, O. Gorbachenko, and K. Solodovnyk. Description of nuclear photoexcitation by lorentzian expressions for electric dipole photon strength function. *European Physical Journal A*, 55:014327, Nov 2019.

[29] S. Goriely and E. Khan. Large-scale qrpa calculation of e1-strength and its impact on the neutron capture cross section. *Nuclear Physics A*, 706(1):217–232, 2002.

[30] S Goriely, E Khan, and M Samyn. Microscopic hfb + qrpa predictions of dipole strength for astrophysics applications. *Nuclear Physics A*, 739(3):331–352, 2004.

[31] I. Daoutidis and S. Goriely. Large-scale continuum random-phase approximation predictions of dipole strength for astrophysical applications. *Physical Review C*, 86:034328, Sep 2012.

[32] S. Goriely, S. Hilaire, S. Péru, and K. Sieja. Gogny-hfb+qrpa dipole strength function and its application to radiative nucleon capture cross section. *Physical Review C*, 98:014327, Jul 2018.

Chapter 6

Indirect determination of ^{58}Co(γ,xp) cross section

6.1 Introduction

As discussed in Chapter 1, different types of sources are available for performing photonuclear experiments. However, there are some limitations with these sources. The bremsstrahlung photons, which are the continuous photon source, require unfolding of the bremsstrahlung spectra to generate the required energy specific cross section [1]. The intensity of quasi monoenergetic photons, available from in-flight positron annihilation, is very low. Furthermore, there are systematic disagreements when comparing the results obtained from bremsstrahlung experiments with those from quasi-monoenergetic annihilation experiments [2]. These disagreements are observed in both the absolute magnitude and the shape of the cross section, arising from the differences in the experimental setup and the photon spectra used in the experiments. Other experimental methods, such as Laser Compton Scattered (LCS) photons and electron-tagged bremsstrahlung photons, are also used to generate energy-specific cross sections [3, 4], but the number of facilities that offer these techniques is few. Another important part in nuclear experiments is the target, which may be placed in a stationary position. The targets used in these experiments should be stable to avoid uncertainties associated with the half-life measurements.

However, the cross sections corresponding to unstable targets are also important in some areas of nuclear physics, especially in reactor physics and nuclear astrophysics. Since short half-life targets cannot be directly used in experiments, surrogate reaction technique [5], an indirect method, are considered as a better alternative to overcome such limitations.

A significant number of high energy photons are produced inside the fusion reactors as a result of neutron interaction with the structural materials and during the tritium breeding stage [6, 7]. The energetic photons also contribute to gas formation through the photonuclear reactions and result in swelling and stress formation. Hydrogen gas is one such product formed via (γ,xp) reaction channel. ^{58}Co(γ,xp) is one of the major reaction channels as we consider the production of hydrogen isotopes. ^{58}Co is an important radioisotope produced inside the nuclear reactor due to the continuous exposure of neutrons on the reactor structural materials. ^{58}Ni(n,p), ^{59}Co(n,2n), ^{60}Ni(n,t), etc. are the major pathways leading to the production of ^{58}Co. This is shown in the bock diagram 6.1. This ^{58}Co will undergo photon-induced reactions by the prompt gamma rays produced inside the reactor itself. Considering the ^{58}Co target which is highly unstable, the direct measurement of this reaction is not feasible. In the present work, the cross sections for ^{58}Co(γ,xp) reactions were determined via the surrogate technique, employing the surrogate ratio method. The compound nucleus ^{58}Co* was populated through the transfer reaction ^{56}Fe(^{6}Li,α) at $E_{lab} = 35.9$ MeV. The compound nucleus was formed over a wide range of excitation energies with the ^{6}Li beam energy of 35.9 MeV. The cross section of the ^{61}Ni(γ,xp) reaction, taken from the IAEA photonuclear database [8], was used as the reference reaction data to determine the ^{58}Co(γ,xp) cross section by applying the surrogate ratio method. The IAEA-recommended photonuclear data library had adopted KAERI data [9] for this nuclear reaction data. As of our knowledge, the cross section for the reaction, ^{58}Co(γ,xp), is being reported for the first time.

6.2 Experimental details

Self-supporting thin metallic targets of natural cobalt (^{59}Co is 100% abundant) and iron (^{56}Fe is 92% abundant) with thickness ≈ 700 μg/cm^2 were used for the surrogate experi-

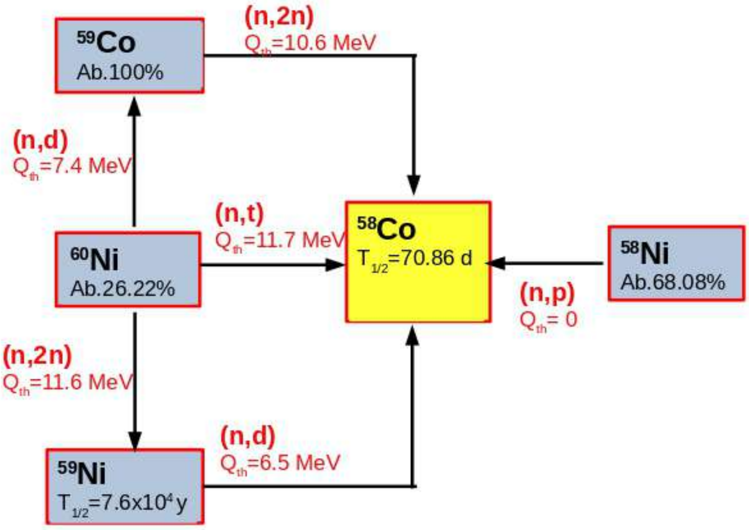

Figure 6.1: Major pathways leading to the production of ^{58}Co inside the reactor

Table 6.1: Photon induced reactions and the corresponding surrogate reactions in the present experiment, their ground-state Q values (Q_{gg}), and the compound nucleus (CN) formed

$E^{^6Li}_{beam}$ (MeV)	Surrogate reaction	Q_{gg} (MeV)	CN	Equivalent Photon induced reaction
35.9	^{56}Fe(^{6}Li,α)	4.817	^{58}Co*	^{58}Co(γ,xp)
40.5	^{59}Co(^{6}Li,α)	13.65	^{61}Ni*	^{61}Ni(γ,xp)

ment. ^{6}Li beam obtained from the BARC-TIFR Pelletron Accelerator Facility in Mumbai, was used as the projectile for both the transfer reactions, with beam energy of 35.9 MeV incident on ^{nat}Fe and 40.5 MeV on ^{59}Co respectively. The surrogate reactions for the desired and reference photon induced reactions, their ground state Q values (Q_{gg}), and the corresponding compound nucleus of interest are tabulated in Table 6.1. Schematic diagram for the experimental setup and detector details are discussed in Chapter 3.

The energy calibrated correlation plot of ΔE versus total energy (E_{tot}) obtained from telescope detector clearly identifies each projectile like fragment, such as a proton, deuteron, alpha particles, triton, etc. which is shown in Fig. 6.2a. To record the evaporated particles from the compound nucleus, two sets of strip detectors S_1 and S_2

are placed in the backward angles covering an angular range of 110^0-130^0 and 140^0-160^0 respectively. The evaporating protons from the compound nucleus ^{58}Co and ^{61}Ni in the two different transfer reactions are identified in strip detectors in coincidence with the outgoing alphas, for both ^{58}Co and ^{61}Ni, using the same telescope. Figure 6.2*b* represents a typical energy-calibrated two-dimensional plot of ΔE versus total energy (E_{tot}) obtained from one of the 32 $\Delta E - E$ strip detectors. The spectrum clearly differentiates evaporated particles such as ^{4}He and H isotopes (p,d,t) from the compound nucleus.

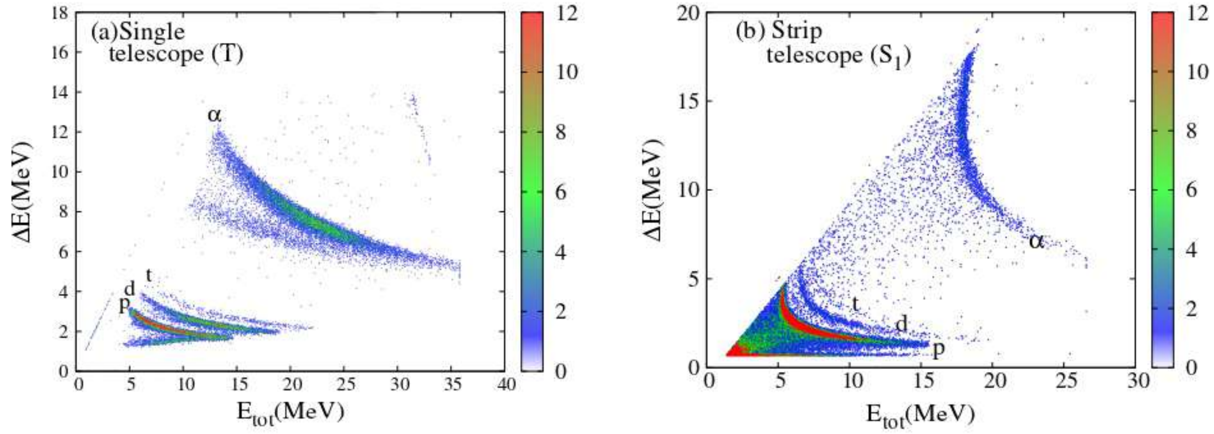

Figure 6.2: (a)ΔE versus total energy E_{tot} plot for ^{56}Fe(^{6}Li,α) reaction at $E_{lab} = 35.9$ MeV measured at T, (b)ΔE versus total energy E_{tot} plot for ^{56}Fe(^{6}Li,α) reaction at $E_{lab} = 35.9$ MeV obtained from one of the 16 E-ΔE strip detectors S_1.

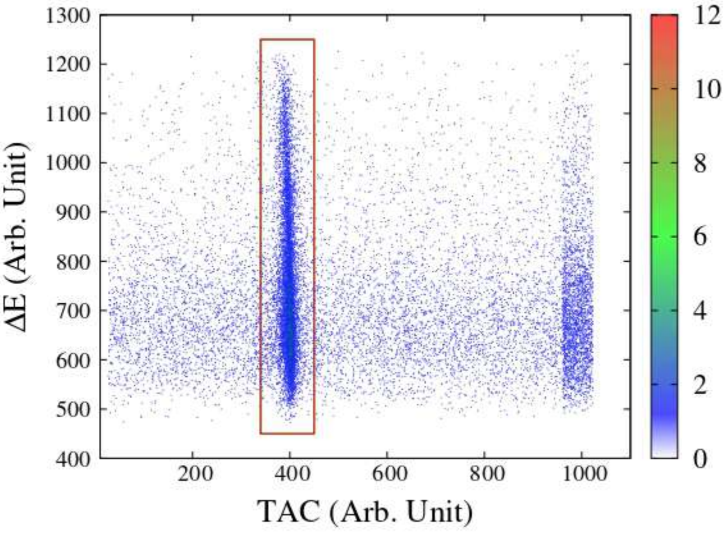

Figure 6.3: Plot of proton TAC versus alpha PLF energy in ^{56}Fe(^{6}Li,α) reaction at $E_{lab} = 35.9$ MeV

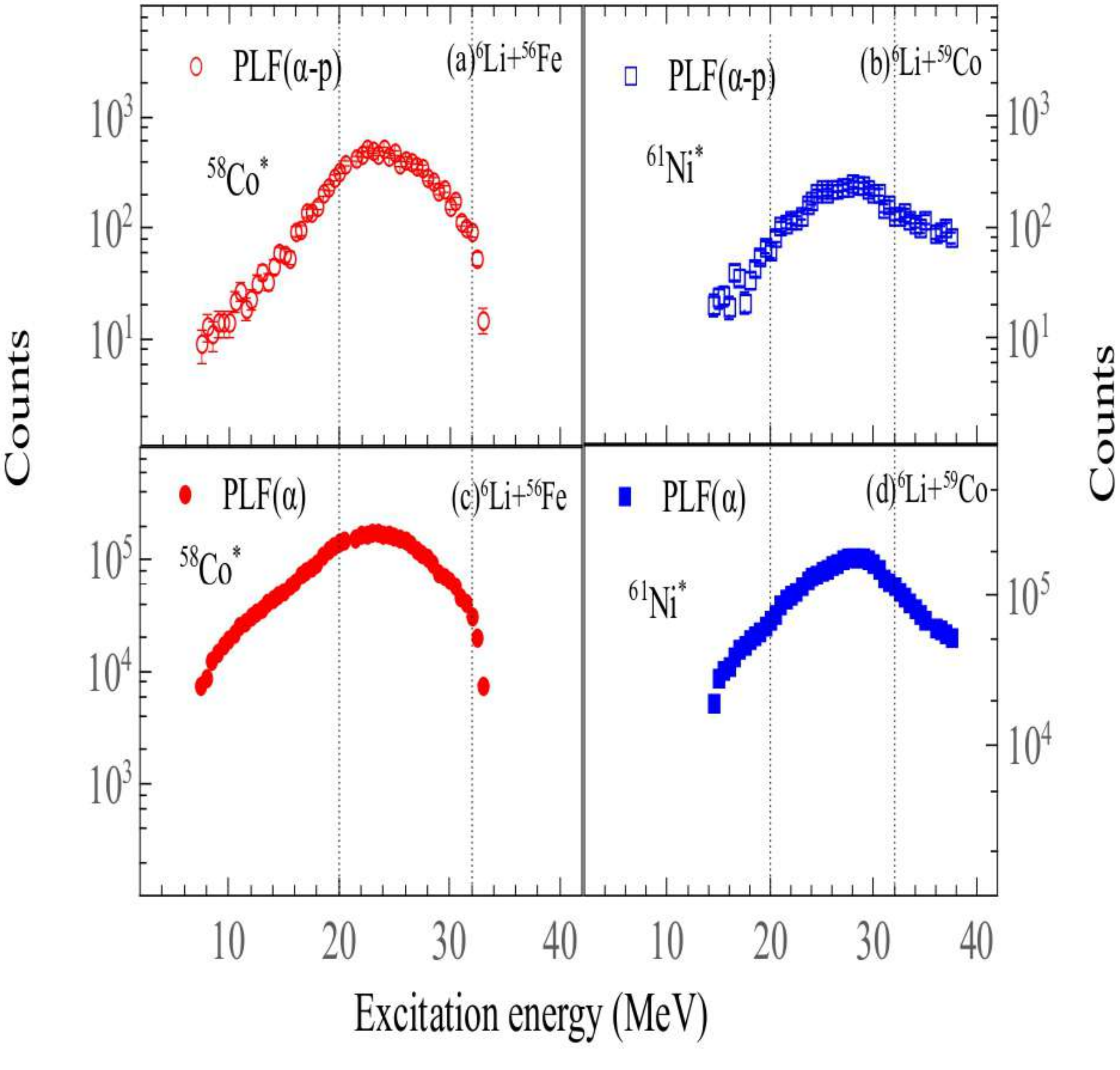

Figure 6.4: Particle spectra of the target like fragments produced in ^{6}Li+^{56}Fe and ^{6}Li+^{59}Co corresponding to the α PLF respectively with[(a) ,(b)] and without [(c) ,(d)] coincidence with evaporated protons.

The decay probability of the populated compound nucleus for the particular emission channels (here proton) at the given excitation energy E$_x$, $\Gamma_p^{CN}(E_x)$, is determined using the following relation;

$$\Gamma_p^{CN}(E_x) = \frac{1}{\epsilon}\frac{N_{i-p}(E_x)}{N_i(E_x)} \tag{6.1}$$

Where N$_i$ represents the total number of PLF events and N$_{i-p}$ is the number of coincidence events, between the protons and PLF's, ϵ denote the efficiency of detection set up.

The compound nuclear energy spectra of nuclei ^{58}Co and ^{61}Ni were determined from the event by event mode analysis, applying the two-body kinematics for α PLF channels. The particle spectra corresponding to singles events for α transfer are shown in Figs. 5(a) and 5(b). The respective particle energy spectra of the compound nuclei ^{58}Co and ^{61}Ni in coincidence with the evaporated protons are shown in Figs. 5(c) and 5(d). A bin size of 0.5 MeV was used in determining the spectra. The statistical uncertainties are also presented along with the measured data. From the excitation energy spectra, it is found that the compound nucleus ^{58}Co and ^{61}Ni are populated at an overlapping excitation energy range of 20-32 MeV in the ^{56}Fe(^{6}Li,α) reaction at E$_{lab}$ = 35.9 MeV and in the ^{59}Co(^{6}Li,α) reaction at E$_{lab}$ = 40.5 MeV, which is marked as vertical broken lines in Fig. 6.4. To verify the compound-like behavior of the isotope populated in the transfer reaction, the proton spectra obtained from the strip detector are compared with those predicted by TALYS at an excitation energy of 25 MeV, as shown in Fig.6.5. It can be observed that the measured proton spectrum and the TALYS predictions are in good agreement, thereby confirming the evaporation process from the compound nucleus ^{58}Co*. The decay probabilities for the compound nuclei ^{58}Co and ^{61}Ni, along with their associated uncertainties, are shown in Fig.6.6.

In the present study, the compound nuclei are formed in the excitation energy range of $\approx$ 20-32 MeV corresponding to the alpha energies, E$_\alpha$ = 35.5 to 13.5 MeV. The excitation energies were determined from PLFs using two body kinematics, applying an appropriate

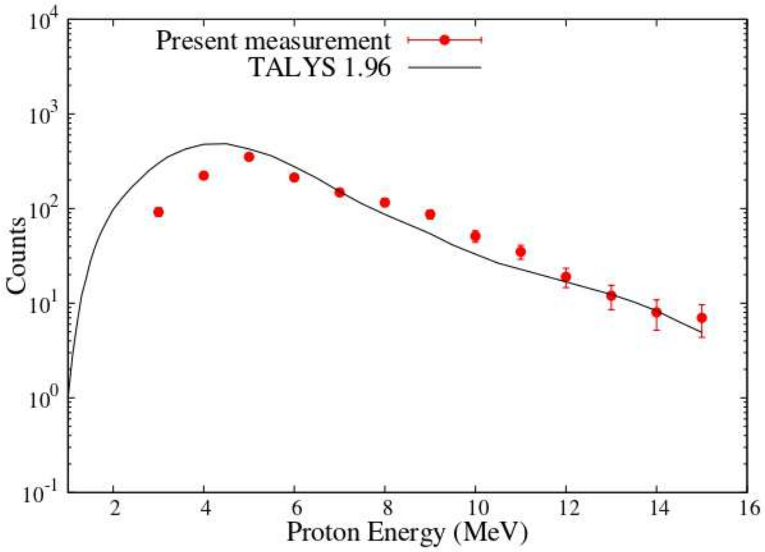

Figure 6.5: The measured proton energy spectrum obtained in a strip detector in coincidence with the α-particle PLF, corresponding to the reaction ^{56}Fe(^{6}Li,α) at $E_{lab} = 35.9$ MeV, is compared with the theoretical data from code TALYS 1.96 after normalization.

gate to the PLF band. The equivalent photon energy range obtained is 20-32 MeV using the general expression $E_a = \frac{A_a + A_A}{A_A}(E_x - S_a)$ where S_a is the projectile separation energy from the compound nucleus. Since we are dealing with the energetic gamma photon, the excitation energy will be equivalent to the incident energy after subtracting the necessary recoiling energy of the nucleus.

Using the coincidence and single counts obtained from the telescopes, the decay probabilities of compound nucleus ^{58}Co and ^{61}Ni in the alpha transfer reaction have been determined for the excitation energies of interest in respective cases, by applying Eq. (6.1) in steps of 1 MeV. Accordingly, the cross section of ^{58}Co(γ,xp) reaction is expressed in terms of surrogate ratio, as

$$\frac{\sigma^{^{58}Co(\gamma,xp)(E_\gamma)}}{\sigma^{^{61}Ni(\gamma,xp)(E_\gamma)}} = \frac{\sigma^{CN}_{\gamma+^{58}Co}(E_\gamma)\Gamma_p^{^{58}Co}(E_x)}{\sigma^{CN}_{\gamma+^{61}Ni}(E_\gamma)\Gamma_p^{^{61}Ni}(E_x)} \tag{6.2}$$

Here $\sigma^{CN}_{\gamma+^{58}Co}(E_\gamma)$ and $\sigma^{CN}_{\gamma+^{61}Ni}(E_\gamma)$ are the cross sections for the formation of the compound nucleus of the desired and the reference reactions. The photonuclear reaction ^{61}Ni(γ,xp) serves as the reference reaction, and the related data were taken from the

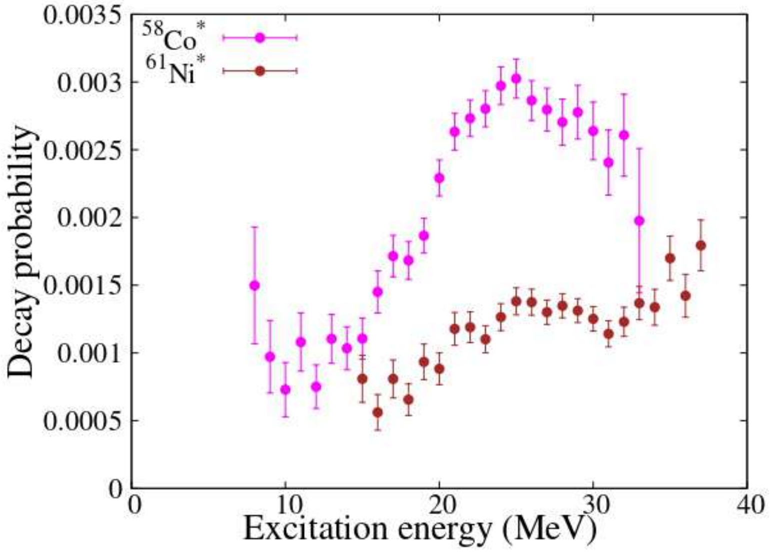

Figure 6.6: The decay probabilities corresponding to the compound nuclus ^{58}Co and ^{61}Ni populated through the transfer reactions ^{56}Fe(^{6}Li,α) at E_{lab} = 35.9 MeV and ^{59}Co(^{6}Li,α) at E_{lab} = 40.5 MeV, respectively

corresponding IAEA/KAERI photonuclear data library [8, 9], since there are no experimental data available in the experimental data library such as EXFOR. We compared the IAEA/KAERI data with the total proton production cross section obtained from the code TALYS 1.96, as shown in Fig. 6.7. The TALYS model calculations were performed using the Skyrme-Hartree-Fock-BCS model for level density and the temperature-dependent Skyrme-Hartree-Fock-Bogoliubov model for the photon strength function. The incident photon energies are equivalent to the excitation energies of the compound nucleus, hence the cross section is obtained for an equivalent photon energy range of 24-32 MeV.

6.3 Nuclear Model Calculations

The nuclear reaction code TALYS 1.96[10] has been used for the theoretical calculations. Since the proton is being the tagged particle, the following channels have been accounted for in the calculations viz. (γ,p), (γ,np), (γ,2p), (γ,pd), (γ,pα), (γ,n2p), and (γ,2np). Threshold energies for these reactions are tabulated in Table 6.2. The masses used in the calculation has taken from the 2020 Atomic Mass Evaluation by M. Wang *et al.*[11]. The theoretical calculation has been performed for energies ranging from threshold to 32

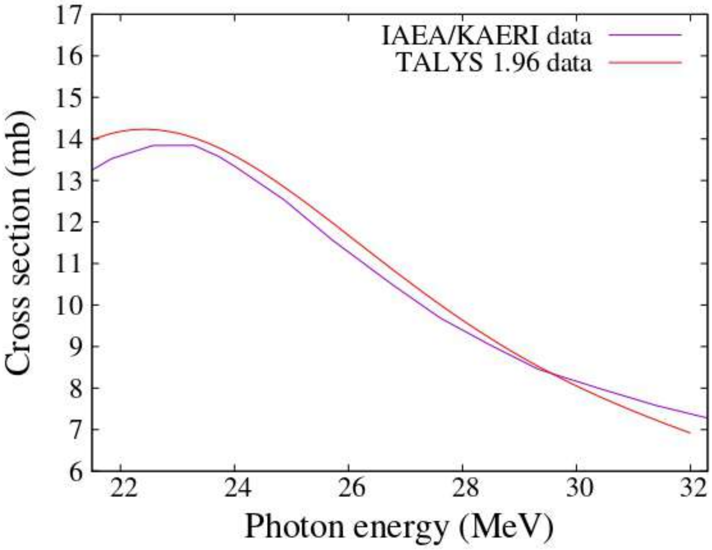

Figure 6.7: Comparing the ^{61}Ni(γ,xp) reaction data retrieved from the recommended IAEA photonuclear database, which incorporates the KAERI data in these cases, with the ^{61}Ni(γ,xp) data obtained through calculations using the TALYS 1.96 code.

Table 6.2: Threshold energies for different reaction channels included in ^{58}Co(γ,xp) and ^{61}Ni(γ,xp) reactions

Reaction Channel	Threshold Energy (MeV)	
	^{58}Co	^{61}Ni
(γ,p)	6.95	9.86
(γ,np)	14.6	17.35
(γ,2p)	17.52	18.14
(γ,pα)	14.28	17.02
(γ,pd)	22.56	22.49
(γ,2np)	25.8	27.81
(γ,n2p)	24.79	24.72

MeV. The cross section of the reference reaction ^{61}Ni(γ,xp) was taken from IAEA/KAERI photo-nuclear data library. Certain conditions, as outlined in Subsection 2.2.4 of Chapter 2, must be satisfied in order to apply the surrogate ratio method for determining the cross section. We have examined these three conditions individually, taking into account the present set of photon-induced reactions and their corresponding surrogate reactions.

6.3.1 J$^{\pi}$ -by- J$^{\pi}$ convergence

We have calculated the proton decay probabilities (P$_{xp}$) for different spin (J) states of both the compound nuclei ^{58}Co and ^{61}Ni, formed through the transfer reaction ^{56}Fe(^{6}Li,α) and

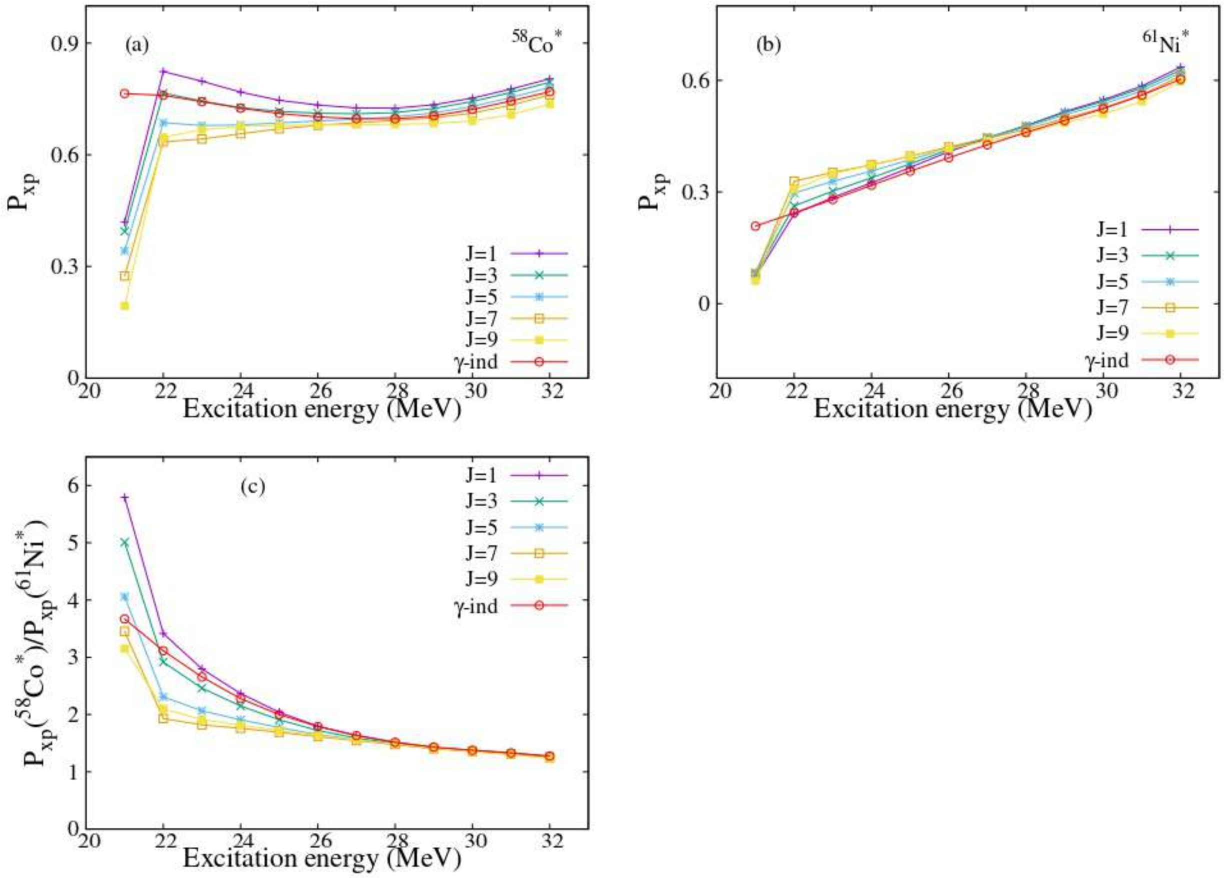

Figure 6.8: (a)The decay probabilities (P_{xp}) for various spin states (J) of ^{58}Co* populated in ^{56}Fe(^{6}Li,α) reaction at E_{lab} = 35.9 MeV and in the corresponding photon induced reaction ^{58}Co(γ,xp), as a function of excitation energy. (b)Similar to (a) but for the compound nucleus ^{61}Ni populated in ^{59}Co(^{6}Li,α) reaction at E_{lab} = 40.5 MeV and in the corresponding photon induced reaction ^{61}Ni(γ,xp). (c)The ratio of decay probabilities of ^{58}Co to ^{61}Ni for various spin (J) states compared to photon induced reaction as a function of excitation energy.

^{59}Co(^{6}Li,α), respectively. An excitation energy range of 21-32 MeV has been selected, which is the energy range of the compound nucleus found to be populated in the surrogate reactions ^{56}Fe(^{6}Li,α) and ^{59}Co(^{6}Li,α). We analyze theoretical predictions up to J= $(9)^{\pm}$ and find consistent behavior across both ($\pm$) parity states. Since the maximum spin transfer for the photonuclear reaction is ΔJ=1, we have also calculated the decay probabilities corresponding to the ^{58}Co(γ,xp) and ^{61}Ni(γ,xp) reactions. The results are shown in Fig. 6.8.

The decay probabilities of the populated compound nuclei ^{58}Co and ^{61}Ni, and the corresponding ratio for various spin states are shown in Fig. 6.8a, Fig. 6.8b, and Fig. 6.8c respectively. Specifically, the decay probabilities resulting from the ^{58}Co(γ,xp) and ^{61}Ni(γ,xp) reactions are indicated by the red line-points in each figure. It is evident from the Fig. 6.8a and Fig. 6.8b that the decay probabilities (P_{xp}) of the compound nucleus remarkably depend on the angular momentum (J) state of the decaying nucleus. However, it is obvious from Fig. 6.8c that the ratio of the two decay probabilities for each spin state merge and coincide with the decay probability of the photon-induced reaction at the excitation energy range 27-32 MeV with theoretical systematic uncertainty of 5.4 to 3.3 %. But, large deviations (around 31 % at 23 MeV) of the different spin states from the γ-induced curve is observed for the excitation energies below 27 MeV. This is a clear indication that the weak Weisskopf-Ewing condition is satisfied in the excitation energy range 27-32 MeV only.

6.3.2 Equivalance of the spin distribution

The equivalence of the spin distribution (σ_J versus J) of the two compound nuclei ^{58}Co and ^{61}Ni which are populated by the surrogate reactions ^{56}Fe(^{6}Li,α) and ^{59}Co(^{6}Li,α), at ^{6}Li beam energies 35.9 MeV and 40.5 MeV are recently investigated by R. Gandhi *et al.* [12]. They have used the 3-body classical dynamical code PLATYPUS [13] to calculate the incomplete fusion (ICF) cross sections at beam energies 35.9 and 40.5 MeV. The results for incomplete fusion or transfer reaction cross sections for the two systems, are shown in Fig. 6.9 (figure has been taken from R. Gandhi *et al.* [12]). It is evident from the figure that the spin distribution for both surrogate reactions are equivalent.

6.3.3 Spin population in the surrogate reactions

Based on the analysis of R. Gandhi *et al.* [12], the average spin populated in the transfer reactions ^{56}Fe(^{6}Li,α) and ^{59}Co(^{6}Li,α) are found to be 5.1 $\hbar$ and 5.6 $\hbar$ respectively. The spin populated by the compound nuclei ^{58}Co and ^{61}Ni are also not exceeding $10\hbar$ as evident from Fig. 6.8. Hence, all the three conditions for the validity of SRM as suggested by Chiba *et al.* are satisfied by the current set of surrogate systems.

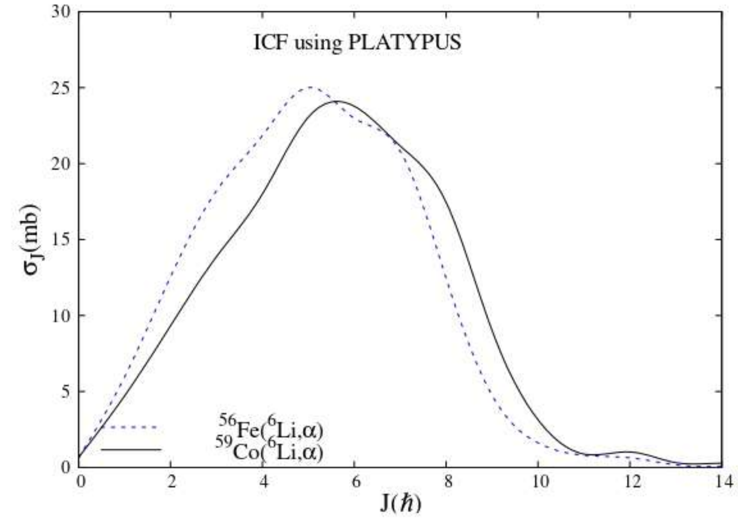

Figure 6.9: ICF cross section corresponding to the capture of deutron fragment by the target in the surrogate reactions ^{56}Fe(^{6}Li,α) and ^{59}Co(^{6}Li,α) at ^{6}Li beam energies 35.9 MeV and 40.5 MeV respectively. (Figure has been taken from *R. Gandhi et al. [12]*)

6.4 Result and discussions

The cross section of the photonuclear reaction ^{58}Co(γ,xp) was determined using the surrogate ratio method, and results were analyzed with different nuclear level density models obtained from statistical nuclear reaction code, TALYS 1.96. Various phenomenological level density models such as the Constant Temperature model+Fermi Gas model [14](CTM+FGM), which incorporates the constant temperature model for lower energy and Fermi gas model for higher energy region, the Back-shifted Fermi Gas model (BFM)[15] and the Generalised super fluid model (GSM)[16] are used in the TALYS model code. Along with these phenomenological models, the TALYS 1.96 code incorporates parity-dependent nuclear level densities based on microscopic combinatorial tables. These include calculations from the Hartree-Fock-Bogoliubov model using the Skyreme force proposed by Goriely[17], the Hartree-Fock-Bogoliubov model using the Gogny force proposed by Goriely and Hilaire[18], and the temperature-dependent Hartree-Fock-Bogoliubov calculations using the D1M Gogny force[19]. The results are presented in Fig. 6.10, highlighting measured cross sections by red filled circles. The reference reaction cross section was taken from the IAEA/KAERI photo-nuclear data library. The cross section was de-

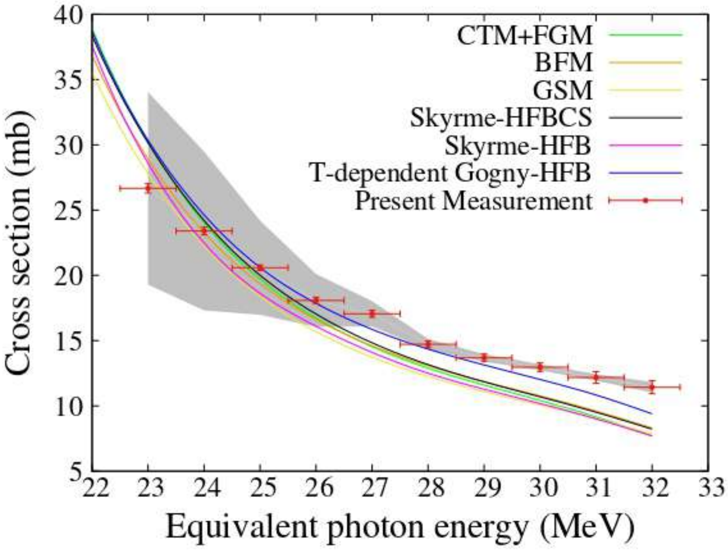

Figure 6.10: Comparison of ^{58}Co(γ,xp) reaction data with different level density models obtained from nuclear reaction code TALYS 1.96 (Default parameter values serve as inputs for the calculation). The grey shaded region represents the theoretical systematic uncertainties arising from the SRM technique.

termined, over the incident photon energy range 23-32 MeV, using the measured proton decay probabilities from the compound nuclei ^{58}Co* and ^{61}Ni*. Measured cross sections are presented in Table 6.3 along with uncertainties. The result obtained corresponds to the equivalent photon energy interval of 1 MeV. The uncertainties presented in the table are statistical uncertainties associated with the measurements. The surrogate ratio method effectively reduces most of the systematic uncertainties, such as those related to detector efficiencies, beam flux, and other experimental factors, when measuring the ratio of decay probabilities. The error bars shown for equivalent photon energies correspond to energy bins with a width of 1.0 MeV. Other contributions to the energy uncertainties, stemming from factors such as incident beam energy and target thickness, were found to be negligible in comparison.

Employing the SRM technique to obtain the cross sections itself produces additional theoretical systematic uncertainties. Major contributions to the uncertainties are originating as a result of variations in the decay probabilities corresponding to different J$^{\pi}$ values. The theoretical systematic uncertainties are evaluated by calculating the deviations of the ratio of decay probabilities of the compound nuclei for different spin (J) states from that

Table 6.3: Measured cross section data for ^{58}Co(γ,xp) reaction with statstical uncertainties arising from the measured counts along with different terms in Eq.6.2.

E_γ (MeV)	$\sigma^{CN}_{\gamma+^{58}Co}$ (mb)	$\sigma^{CN}_{\gamma+^{61}Ni}$ (mb)	$P^{^{58}Co}_{xp}(E_x)$ x10^{-3}	$P^{^{61}Ni}_{xp}(E_x)$ x10^{-3}	$\sigma^{^{61}Ni(\gamma,xp)}$ (mb)	$\sigma^{^{58}Co(\gamma,xp)}$ (mb)
23 ± 0.5	23.71	31.18	2.80±0.13	1.1±0.1	13.78	26.67 ± 0.35
24 ± 0.5	18.30	24.32	2.97±0.14	1.3±0.1	13.23	23.40 ± 0.29
25 ± 0.5	14.53	19.37	3.02±0.14	1.4±0.1	12.53	20.59 ± 0.22
26 ± 0.5	11.84	15.74	2.86±0.15	1.4±0.1	11.55	18.08 ± 0.24
27 ± 0.5	9.86	13.04	2.80±0.16	1.30±0.09	10.5	17.06 ± 0.27
28 ± 0.5	8.34	11.00	2.70±0.17	1.35±0.09	9.68	14.73 ± 0.26
29 ± 0.5	7.18	9.40	2.78±0.20	1.31±0.01	8.46	13.28 ± 0.29
30 ± 0.5	6.25	8.14	2.64±0.21	1.25±0.09	8.01	12.96 ± 0.32
31 ± 0.5	5.44	7.14	2.41±0.24	1.14±0.01	7.58	12.08 ± 0.44
32 ± 0.5	4.75	6.33	2.6±0.3	1.23±0.11	7.18	11.43 ± 0.49

of photon induced reaction. A deviation of 5.4-3.3 % is observed from the actual photon induced curve, in the excitation energy range 27-32 MeV, which is shown as the grey shaded region in Fig. 6.10. The discrepancies become more pronounced, especially as the equivalent photon energy decreases below 27 MeV. These observations suggest that the current cross section measurements obtained using the surrogate ratio method are reliable, as they remain within an acceptable range of theoretical systematic uncertainties across the energy range considered.

Due to the absence of experimental cross-section data for the ^{58}Co(γ,xp) reaction, theoretical model comparisons were carried out using the TALYS 1.96 code. Present data were analyzed using various level density models which are presented in Fig. 6.10. The solid curves in the figure represent cross sections obtained for different level density models, which show similar trends in the considered energy range. We also examined the gamma strength function models available in the TALYS 1.96 code to assess the consistency of the present measurements with theoretical predictions. The results of these analyses are presented in Fig. 6.11. Kopecky-Uhl model [20] of E_1 gamma-ray strength function that uses generalized Lorentzian form with temperature dependence and Brink-Axel Lorentzian model [21, 22], Skyrme-Hartree-Fock BCS model [23], Skyrme-Hartree-Fock Bugoliubov model [24], Goriely's hybrid model [25], Temperature-dependent Skyrme-Hartree-Fock Bogoliubov model [24], Temepratrure-dependent Relativistic Mean Field model [26], and

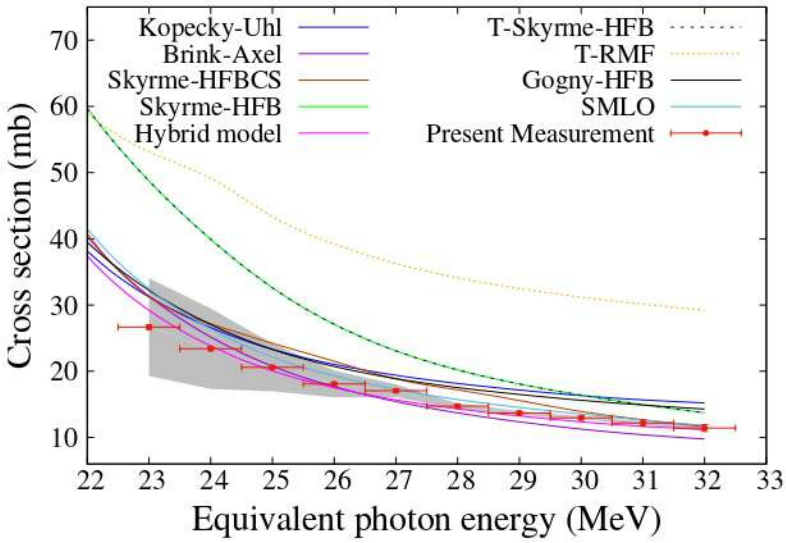

Figure 6.11: Variations of the ^{58}Co(γ,xp) reaction cross section for different photon strength function models performed using TALYS 1.96, keeping temperature-dependent Gogny force HFB level density model as constant.

Gogny-Hartree-Fock-Bogoliubov model [27] are also utilized within the code. In addition to these methods, the TALYS 1.96 code also integrates a modified technique known as the Simplified Modified Lorentzian (SMLO) model [28]. This modification was developed to address discrepancies between established phenomenological and microscopic models. We have examined the variations of photon strength function for the present reaction by fixing each level density model. Out of the six level density models, we obtained much more consistent results for the temperature-dependent Gogny-HFB level densities, and we also observed a similar trend among all the strength function models when comparing them with the present experimental data. For the visualization purpose, selected strength function models are shown in Fig. 6.12, along with the measured data. We have performed a χ^2 analysis to determine the best gamma-ray strength function model, which satisfies the present measurement in the equivalent photon energy range 23-32 MeV. The calculation identifies the Goriely's hybrid model as the most suitable model for explaining photon absorption in the present reaction.

Since the actual surrogate experiment has been performed using a natural Fe target, we have also investigated the cross section dependence of various isotopes in the target. The

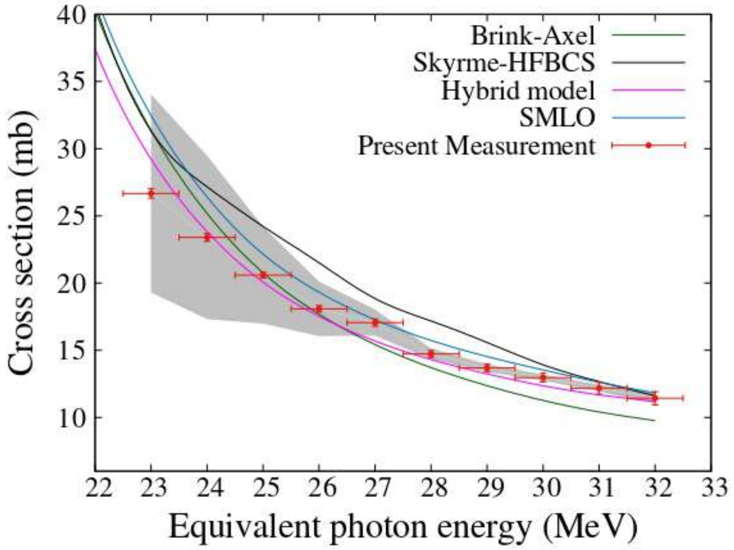

Figure 6.12: Same as Fig.6.11, but showing only selected strength function models for clarity.

most abundant isotope in natural Fe is ^{56}Fe($\approx 91.76\%$), it also consists of smaller fractions of other isotopes such as ^{54}Fe($\approx 5.85\%$), ^{57}Fe($\approx 2.12\%$), and ^{58}Fe($\approx 0.28\%$). Even these low abundances may contribute to measurables in the experiment. Corresponding contributions can be studied by accounting various reaction cross sections viz. ^{58}Co(γ,xp), ^{56}Co(γ,xp), ^{59}Co(γ,xp), and ^{60}Co(γ,xp) reactions. Hence, we have performed TALYS 1.96 calculations utilizing modified parameters (T-dependent Gogny-HFB and Goriely's hybrid model) to obtain cross section for above mentioned reactions. The total cross sections were determined by summing each cross section with weight factors corresponding to their abundance in the natural target, resulting in the cross section for a natural target. The cross section plot corresponds to natural and enriched target represented by a black dashed line and blue solid line respectively are shown in Fig. 6.13 along with measured cross sections. The results suggest that the cross sections for both natural and enriched targets are consistent with each other, as well as with the measured cross sections.

6.5 Conclusions

In summary, we have determined the cross section of ^{58}Co(γ,xp) by employing the surrogate ratio method. The cross section obtained is in steps of 1 MeV in the equivalent

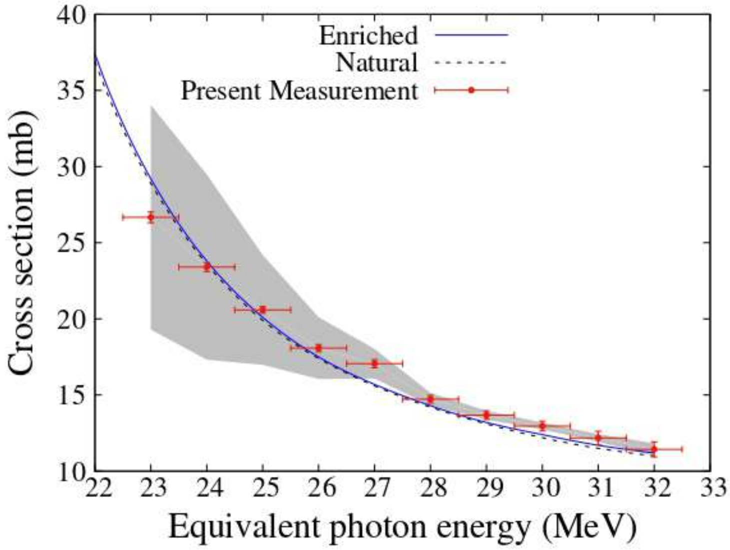

Figure 6.13: Comparison of the cross section for the reaction ^{58}Co(γ,xp) derived from natural and enriched targets using TALYS 1.96, alongside the corresponding measured data (The calculation utilizes the best level density and strength function models obtained).

photon energy range 27-32 MeV. Theoretical model calculations performed using TALYS 1.96 code are consistent with the measured results, in the photon energy range 27-32 MeV. Presently, the surrogate reaction method successfully produces the cross section of photonuclear reaction ^{58}Co(γ,xp) within a theoretical systematic uncertainty of 5.4-3.3 %. In the case of unstable medium mass nuclei, the proton decay probabilities can be studied by populating the required compound nucleus via the surrogate technique, which can be further used to determine the corresponding cross sections. Accordingly, this indirect method can be used as an effective tool to study the cross sections of photonuclear reactions involving unstable medium mass nuclei by properly accounting the spin parity mismatches.

Bibliography

[1] A. S. Penfold and J. E. Leiss. Analysis of photonuclear cross sections. *Physical Review*, 114:1332–1337, Jun 1959.

[2] B. S. Ishkhanov and V. V. Varlamov. Photonuclear reactions: Modern status of the data. *Physics of Atomic Nuclei*, 67:1664–1673, 2004.

[3] Heishun Z., Yoshitaka T., Taro K., Takehito H., T. Shizuma, Junichiro Y., Toshiteru K., H. Toyokawa, Masahiro K., and H. Ohgaki. Generation of high energy gamma-ray by laser compton scattering of 1.94-μm fiber laser in uvsor-iii electron storage ring. *Energy Procedia*, 89:335–345, 06 2016.

[4] Takehito H. and Ryoichi H. Photo-nuclear science using laser compton scattering gamma-rays in jaea. *AIP Conference Proceedings*, 1024:17–24, 06 2008.

[5] J. E. Escher, J. T. Harke, F. S. Dietrich, N. D. Scielzo, I. J. Thompson, and W. Younes. Compound-nuclear reaction cross sections from surrogate measurements. *Review of Modern Physics*, 84:353–397, Mar 2012.

[6] L. Reali, M. R. Gilbert, M. Boleininger, and S. L. Dudarev. Intense γ-photon and high-energy electron production by neutron irradiation: Effects of nuclear excitations on reactor materials. *PRX Energy*, 2:023008, Jun 2023.

[7] Luca Reali, Mark R. Gilbert, Max Boleininger, and Sergei L. Dudarev. γ-photons and high-energy electrons produced by neutron irradiation in nuclear materials. *Journal of Nuclear Materials*, 585:154584, 2023.

[8] Iaea photonuclear data library (iaea-pd 1999).

[9] J. H. Chang, Y. O. Lee, and Y. I. Han. *KAERI photonuclear library (KAERI/TR–1512/2000)*. 2000.

[10] Koning, A., Hilaire, S., and Goriely, S. Talys: modeling of nuclear reactions. *The European Physical Journal A*, 59(6):131, 2023.

[11] Meng Wang, W.J. Huang, F.G. Kondev, G. Audi, and S. Naimi. The ame 2020 atomic mass evaluation (ii). tables, graphs and references*. *Chinese Physics C*, 45(3):030003, mar 2021.

[12] Ramandeep Gandhi, B. K. Nayak, S. V. Suryanarayana, A. Pal, G. Mohanto, S. De, A. Parihari, A. Kundu, P. C. Rout, S. Santra, K. Mahata, B. Srinivasan, E. T. Mirgule, and J. Pandey. Determination of $^{53}\mathrm{Mn}(n,xp)$ cross sections using the surrogate reaction ratio method. *Physical Review C*, 100:054613, Nov 2019.

[13] A. Diaz-Torres. Platypus: A code for reaction dynamics of weakly-bound nuclei at near-barrier energies within a classical dynamical model. *Computer Physics Communications*, 182(4):1100–1104, 2011.

[14] A. Gilbert and A. G. W. Cameron. A composite nuclear-level density formula with shell corrections. *Canadian Journal of Physics*, 43:1446, January 1965.

[15] W. Dilg, W. Schantl, H. Vonach, and M. Uhl. Level density parameters for the back-shifted fermi gas model in the mass range 40 ¡ a ¡ 250. *Nuclear Physics A*, 217(2):269–298, 1973.

[16] A V Ignatyuk, K K Istekov, and G N Smirenkin. Collective effects in level density, and the probability of fission. *Soviet Journal of Nuclear Physics (Engl. Transl.); (United States)*, 30:5, 11 1979.

[17] S. Goriely, S. Hilaire, and A. J. Koning. Improved microscopic nuclear level densities within the hartree-fock-bogoliubov plus combinatorial method. *Physical Review C*, 78:064307, Dec 2008.

[18] S. Hilaire, M. Girod, S. Goriely, and A. J. Koning. Temperature-dependent combinatorial level densities with the d1m gogny force. *Physical Review C*, 86:064317, Dec 2012.

[19] S. Hilaire, M. Girod, S. Goriely, and A. J. Koning. Temperature-dependent combinatorial level densities with the d1m gogny force. *Physical Review C*, 86:064317, Dec 2012.

[20] J. Kopecky, M. Uhl, and R. E. Chrien. Radiative strength in the compound nucleus $^{157}\mathrm{Gd}$. *Physical Review C*, 47:312–322, Jan 1993.

[21] D.M. Brink. Individual particle and collective aspects of the nuclear photoeffect. *Nuclear Physics*, 4:215–220, 1957.

[22] P. Axel. Electric dipole ground-state transition width strength function and 7-mev photon interactions. *Physical Review*, 126:671–683, Apr 1962.

[23] S. Goriely and E. Khan. Large-scale qrpa calculation of e1-strength and its impact on the neutron capture cross section. *Nuclear Physics A*, 706(1):217–232, 2002.

[24] S Goriely, E Khan, and M Samyn. Microscopic hfb + qrpa predictions of dipole strength for astrophysics applications. *Nuclear Physics A*, 739(3):331–352, 2004.

[25] S. Goriely. Radiative neutron captures by neutron-rich nuclei and the r-process nucleosynthesis. *Physics Letter B*, 436:10–18, 1998.

[26] I. Daoutidis and S. Goriely. Large-scale continuum random-phase approximation predictions of dipole strength for astrophysical applications. *Physical Review C*, 86:034328, Sep 2012.

[27] S. Goriely, S. Hilaire, S. Péru, and K. Sieja. Gogny-hfb+qrpa dipole strength function and its application to radiative nucleon capture cross section. *Physical Review C*, 98:014327, Jul 2018.

[28] V. Plujko, O. Gorbachenko, and K. Solodovnyk. Description of nuclear photoexcitation by lorentzian expressions for electric dipole photon strength function. *The European Physical Journal A*, 55:014327, Nov 2019.

Chapter 7

Summary and Future Outlook

7.1 Summary

Photonuclear reactions, as introduced in Chapter 1, occur when gamma radiation interacts with a target nucleus, resulting in the emission of particles such as gamma, neutrons, protons, or alpha particles. Bremsstrahlung photons, produced by high-energy electrons, are commonly used as a source of gamma radiation in photonuclear experiments. Other photon sources, such as quasi-monoenergetic photons, bremsstrahlung-tagged photons, and laser-Compton scattered photons, are also used depending on the specific requirements of the experiment. Photonuclear reaction data, play a crucial role in various scientific and medical applications, including radiation therapy, nuclear astrophysics, and nuclear waste transmutation. In radiation therapy, high energetic photons are routinely used for the treatment of cancer. Also large number of radioisotopes, which can be produced through photon induced reactions, are currently used for diagnostic purpose in medical field. In reactor physics, the study of cross sections for unstable nuclei plays an important role in understanding nuclear reactions and their outcomes. Currently, very limited experimental photonuclear data, in relavant area is available in the experimental data library. The available experimental data generated through different experimental setups in different laboratories exhibit some discrepancies. Hence, the generation of experimental data with proper theoretical validation is necessary in photonuclear area. The present thesis report the measured and analysed cross section, foussing the validation of two medically and one reactor physics important isotopes.

In the present thesis, both direct and indirect photonuclear measurements were conducted to determine the cross section and performed the theoretical validation as a part of photonuclear data generation. We have considered three different isotopes ^{18}F, ^{58}Co and ^{99m}Tc in three different mass regions. Among these, the integral cross sections were determined for the reactions ^{99}Tc(γ,$\gamma\prime$)^{99m}Tc and ^{19}F(γ,n)^{18}F, using photon activation techniques. However, for the case of unstable ^{58}Co isotope, surrogate ratio method, which is an indirect method was adopted to study the cross section.

Technetium-99m (^{99m}Tc) is a important medical isotope used for diagnostic purposes. Currently, this isotope is extracted from its parent isotope, Molybdenum-99 (^{99}Mo), through a molybdenum-technetium generator, which is produced within a nuclear reactor. However, the production, transportation, and activity loss associated with this method present significant challenges. Additionally, a substantial quantity of ^{99}Tc remains as nuclear waste, both in the reactor and at hospitals. To address these challenges, we have explored photon-induced reactions on ^{99}Tc as a potential alternative solution. The integral cross-section of the reaction ^{99}Tc(γ, $\gamma\prime$)^{99m}Tc was determined using a bremsstrahlung photon beam with various endpoint energies. The level density and strength function models in the statistical nuclear reaction code TALYS 1.96, which are crucial for evaluating photonuclear reactions, were optimized using the data obtained in this study. The total production cross section of ^{99m}Tc was then estimated using these experimentally optimized parameter values. Even though, the cross sections are relatively low, this method proves to be highly advantageous for the local production of the ^{99m}Tc radioisotope. The study also explores the transmutation potential of photon beams, specifically focusing on the conversion of the long-lived ^{99}Tc isotope into the stable ^{98}Mo isotope via the (γ,p) reaction channel, as an alternative for the disposal of ^{99}Tc. It was found that this transmutation can be efficiently achieved if the photon beam intensity is sufficiently high and the energy is kept below the neutron separation energy, which is not feasible. Thus, the effective way to reduce nuclear waste is the re-utilization of ^{99}Tc to produce ^{99m}Tc, with double gain in singe step.

^{18}F is an ideal candidate for positron emission tomography scan. The integral cross section of the reaction ^{19}F(γ,n)^{18}F have been determined via the photon activation method utilizing bremsstrahlung photons. Using the optimized theoretical models, we have investigated the contamination channels in photon-induced reactions. Notably, the (γ,pα) reaction, which produces ^{14}C with a threshold energy of 14.23 MeV, is the only channel leading to the production of a radioisotope. Furthermore, the β^- radiation emitted from ^{14}C is of low energy and has a relatively long half-life. All other reactions result in the production of stable products. Additionally, it was found that the maximum cross section for ^{19}F(γ,n)^{18}F is obtained at a bremsstrahlung energy of 17.8 MeV, which can be readily achieved using an electron linac

The photon induced hydrogen gas production probability from the unstable isotope ^{58}Co, generated in reactor structural materials due to continuous exposure, was investigated using the surrogate ratio method. This indirect method proved effective for studying the cross sections of photonuclear reactions involving unstable medium-mass nuclei, taking into account spin-parity mismatches. The cross section of the photonuclear reaction is obtained in the energy region 27-32 MeV. The compound nucleus ^{58}Co* was populated using the transfer reaction ^{56}Fe(^{6}Li,α) at E_{lab} = 35.9 MeV. To determine the cross section using the surrogate ratio method, ^{61}Ni(γ,xp) was selected as the reference reaction and the corresponding compound nucleus ^{61}Ni* was populated using the transfer reaction ^{59}Co(^{6}Li,α) at E_{lab} = 40.5 MeV. Reference data taken from the recommended IAEA photonuclear database, which adopted the KAERI data in this case, have been used to determine the desired cross section. Compound nuclear cross section calculations have been done using the statistical nuclear reaction code TALYS 1.96. In this study, we also conducted a theoretical spin-parity analysis to assess the applicability of the surrogate ratio method in the photonuclear domain. The surrogate reaction method was successfully applied to determine the cross section of the photonuclear reaction ^{58}Co(γ,xp), with a theoretical systematic uncertainty ranging from 5.4% to 3.3%. For unstable medium-mass nuclei, this method allows the study of proton decay probabilities by populating the required compound nucleus, which can then be used to determine the corresponding cross sections.

7.2 Future Outlook

The present studies on direct photonuclear measurement provides an overall effect of the bremsstrahlung spectrum on the cross section section of the considered isotopes. The theoretical parameters of level density and strength function models, which are essential while considering a photonuclear reaction, where able to optimized for each reactions. Thus, in future it will be helpful to quantifying the production of ^{99}Tc$(\gamma, \gamma\prime)^{99m}$Tc and ^{19}F($\gamma$,n)^{18}F. The analysis technique can also extend to investigate the other medically important isotopes such as $^{44/47}$Sc, ^{99}Mo, $^{165/169}$Er, ^{186}Re,^{161}Tb, ^{177}Lu etc.

Coming to the indirect measurement part, there are large number unstable isotopes, such as ^{57}Co, ^{55}Fe, ^{59}Ni and ^{54}Mn, are found to be produced inside the reactor due to continuos neutron exposure. Thus, the surrogate ratio method can be used in these cases to study the total proton production cross sections. Utilizing this method, we can also study the total helium gas production similar to total hydrogen gas production for the same isotopes.

Chapter 8

Recommendations

Photonuclear data has large potential for specific applications including in medical, industrial and research fied. The lack of high-quality data in photonuclear reactions poses a significant challenge in the applied photonuclear field. Although photonuclear reactions have been studied across a wide range of elements and isotopes, much of the available data remains outdated and lacks proper validation. This lack of reliable, up-to-date information hinders the development of accurate theoretical models. It also hinders the advancement of technologies that depend on photonuclear processes, such as nuclear energy production, medical imaging, and radiation therapy. Present thesis makes a significant contribution to the fields of medical and reactor physics, as the isotopes studied are highly relevant to these areas. ^{99m}Tc is a crucial isotope in the medical field for diagnostic purposes. Additionally, its ground state, ^{99}Tc, is a radioactive waste product generated during reactor operations and after diagnostic procedures in therapeutic clinics. Due to its longer half-life, this isotope requires large reservoirs and safety measures for natural transmutation. Reutilization of this isotope offers a better solution to reduce the accumulation of ^{99}Tc as nuclear waste. Another important isotope is ^{18}F, which is an ideal candidate for positron emission tomography (PET) scanning. The current production method is costly, as it requires a highly enriched water target containing ^{18}O, and a cyclotron facility. Due to its shorter half-life, a significant amount of ^{18}F will be lost during transportation from cyclotrons to the therapy centers. In this study, we have investigated the feasibility of producing

^{18}F directly at hospitals, which could significantly reduce production costs. Regarding ^{58}Co, this isotope is highly relevant to fusion reactor technology. Studying hydrogen gas production from this isotope will aid in the design of reactor structural materials, helping to assess potential damage.

Based on the present thesis work, the following recommendations are made:

1. The cross section data for the medically important isotopes, ^{99m}Tc and ^{18}F, can be used for their in-house production using the electron linac facility.
2. The photon-induced proton production cross section data for the structural material ^{58}Co can be utilized in the design of reactor structural materials.

List of Publications

1. **Shaima Akbar**, M.M. Musthafa, C.V. Midhun *et al., Determination of photonuclear cross section of* $^{58}Co(\gamma,xp)$ *reaction in the energy region 27-32 MeV via the surrogate ratio method.* European Physical Journal A 61, 13 (2025). https://doi.org/10.1140/epja/s10050-025-01485-w

2. **Shaima Akbar**, M.M. Musthafa, C.V. Midhun *et al., Integral cross section measurement of the* $^{19}F(\gamma,n)^{18}F$ *reaction for 12-20 MeV bremsstrahlung photons.* Applied Radiation and Isotopes. 218 (2025)111673, https://doi.org/10.1016/j.apradiso.2025.111673.

3. **Shaima Akbar**, M.M. Musthafa, C.V. Midhun *et al., Re-utilization of long lived* ^{99}Tc *radio isotope via Photon induced nuclear reactions.* Applied Radiation and Isotopes 204 (2024)111138, https://doi.org/10.1016/j.apradiso.2023.111138

Co-authored Publications

1. Resmi K.Bharathan, C. V. Midhun, M. M. Musthafa, M. Sreena, Silpa Ajaykumar, M. P. Farhana Thesni, Swapna Balakrishnan, Vafiya Thaslim T.T, **Shaima Akbar**, K. Nived, Akhil Ramesh, P. K. Anagha, V., Arunima Dev T., S. Keerthi E., K. S. Akshay, P. V. Arun and Ghugre, S. *Measurement of the sequential* 3α *process in the photodissociation of* ^{12}C. Phys. Rev. C 111 (6) 2025

2. Hajara K., M.M. Musthafa, N. Madhavan, S. Nath, Jagadish Gehlot, Gonika, C.V. Midhun, **Shaima Akbar** , Fathima Shirin Shana , A. Parihari , Rohan Biswas,

Amninder Kaur. *Entrance channel dependence of quasi fission in reactions leading to* ^{206}Po *compound nucleus.* Nucl. Phys. A 1042 (2024) 122789

3. K. Hajara, M. M. Musthafa , C. V. Midhun, **Shaima Akbar**, P. T. M. Shan, N. Madhavan, S. Nath , J. Gehlot, Gonika, Rohan Biswas, F. S. Shana, Amninder Kaur, Prashant N. Patil. *Evaporation residue cross section measurements for the* $^{30}Si+^{176}Yb$ *reaction.* Phys. Rev. C 105, 044619 (2022)

4. C. V. Midhun, M. M. Musthafa, S. V. Suryanarayana, T. Santhosh, A. Baishya, P. N. Patil, A. Pal, P. C. Rout, S. Santra, R. Kujur, Antony Joseph, **Shaima Akbar**, Hajara. K., P. T. M. Shan, Satheesh B., Y. Sawant, B. V. John, E. T. Mirgule, K. C. Jagadeesan, and . Ganesan. *Impact of* $^{7}\mathrm{Be}$ *breakup on the* $^{7}\mathrm{Li}(p,n)$ *neutron spectrum.* Phys. Rev. C 104, 054606 (2021)

5. Midhun C. V., Musthafa M. M., **Shaima Akbar**, Swapna Lilly Cyriac, Sajeev Sachin, Antony Joseph, Jagadeesan K. C., Suryanarayana S. V. and Ganesan S. *Spectroscopy of High-Intensity Bremsstrahlung Using Compton Recoiled Electrons.* Nucl. Sci. Eng.194(3):207–212,2020

Conference Proceedings

1. Shaima Akbar, M.M Musthafa, C.V Midhun, S.V Suryanarayana. Investigation of spin-parity conditions for the photonuclear reaction using surrogate ratio method. Proceedings of the DAE Symp. on Nucl. Phys. 68 (2024)

2. Shaima Akbar, M.M. Musthafa, C.V. Midhun, Antony Joseph, Swapna Lilly Cyriac, K.C. Jagadeesan *Integral cross section of* $^{19}F(\gamma,n)^{18}F$ *reaction at 14 MeV bremsstrahlung photon.* Proceedings of the DAE Symp. on Nucl. Phys. 67 (2023)

3. Shaima Akbar, M.M Musthafa, C.V Midhun, S.V Suryanarayana, Jyoti Pandey. *Determination of* $^{58}Co(\gamma,xp)$*cross section via the surrogate ratio method.* 8th International Conference on Women in Physics, 10-14 July 2023.

4. Shaima Akbar, M.M. Musthafa, C.V. Midhun, Antony Joseph, Swapna Lilly Cyriac, K.C. Jagadeesan. *Re-utilization and Transmutation of long lived* ^{99}Tc *radio isotope via Photon induced nuclear reactions.* 23rd National Symposium on Radiation Physics (NSRP-23), January 19 – 21, 2023

5. Shaima Akbar, M.M. Musthafa, C.V. Midhun, Resmi K. Bharathan, Sreena M., K.C. Jagadeesan. *Measurement and analysis of* $^{19}F(\gamma,n)^{18}F$ *reaction.* Proceedings of the DAE Symp. on Nucl. Phys. 66 (2022)

6. Shaima Akbar, M.M. Musthafa, C.V. Midhun, Antony Joseph, Swapna Lilly Cyriac, K.C. Jagadeesan. *The Photo-Activation based production of* $^{99}Tc^{m}$. DST-PURSE supported Satellite Symposia on Physical Sciences, Life Sciences, Chemical Sciences, and Mathematical-Statistical-Computational Sciences held at Bharathiar University on September 13-15 2022

7. Shaima Akbar, Jyoti Pandey, M.M. Musthafa, Midhun C.V., Bhawna Pandey, S.V. Suryanarayana, B.K. Nayak, H.M Agrawal, S. Santra, Antony Joseph, and K.C Jagadeesan. *Determination of excitation function of* $^{61}Ni(\gamma,xp)$ *reaction using surrogate ratio method.* Proceedings of the DAE Symp. on Nucl. Phys. 64 (2019)

8. Akhil Ramesh, M.M. Musthafa, Midhun C.V., Shaima Akbar, S.S. Ghugre. *Validating Spin-Parity conditions for neutron capture cross sections using surrogate Techniques.* Proceedings of the DAE Symp. on Nucl. Phys. 68 (2024)

9. Nived K, Midhun C.V, M.M. Musthafa, Resmi K. Bharathan, Vafiya Thaslim T.T , Swapna Balakrishnan, Akhil Ramesh, Arunima Dev T.V, Anagha P.K, Shaima Akbar, Drisya Karinkuzhi and Irfana Thasni A.K. *Direct Measurement of* $^{7}Li(\gamma,\alpha)t$ *cross sections.* Proceedings of the DAE Symp. on Nucl. Phys. 68 (2024)

10. Resmi K Bharathan, Midhun CV, Musthafa MM, Sreena M, Silpa Ajaykumar, Farhana Thesni MP, Swapna B, Vafiya TT , Shaima A, Nived K, Akhil R, Keerthi ES, Akshay KS, Arun PV. *Direct Measurement of* $^{12}C(\gamma,\alpha)\ ^{8}Be\rightarrow 3\alpha$ *Cross Sections.* Proceedings of the DAE Symp. on Nucl. Phys. 67 (2023)

11. Sreena M, Midhun CV, Musthafa M.M, Resmi K Bharathan, Farhana Thesni M P, Swapna B, Vafiya T T, Shaima A, Nived K, Akhil R, Keerthi E S, Silpa Ajaykumar, Akshay K S, Arun P V. *Inclusive* α *Spectrum from* $^{12}C(\gamma,\alpha)$ *Reaction.* Proceedings of the DAE Symp. on Nucl. Phys. 67 (2023)

12. C. V. Midhun, M. M. Musthafa, S. V. Suryanarayana, H. Gokul Das, A. Shaima, K. Hajara, Joseph Antony, T. Santhosh, A. Baishya, A. Pal, P. C. Rout, S. Santra, P. T. M. Shan, B. V. John, K. C. Jagadeesan, S. Ganesan. *On the estimation of* $^{6}Li(n,\gamma)$ *cross sections*, Proceedings of the DAE Symp. on Nucl. Phys. 66 (2022)

13. C.V Midhun, M.M Musthafa, Shaima Akbar, S.V Suryanarayana, K.C Jagadeesan, N.T Rijin, *Monitor Controlled Single Projection Approach for Cross Section Unfolding*, Proceedings of the DAE Symp. on Nucl. Phys. 66 (2019).

14. Siji M, Syama G Nair, Midhun C V, Shaima Akbar, Musthafa M M, Ganesan S, *Re-Estimation of Cross section data for the IAEA EXFOR ID:40803 for* $^{232}Th\,(n,\gamma)^{233}Th$ *using covariance analysis technique.* Proceedings of the DAE Symp. on Nucl. Phys. 65 (2018).

15. Syama G Nair, Siji M, Midhun C V, Shaima Akbar, M. M Musthafa, S Ganesan. *Re-Estimation of Cros section data for the IAEA EXFOR ID:40803 for* $^{238}U(n,\gamma)^{239}U$ *using covariance analysis technique*, Proceedings of the DAE Symp. on Nucl. Phys. 65 (2018).